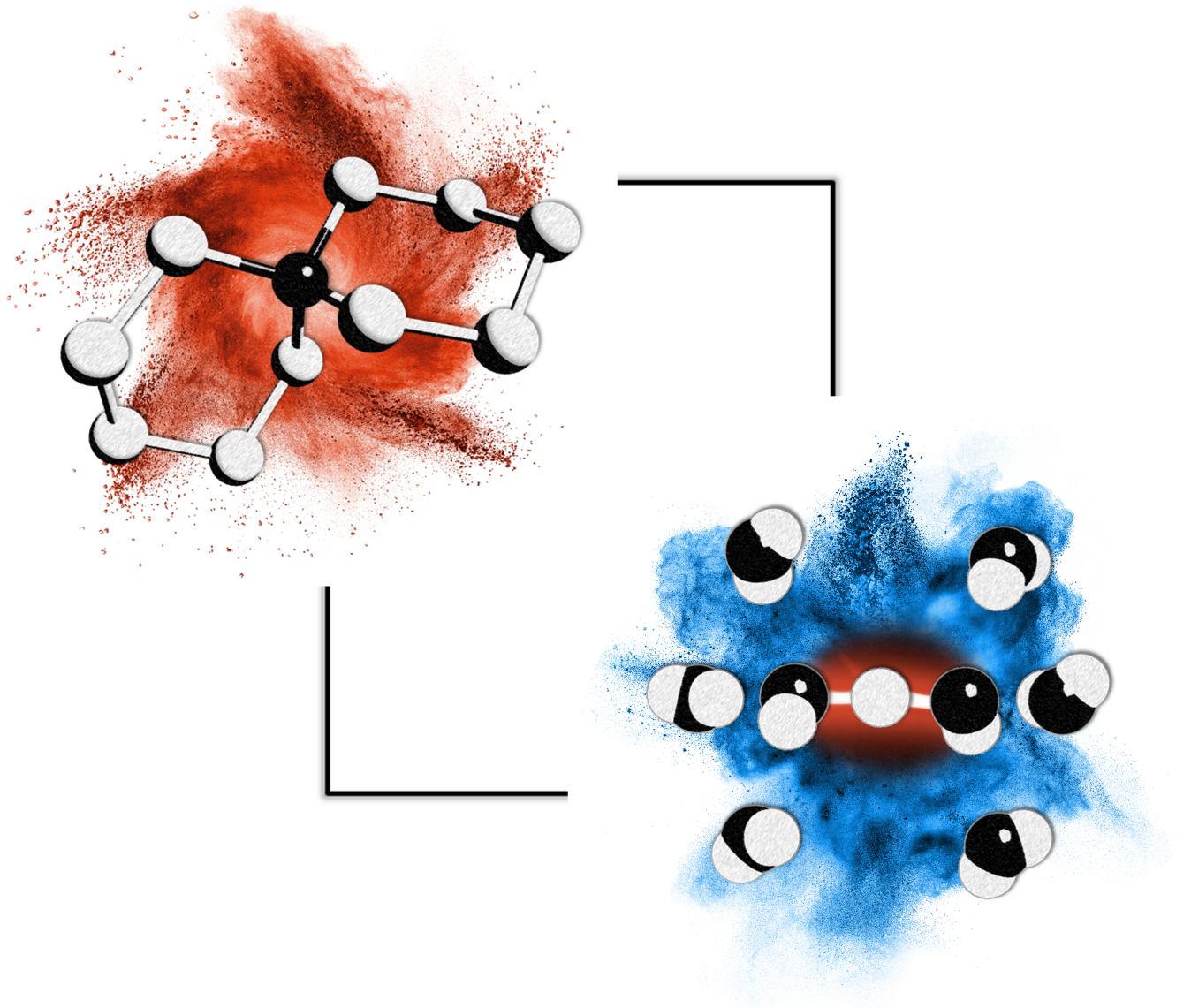# Anion exchange membranes for fuel cells and flow batteries:

Transport and stability of model systems

Dissertation an der Universität Stuttgart

von

Michael Giuseppe Marino

Anion exchange membranes for fuel cells and flow batteries: Transport and stability of model systems

Von der Fakultät Chemie der Universität Stuttgart
zur Erlangung der Würde eines

Doktors der Naturwissenschaften

(Dr. rer. nat.) genehmigte Abhandlung

Vorgelegt von

Michael Giuseppe Marino

aus Backnang

Hauptberichter:	Prof. Dr. Joachim Maier
Mitberichter:	Prof. Dr. Sabine Ludwigs
Prüfungsvorsitzender:	Prof. Dr. Frank Gießelmann
Tag der Einreichung:	03.03.2015
Tag der mündlichen Prüfung:	27.04.2015

Max-Planck-Institut für Festkörperforschung
2015

"Science is the candle in the dark."

Carl Sagan

Erklärung

Die vorliegende Doktorarbeit wurde vom Autor selbst in der Abteilung von Prof. Maier am Max-Planck-Institut für Festkörperforschung, im Zeitraum vom Juni 2011 bis März 2015 angefertigt. Der Inhalt ist die eigene Arbeit des Autors, Ausnahmen sind gekennzeichnet, und wurde noch nicht zur Erlangung einer Qualifizierung oder eines Titels an einer akademischen Institution eingereicht.

Stuttgart, 2. März 2015   Michael G. Marino

Declaration

The work described in this thesis was carried out by the author in the department of Prof. Maier at the Max Planck Institute for Solid State Research from June 2011 to March 2015. The contents are the original work of the author except where indicated otherwise and have not been previously submitted for any other degree or qualification at any academic institution.

Stuttgart, 2. March 2015   Michael G. Marino

Contents

Abstract

Polymeric anion exchange materials in membrane form can be key components in emerging energy storage and conversions systems such as the alkaline fuel cell and the RedOx flow battery. For these applications the membrane properties need to include good ionic conductivity and sufficient chemical stability, two aspects, that are not sufficiently understood in terms of materials science. Materials fulfilling both criteria are currently not available.

The transport of ions and water in a model anion exchange membrane (AEM) as well as the alkaline stability of their quaternary ammonium functional groups is therefore investigated in this thesis from a basic point of view but with the aim to bring these technologies one step closer to large scale application, as they have several advantages compared to existing energy storage and conversion systems. The hydroxide exchanging alkaline fuel cell (AFC), for example, is in principle more cost-effective than the more common acidic proton exchange fuel cell (PEMFC). This is because the high-pH environment in the AFC allows the use of non-platinum group metal catalysts such as e.g. silver and nickel. Unfortunately AFCs suffer from base induced decomposition of the membrane. Especially the quaternary ammonium (QA) functional groups are easily attacked by the nucleophilic hydroxide.

QAs with higher alkaline stability are required but there is considerable disagreement regarding which QAs are suitable, with widely varying and partially contradicting results reported in the literature. This is potentially due to neglected uncontrolled influences of the polymer backbone (e.g. water uptake, inductive and steric effects). In this thesis, these influences were avoided by investigating the decay of QA salts under controlled accelerated aging conditions (up to 10 M NaOH and 160 °C) by precipitation with Reinecke's salt and UV/Vis absorption measurements. This allowed a stability comparison based solely on the molecular structure of the QAs.

A number of different approaches to stabilize the QAs which potentially inhibit degradation reactions such as β-elimination, substitution and rearrangements were compared. These include β-proton removal, charge delocalization, spacer-chains, electron-inducing groups and conformational confinement. Heterocylic 6-membered QAs based on the piperidine structure proved to be by far the most stable cations at the chosen conditions. This was not readily apparent from their structure since they contain β-protons in anti-periplanar positions, which generally cause rapid decomposition in other types of QAs. The geometry of the cyclic structure probably exerts strain on the reaction transition states, kinetically inhibiting the degradation reactions. Other stabilization approaches resulted in markedly less stable compounds. Noticeably the benzylic group, which is the current standard covalent tether between QA and polymer, degrades very fast compared to almost all aliphatic QAs. The results of this stability study suggest that hydroxide exchange membranes for alkaline fuel cells, which are significantly more stable than current materials are achievable.

Besides stability, the transport of anions and water in AEMs was investigated in this thesis by conductivity measurements, pulsed-field gradient NMR and by recording water uptake and SAXS-patterns.

Hydroxide exchange membranes (HEM) have been reported to exhibit surprisingly low ionic conductivities compared to their proton exchange membrane (PEM) counterparts. This is partially because hydroxide charge carriers are rapidly converted to carbonates when a HEM comes into contact with ambient air. Careful exclusion of CO_2 was required to investigate pure hydroxide form membranes. For this purpose a custom glove box was designed and built that allowed preparation and measurements of HEM samples in a humidified CO_2-free atmosphere. It was found that the conductivity reduction of a carbonate contaminated HEM is not only due to the reduced ionic mobility of carbonate charge carriers compared to hydroxide, but also because of reduced water absorption of the corresponding membrane which decreases conductivity even further. Pure HEMs can in fact achieve conductivities within a factor of two of PEMs at equal ion exchange capacity at sufficient hydration, according to the differences in the ionic mobility of hydroxide and hydronium. At lower water contents though, the hydroxide mobility decreases faster than that of hydronium in comparable PEMs due to reduced dissociation and percolation as well as a break-down of structural diffusion.

Apart from the HEM, membranes in other ionic forms were investigated, with a focus on the halide forms fluoride, chloride, bromide, and iodide. Generally, all investigated AEM

properties were found to change if the type of anion was exchanged. This comprises the degree of dissociation, conductivity, membrane morphology and sometimes even water diffusion. Remarkably, at low water contents, the ionic conductivity of the HEM sank below that of the halides, despite the much higher hydroxide mobility in aqueous solution. A gradual break-down of the hydroxide structural diffusion is probably responsible. Another noticeable observation was that the degree of dissociation for at least the bromide and chloride form membranes remains almost constant over a considerable water content range, suggesting the formation of associates consisting of several ions, which probably also exists in other ionic forms.

In summary, some light was shed on the understanding of the ion and water transport processes in AEMs and QA functional groups with exceptional alkaline stability were discovered. These aspects may well serve as an initial guide for both the synthesis and the working conditions for membranes in alkaline fuel cells and RedOx flow batteries.

Zusammenfassung

Polymerbasierte Anionentauschermembranen (AEM) sind ein zentraler Bestandteil vielversprechender Energiespeicher- und Umwandlungssysteme, wie der alkalischen Brennstoffzelle (AFC) und der RedOx Flow Batterie (RFB). Die Membranen müssen hierfür gute Ionenleitfähigkeit und chemische Stabilität aufweisen, zwei wenig erforschte Aspekte mit großem Optimierungspotential.

In dieser Arbeit wurden daher der Wasser- und Ionentransport in einer Modell-AEM, sowie die alkalische Stabilität einer Vielzahl kationischer funktioneller quartären Ammoniumgruppen (QA) für AEMs untersucht. Das Ziel war es, die fundamentalen Transportprozesse in diesen Membranen aufzuklären und einen Leitfaden für die Synthese alkalisch stabiler AEMs zu erstellen. Die großflächige Anwendung von AFCs und RFBs sollen dadurch der Realität einen Schritt näher gebracht werden, da diese Technologien einige Vorteile gegenüber bisher etablierten Energiespeichern und –umwandlern haben. Zum Beispiel ist die hydroxidtauschende AFC prinzipiell günstiger in der Herstellung im Vergleich zur bekannteren sauren Protonentauscher-Brennstoffzelle (PEMFC), da die im sauren benötigten Platinmetallkatalysatoren im alkalischen durch günstigere Metalle wie Silber und Nickel ersetzt werden können. Leider werden die verfügbaren AFC-Membranen im alkalischen relativ schnell zerstört. Vor allem ihre funktionellen QAs sind von dem nukleophilen Angriff der Hydroxydionen betroffen.

QAs mit höherer alkalischer Stabilität werden daher benötigt, doch welche Gruppen hierfür in Frage kommen ist unklar, da in der Literatur von stark schwankenden und teilweise widersprüchlichen Ergebnissen berichtet wird. Dies ist vermutlich auf den unkontrollierten Einfluss des Polymers (z.B. durch Änderungen der Wasserkonzentration, induktive und sterische Effekte) zurückzuführen. In der vorliegenden Arbeit wurde dieser Einfluss unterbunden, indem die QAs als separate Salze unter kontrollierten Bedingungen (bis zu

160 °C und 10 м NaOH) untersucht wurden. Ein auf der molekularen Struktur der QAs basierender Vergleich ihrer alkalischen Stabilität wurde damit ermöglicht. Der Abbau der QAs wurde durch Fällung mit Reinecke-Salz und anschließender UV/Vis-Spektroskopie verfolgt.

Verschiedene Herangehensweisen zur Stabilisierung der QAs wurden überprüft, wie z.B. Entfernung von β-Protonen, aromatische Ladungsdelokalisierung, Alkan-Zwischenstücke (spacer-chains), Einschränkung der C-C Bindungsrotation sowie Einführung von elektroneninduzierender Gruppen. Heterocyclische Piperidin-basierte QAs waren die mit Abstand stabilsten Verbindungen bei den gewählten Bedingungen. Dies ist bemerkenswert, da β-Protonen in anti-periplanarer Position zum Stickstoffatom Teil der Piperidinstruktur sind, welche in anderen QAs zu schnellen Abbaureaktionen führen. Wahrscheinlich muss sich der Heterocyclus in den Reaktionsübergangszuständen stark deformieren, was die entsprechenden Aktivierungsenergien erhöht und die Abbaureaktionen kinetisch hemmt. Ein weiteres auffälliges Ergebnis war, dass benzylische Gruppen ein Schwachpunkt in der Struktur von QAs sind. Da QAs aus Gründen der Einfachheit bisher fast ausschließlich über solche Gruppen kovalent an das Polymer gebunden wurden, deuten die Ergebnisse der Stabilitätsexperimente stark darauf hin, dass es möglich ist die alkalische Stabilität heutiger AEMs für AFCs deutlich zu erhöhen.

Neben der alkalischen Stabilität von QAs wurde der Transport von Ionen und Wasser in einer Modell-AEM untersucht. Dazu wurden Leitfähigkeitsmessungen, Gradientenfeld NMR, Wasseraufnahmeexperimente und SAXS-Messungen durchgeführt. Im Vergleich zu Protonentauschermembranen (PEM) zeigten Hydroxidtauschermembranen (HEM) bisher eine unerwartet niedrige Ionenleitfähigkeit. Ein Grund hierfür ist die schnelle Umwandlung von Hydroxidionen in deutlich schlechter leitende Carbonate, wenn die HEM mit CO_2 (z.B. aus der Luft) in Kontakt kommt. Um Carbonat-Kontamination zu verhindern wurde daher eine Handschuhbox entworfen und konstruiert, welche Probenvorbereitung und Messungen in CO_2-freier, befeuchteter Atmosphäre ermöglichte. So wurde erkannt, dass ein weiterer bedeutender Faktor bei der Verringerung der ionischen Leitfähigkeit einer Carbonat-kontaminierten HEM die verringerte Wasseraufnahme der Membran ist. Es konnte außerdem festgestellt werden, dass eine HEM bei ausreichendem Wassergehalt Hydroxid-Leitfähigkeiten erreichen kann, die nur um einen Faktor zwei niedriger sind, als die Protonen-Leitfähigkeit einer vergleichbaren PEM (bei gleicher Ionenaustauschkapazität). Der Faktor zwei ist bedingt durch die entsprechend niedrigere Beweglichkeit

von Hydroxid im Vergleich zu Hydronium in wässriger Lösung. Mit fallendem Wassergehalt sinkt die Ionenleitfähigkeit von HEMs allerdings deutlich stärker als in PEMs aufgrund früher zurückgehender Dissoziation und Perkolation, sowie einem Zusammenbruch der Strukturdiffusion.

Zusätzlich zur HEM wurden auch Membranen in anderen Ionenformen untersucht, mit Schwerpunkt auf den Halogenidformen Fluorid, Chlorid, Bromid und Iodid. Mit Austausch des Anions verändern sich alle Membraneigenschaften (was Dissoziationsgrad, Ionenleitfähigkeit, Membranmorphologie und zum Teil selbst Wasserdiffusion einschließt). Überraschenderweise sank bei niedrigen Wassergehalten die Ionenleitfähigkeit der HEM, trotz der deutlich höheren Beweglichkeit von Hydroxid, unter die der Halogenide, was wahrscheinlich auf den graduellen Zusammenbruch der Hydroxid-Strukturdiffusion zurückzuführen ist. Eine interessante Beobachtung war ebenfalls, dass der Dissoziationsgrad der Bromid- und Chloridform Membranen über einen großen Wasservolumenbereich fast unverändert bleibt, was auf die Bildung von Ionenclustern aus mehreren Ionen hindeutet, die vermutlich auch bei anderen Ionenformen vorhanden sind.

Zusammengefasst wurde Licht auf die Transportprozesse von Anionen und Wasser in AEMs geworfen und zusätzlich funktionelle QA Gruppen mit bemerkenswerter alkalischer Stabilität entdeckt. Die vorgestellten Ergebnisse zu diesen bisher ungenügend beleuchteten Aspekten haben das Potential als vorläufiger Leitfaden bei der Synthese und den Betriebsbedingungen von Membranen für alkalische Brennstoffzellen und RedOx Flow Batterien zu dienen.

List of papers

This thesis is partially based on the following publications by the author:

M.G. Marino, J.P. Melchior, A. Wohlfarth, K.D. Kreuer, Hydroxide, halide and water transport in a model anion exchange membrane, *Journal of Membrane Science* **2014**, *464*, 61-71.

M.G. Marino, K.D. Kreuer, Alkaline stability of quaternary ammonium cations for alkaline fuel cell membranes and ionic liquids, *ChemSusChem* **2015**, *8*, 513-523.

Chapter 1

Introduction

1.1 General aspects

The demand for clean renewable energy (RE) has increased upon realizing that fossil fuels are a major cause of human induced climate change and pollution. Unfortunately, power supply from most RE sources can not produce energy on demand as they fluctuate considerably due to variances in weather conditions. The development of energy storage systems for times of increased power consumption and reduced energy production (e.g. no sun or wind) is therefore essential to make RE technologies viable on a larger scale. An adequate understanding of the properties of their components will accelerate progress towards efficient, affordable and reliable materials for RE storage.

Polymeric anion exchange membranes (AEMs) can be an integral component of energy storage and conversion technologies such as the alkaline fuel cell (AFC) and the redox flow battery (RFB). These exhibit a number of advantages over current conventional systems but many of their fundamental properties have yet to be investigated in detail and certain issues need to be resolved to pave the way for potential large scale applications. The transport of ions and water inside the membranes is for example crucial both for AFC and RFB but highly complex and dependent on factors such as hydration, ionic dissociation, and the polymer/water phase-separation. These affect e.g. conductance, ionic selectivity and Coulomb efficiency which are critical for application of such electrochemical devices. Besides satisfying scientific curiosity, investigating the transport processes in AEM mate-

rials may allow inferences with respect to temperature and water management in an active cell. Apart from good transport properties the membranes need to resist the aggressive chemical environments in which they are intended to be used. This especially concerns hydroxide form AEMs (i.e. hydroxide exchange membranes) in AFCs which are vulnerable hydroxide induced degradation that leads to membrane failure even at comparatively mild conditions. A comprehensive investigation of the factors that influence their alkaline stability is required, beginning with the molecular structure of the AEM cationic functional groups, as these are currently the most susceptible part in an alkaline environment.

This thesis tries to shed some light on these two open questions by addressing ion and water transport in a model AEM and the alkaline stability of a large number of quaternary ammonium functional groups.

1.2 The alkaline fuel cell

A fuel cell (FC) converts chemical energy into electrical energy by the reaction of RedOx active species at spatially separated electrodes. This requires ions to travel through an electronically insulating electrolyte between the electrodes, while electrons move along an external connection and conduct electrical work.

The most common low temperature fuel cell is the proton exchange membrane polymer electrolyte fuel cell (PEMFC) in which oxygen and hydrogen react to form water on the cathode side, while protons travel from anode to cathode through a polymer membrane. Platinum catalysts are required in the PEMFCs highly acidic conditions with state-of-the-art ion conducting membranes for electrode separation being perfluorinated sulfonic acid polymers (e.g. Nafion®, Gore® or Aquivion®). Some drawbacks to this system are the rate limiting oxygen reduction reaction (ORR), and high costs due to difficult waste treatment caused by the high fluoride content of the membranes and the required platinum. As such, a model fuel cell car by Toyota for 2015 was announced to require around 30 g of platinum, amounting to a total of € 930 for the noble metal alone at the current price of € 31 per gram.

These issues are alleviated with the alkaline fuel cell (AFC) in which the charge carrying ionic species is hydroxide (Figure 1.1). The ORR is facilitated with many catalyst

materials, due to a different reaction mechanism with a lower overpotential (PEMFC: $O_2 + 2H^+ + 2e^- \longrightarrow 2H_2O$, HEM-FC: $O_2 + 2H_2O + 4e^- \longrightarrow 4OH^-$)[1–5] and additionally, the corroding effect of O_2 is greatly reduced. This enables usage of cheap non platinum group metal catalysts (e.g. gold, silver for cathode and cobalt, nickel, iron for anode) that would have little to no activity and corrode quickly in a PEMFC.[5–11] For polymeric AFCs hydrocarbon membranes are mostly used, since fluorinated polymers degrade in alkaline medium if protons in α-position relative to a C-F bond are present[12–14] and the electron-withdrawing effect of the fluoride groups is prone to increase the degradation rate of the quaternary ammonium groups in the presence of hydroxide. Despite these difficulties, some groups are trying to realize AEMs for AFCs based on flourinated polymers.[15–17]
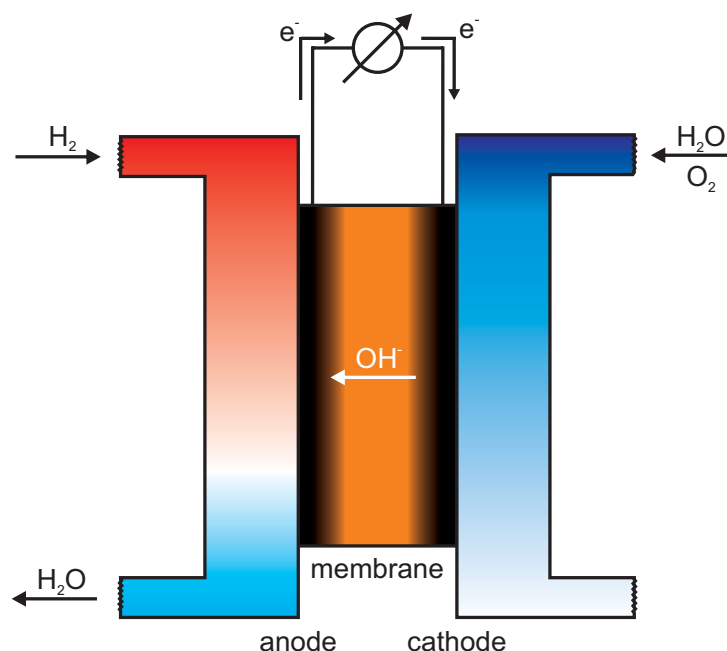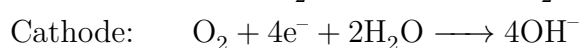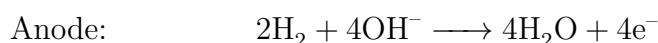

Figure 1.1: Scheme of an alkaline fuel cell.

Electrode reactions in an alkaline fuel cell:

Anode: $\qquad\qquad 2H_2 + 4OH^- \longrightarrow 4H_2O + 4e^-$

Cathode: $\qquad O_2 + 4e^- + 2H_2O \longrightarrow 4OH^-$

Overall: $\qquad\qquad 2H_2 + O_2 \longrightarrow 2H_2O$
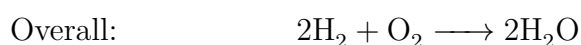
The first viable fuel cell with a power of 5 kW was built by Francis T. Bacon in 1939 using an alkaline KOH electrolyte. Over time, a number of prototype vehicles such as farm tractors, golf carts, boats, and forklifts were developed based on AFCs.[18,19] Although they

worked reasonably well, reliability, running cost, engineering problems and the later success of PEMFCs inhibited further development, except for the space programs, for many years. One of the main problems was the use of liquid KOH electrolytes (usually held inside an asbestos matrix), which require pure gas feeds containing less than 50 ppm CO_2, as otherwise carbonate precipitates decrease electrolyte conductivity and block the electrode pores, resulting in eventual system failure.

While this can be counteracted with pure CO_2-free gas feeds or through an exchangeable cycled electrolyte, requiring a CO_2 scrubber with additional pipework and pump to cycle the KOH solution, its highly corrosive properties created containment issues. Both pure gas feeds and cycled electrolytes counteract the low cost of AFCs and add considerable complexity.[9,19]

In high-end isolated environments where cost is not an issue, such as the NASA Apollo and Space Shuttle projects, liquid electrolyte AFCs were the power source of choice as they offered the highest electrical efficiency of all fuel cell systems and pure oxygen is required anyway to avoid crew suffocation. In such applications, static and cycled KOH AFCs were in use since the 1960s, though recently they were discontinued in favor of other systems with which faster progress was made, such as PEMs.[9,19,20]

Only in the wake of the search for more cost effective polymer based PEMFCs have AFCs received renewed attention (Figure 1.2). By replacing the KOH electrolyte with a polymeric hydroxide exchange membrane (HEM) it is in principle possible to combine the advantages of the AFC with those of the PEMFC. Non platinum group metal catalysts are just as viable as in a liquid electrolyte and replacing the corrosive KOH solution with a polycation eliminates potential KOH leakage and avoids carbonate precipitation, since the counter ions are fixed to the polymeric backbone. Carbonate ions are simply transported across the membrane and purged at the anode in the following reaction:

$$H_2 + CO_3^{2-} \longrightarrow H_2O + CO_2 + 2e^-$$
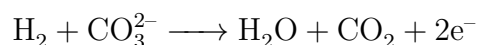
Polymer membrane based AFCs exhibit great potential but are currently in an initial research and development stage with many key issues requiring examination. On a fundamental level, the transport processes have not yet been investigated in detail and especially the reasons for the comparatively low conductivity of HEMs compared to proton exchange membranes are not well understood.
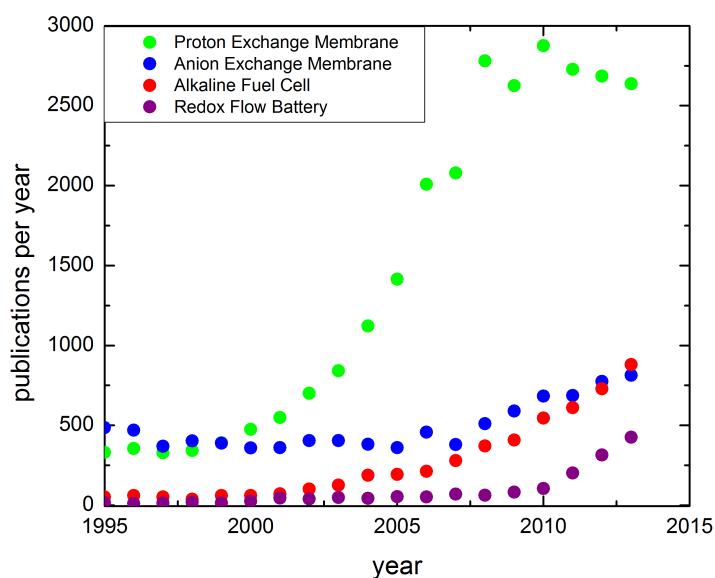
Figure 1.2: Publications per year for four different search terms. While interest in proton exchange membranes has apparently reached a maximum, anion exchange technologies are on the rise. Source: Webofknowledge search on 28.07.2014.

An even more pressing concern is the low alkaline stability of the HEMs themselves, causing membrane degradation above 60 °C and thus membrane failure. The main culprit is considered to be the functional quaternary ammonium (QA) group and more base-stable molecular structures are therefore required.

1.3   The redox flow battery

In a redox flow battery (RFB) the RedOx-active species are not gaseous as in a fuel cell, but dissolved in solution (Figure 1.3). The solutions are pumped along the electrodes from a reservoir of arbitrary size, resulting in considerable advantages with respect to capacity.

Capacity and power output are decoupled and only dependent on reservoir size and electrode area respectively, allowing for enormous capacities. If the pump is turned off, idle discharge is virtually zero since the solutions are stored in external containers without contact to each other or the membrane. Power is almost instantly available, containers are not required to be pressurized and the battery can be quickly recharged by exchanging the

electrolyte. Many different ion pairs for a widely varying potential range can be utilized, all of course with their individual advantages and drawbacks. Examples for some RedOx flow systems include the RedOx couples $(V^{2+};V^{3+}/VO_2^+;VO^{2+})$, $(Fe^{2+};Fe^{3+}/Cr^{3+};Cr^{2+})$, $(Fe^{2+};Fe^{3+}/Ti^{4+};Ti^{3+})$, $(VBr_3;VBr_2/Cl^-;BrCl_2^-)$, $(Br^-;Br_2/Zn^{2+};Zn)$, $(Ru^{2+};Ru_3^+/Ru^{2+};Ru^+)$ $(Mn^{2+};Mn^{3+}/V^{3+};V^{2+})$, $(H_2O;O_2/V_3^+;V_2^+)$.[21,22]
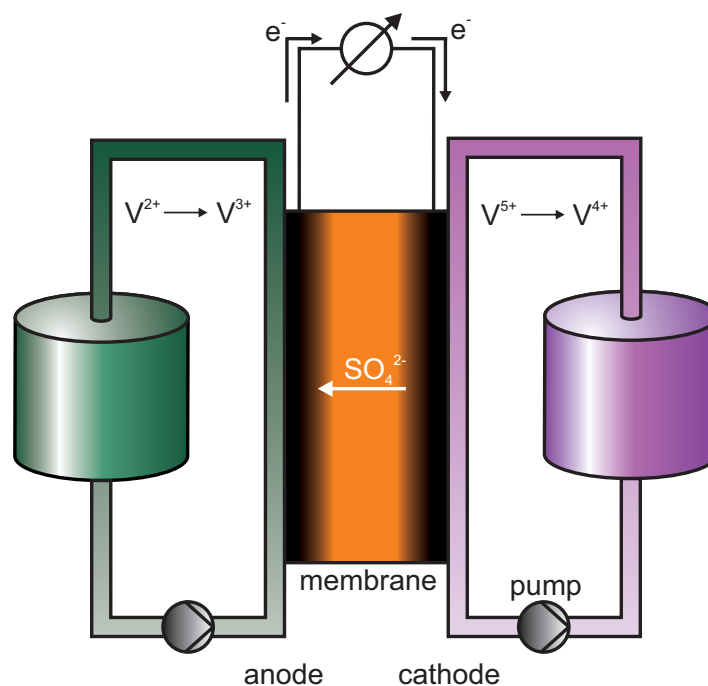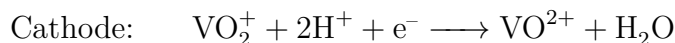

Figure 1.3: Scheme of an all-vanadium redox flow battery during discharge with an AEM. The solutions are acidified by sulfonic acid to increase solubility of the vanadium species, resulting in SO_4^{2-} to be the ionic charge carrier with an AEM.

Electrode reactions for an all-vanadium RFB during discharge:

Anode: $$V^{2+} \longrightarrow V^{3+} + e^-$$

Cathode: $$VO_2^+ + 2H^+ + e^- \longrightarrow VO^{2+} + H_2O$$

Overall: $$VO_2^+ + V^{2+} + 2H^+ \longrightarrow VO^{2+} + V^{3+} + H_2O$$

A drawback of RFBs in general is a capacity loss during load caused by ionic cross-over. For some RedOx couples this results in precipitates or other reaction products that irreversibly lower the capacity of the solutions. In the all-vanadium RFB (VRFB) though, cross-over induced capacity loss is reversible since all ions can be converted to the appropriate RedOx active species during the next charge cycle, which is one of the reasons why the $(V^{2+};V^{3+}/VO_2^+;VO^{2+})$-RedOx couple has attracted considerable attention. A drawback of

the VRFB is the currently low possible energy density due to low vanadium salt solubility.

For the further development of RFB systems, one of the biggest challenges will be the design of separator materials with high permselectivity, i.e. that allow the desired charge carriers to cross over to the other side, while other molecules are retained, especially the electrochemically active species. Particularly, in cases where cations are the RedOx active species, AEMs will be required for efficient cation exclusion due to the Gibbs-Donnan effect.[23]

1.4   Anion exchange membranes

An anion exchange membrane (AEM) consists of polymer chains functionalized with a number of cationic groups. According to IUPAC, such charged polymers are called either ionomers: "polymer[s] composed of macromolecules in which a *small but significant* proportion of the constitutional units has ionic or ionizable groups[...]" or polyelectrolytes: "[...]in which a *substantial* portion of the constitutional units contains ionic or ionizable groups[...]"[24] (Figure 1.4). While the transition between these two definitions is fuzzy, membranes rather fall into the ionomer range, since polyelectrolytes tend to form solutions in the presence of solvent due to their high concentration of ionic groups.
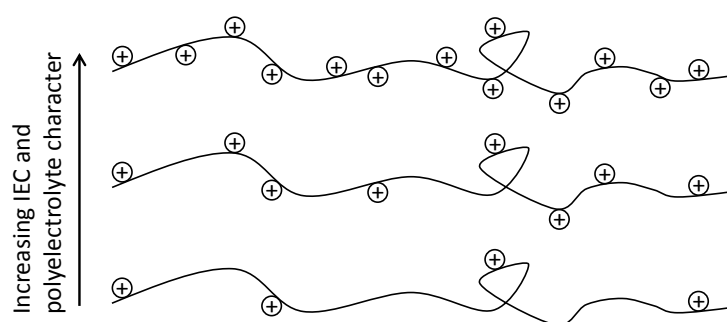
Figure 1.4: Schematic depiction of polycations without counter-ions or solvent. Polyelectrolyte character increases with a higher ion exchange capacity (IEC), i.e. with a higher number of charged groups per mass of the polymer.

Most anion exchangers are made from hydrocarbon polymer backbones with covalently attached quaternary ammonium groups (Figure 1.5). While they are currently investigated for AFCs and RFBs, commercial applications already include e.g. electrodialysis, pharma-

ceutical treatment, HPLC, and water treatment.[25–28] Depending on the application certain properties are required of the ionomer. In AEMs for AFCs these are mechanical stability, good ionic conductivity (especially at high temperature and low humidification), as well as alkaline stability and resistance against radical attack. For RFBs a high permselectivity is required in addition, whereas alkaline stability is generally not.
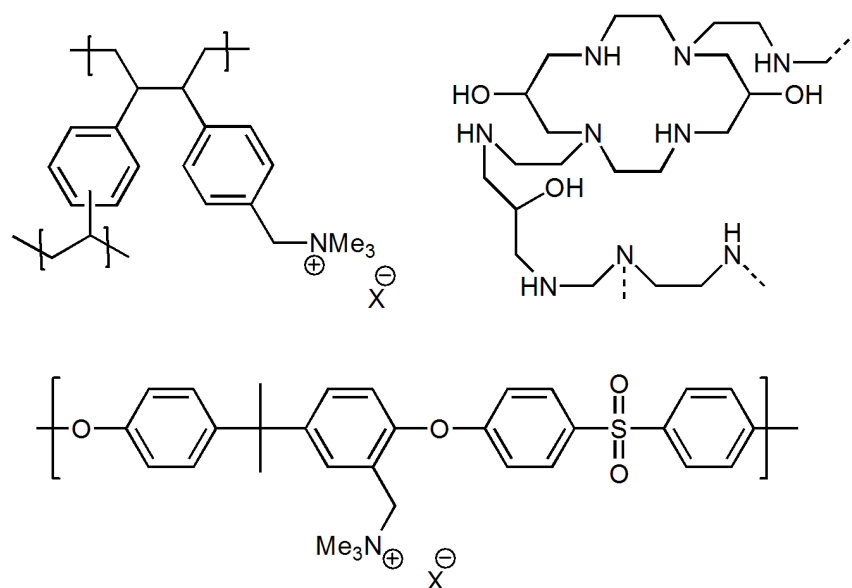

Figure 1.5: Chemical structures of two strong and one weak base anion exchange ionomers. From top left to bottom: Cholestyramine, colestipol (both pharmaceutical substances) and a polysulfone.

These properties are governed by the characteristics of the polymer such as molecular structure, conformation and rotational freedom of the chemical bonds, as well as ion exchange capacity (IEC), which refers to the number of charged functional groups per gram of polymer, the degree of cross-linking, which is the degree to which polymers are covalently interconnected (Figure 1.6) and the molecular weight, which is related to the length of the polymer chains.

Careful balancing of these properties is required to achieve certain desired attributes, which benefits from an understanding of the involved physical and chemical processes. This is a substantial challenge since ionomer membranes are inhomogeneous and irregular materials on the nano-meter scale that are prone to change in composition (e.g. water content) and morphology with e.g. temperature, relative humidity and lifetime.

The aim of this work is to elucidate some of the transport processes of water and ions in AEMs, as well as investigate the alkaline stability of their functional quaternary ammonium
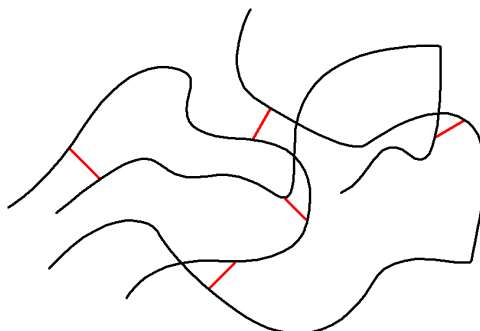
Figure 1.6: Sketch of polymer chains with chemical cross-links that give mechanical stability and reduce swelling marked in red. The chosen FAA-3 AEM in this work does not contain such cross-links to allow access to a wide water content range.

groups. Special focus lies on hydroxide form membranes for AFCs, as no investigation of carbonate free HEMs outside of liquid water has been conducted so far and state-of-the-art materials are chemically unstable in high pH environments. As such, this is one step towards viable polymer membrane based AFCs and RFBs as power storage and conversion devices.

For this thesis a commercial FAA-3 (FuMA-Tech) membrane, which contained no chemical cross-links and came from a single production batch was used for all transport experiments. This ensured that samples only differed with respect to the kind of anion and the water content. A non cross-linked membrane was chosen to have access to a large water content range.

Chapter 2

Theoretical background

2.1 Alkaline degradation of quaternary ammonium groups

2.1.1 General aspects

An anion exchange material requires positively charged groups on the polymer backbone to function as membrane or resin in separation or ion exchange processes. If the positive charges are neutralized for whatever reason, the anion exchanger loses its function and becomes inoperative.

This is a critical current issue with hydroxide exchange membranes (HEM), in which the highly nucleophilic hydroxide counter ion attacks both the positively charged functional quaternary ammonium (QA) groups and the polymer backbone.[26,29–36] Specifically the cation degradation is considered to be the main reason why contemporary HEMs rapidly lose performance beyond 60 °C. AFC applications using HEMs will be severely limited as long as this degradation can not be reduced to acceptable levels at elevated temperatures.[9,10,18,20]

Alternative elements such as phosphonium or sulfonium as basis for cationic functional groups were found to be less stable with similar substituents (stability trend: NR_4^+ >

$PR_4^+ > SR_3^+$).[37,38] While this does not necessarily mean that only QA is a viable option, the notable examples of alternative cations which exhibit QA-comparable stability consist of rather exotic structures based on phosphonium with extremely bulky substituents or transition metal complexes with large ligands (Figure 2.1) that require a complex and expensive synthesis.[37,39–41]
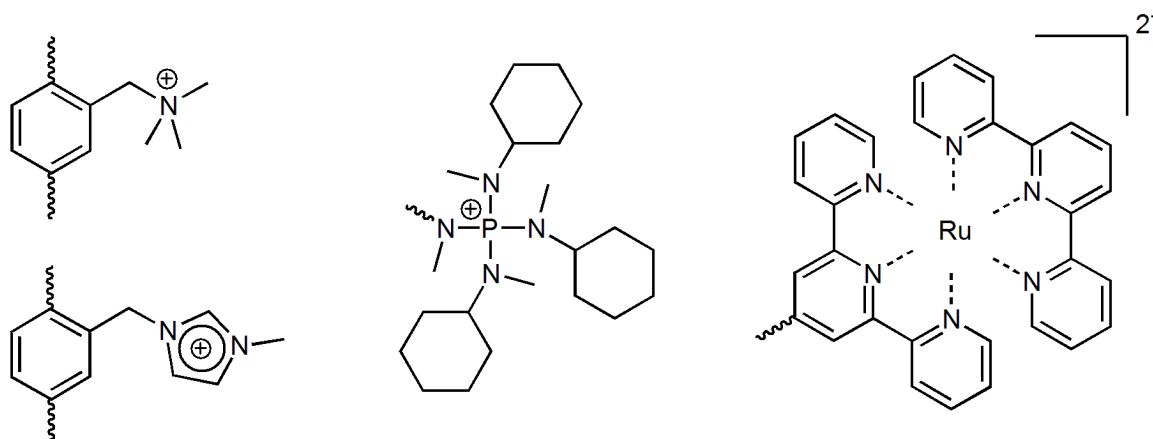
Figure 2.1: Structures of commonly used quaternary ammonium (QA) groups together with some more exotic cations[37,40] as potential functional groups in anion exchange membranes.

Since the advantage of cheap platinum-free AFCs would be counteracted by expensive cations, QA groups are usually chosen as they are not only comparatively simple to synthesize but also easily attached to a polymeric backbone. For these reasons this work will focus exclusively on QA based functional groups and seek those structures that are comparatively inert against the various degradation reactions which occur in the presence of hydroxide.

2.1.2 Degradation mechanisms

The main degradation pathways of QA compounds in the presence of a strong base such as hydroxide are nucleophilic substitution and β-elimination (Figure 2.2).[26,32] In the substitution reaction hydroxide attacks an α carbon, then the molecule proceeds through a trigonal bipyramidal transition state resulting in amine and alcohol reaction products. The β-elimination (a.k.a. Hofmann elimination) requires the presence of a proton in β position which is then abstracted by hydroxide, proceeding through a transition state that resembles
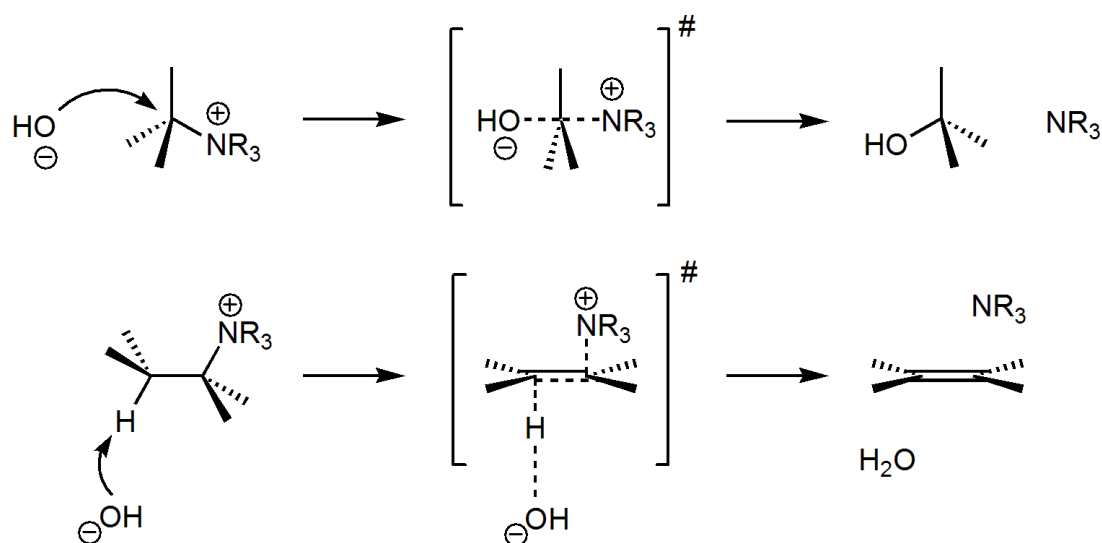
Figure 2.2: S_N2 Nucleophilic substitution (top) and Hofmann elimination (bottom) of a quaternary ammonium in the presence of hydroxide, including transition states. Hydroxide attacks at α-carbon and β-proton, respectively.

both products and starting materials after which an alkene, amine and water are created. The characteristic strong fish-like smell of the amine product is an unambiguous way to detect the degradation of the cations and respective membrane materials.

While substitution and elimination can be considered to be the most critical degradation pathways, other reactions are known to occur as well depending on the molecular structure. In the absence of β-protons these are for example Stevens rearrangement or, with aromatic compounds, Sommelet-Hauser rearrangement or ortho-attacks (Figure 2.3). [42–44]

These degradation pathways tend to compete with each other, especially substitution and elimination. The dominating reaction is prone to change depending on cation structure, solvent and temperature. [45–47] Slowing down one reaction pathway may well speed up another, resulting in a non-trivial relation between molecular structure and alkaline stability.

The β-elimination for example becomes increasingly favored with higher temperatures and proceeds much more rapidly if nuclophile and leaving group are able to rotate into an anti periplanar position (180° angle between both groups). S_N2 substitution on the other hand is inhibited by large substituents attached to the nitrogen that hinder the approach of OH⁻ to the α-carbons. [45–47]

For a given reaction pathway to proceed a certain activation energy is required that de-
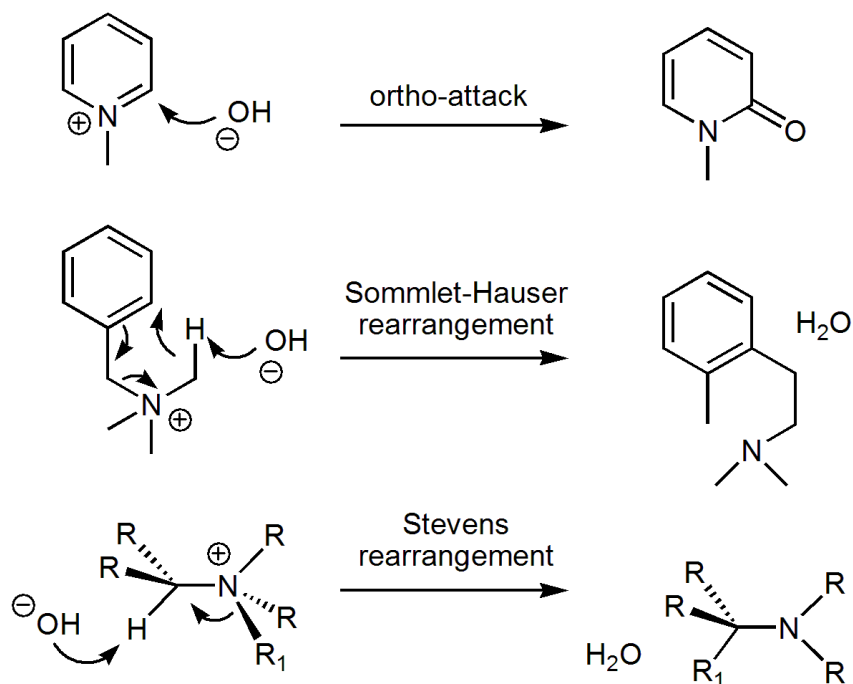
Figure 2.3: Further degradation mechanisms for different quaternary ammonium structures.

pends on the difference between the energy of the starting materials and the transition state (Figure 2.4). Since the total energy of the starting materials (QA and hydroxide) is expected to be higher than that of the reaction products (alcohol, alkane, alkene, water) any kind of stabilization is expected to be kinetic instead of thermodynamic.

The reaction rate of the above degradation processes in Figures 2.2 and 2.3 is expected to follow a second rate order. To compare the relative and absolute kinetic stabilities at given conditions for all investigated compounds, their rate constants have to be determined. The reactions are of the type

$$A + B \xrightarrow{k_2} C$$
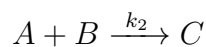
with A and B as reactants, C the reaction products and k_2 the reaction constant. The change of the concentration of A with time is dependent on k_2 and the concentration of B.

$$-\frac{d[A]}{dt} = k_2 \cdot [A] \cdot [B]$$

For the first case of $[A] \neq [B]$, this gives the following expression after integration.

$$[A] = [A]_0 \cdot \frac{[A]_0 - [B]_0}{[A]_0 - [B]_0 \cdot e^{([B]_0 - [A]_0)k_2 t}}$$
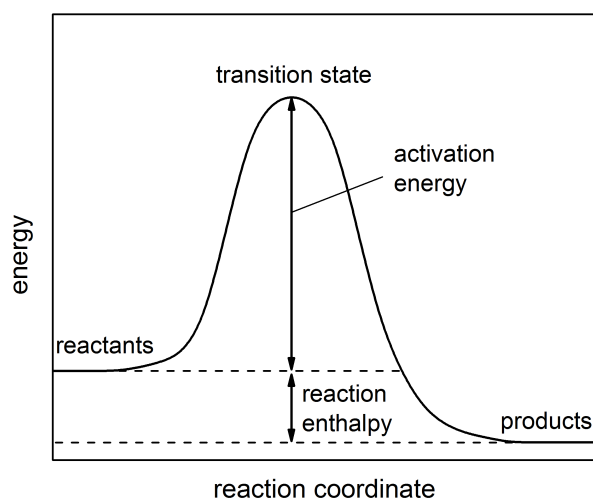
Figure 2.4: Energy profile of a typical chemical reaction.

For the second case of $[A] = [B]$ a simpler form can be derived.

$$[A] = \frac{1}{2 \cdot k_2 t + 1/[A]_0}$$

In the first case, the half life $t_{1/2}$ is different with respect to A and B. For A it corresponds to the following equation (for B, the variables $[A]_0$ and $[B]_0$ have to be swapped):

$$t_{1/2}^A = \frac{\ln \frac{2[B]_0 - [A]_0}{[B]_0}}{k_2([B]_0 - [A]_0)}$$

If $[A] = [B]$, the half-life is:

$$t_{1/2} = \frac{1}{k_2 \cdot [A]_0}$$

For our purpose, the second case does not apply and the first case can be simplified considerably. Since one of the reactants is used in excess (here: B or OH^-) and remains virtually unchanged during the reaction, $[B] = [B]_0$ is a constant and can be included in an effective reaction rate constant $k_1' = k_2 \cdot [B]_0$. The reaction is then of the type

$$A \xrightarrow{k_1'} C$$
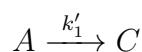
which follows a pseudo-first order reaction rate law.

$$-\frac{d[A]}{dt} = k_1' \cdot [A]$$

After integration the following time dependency for A is received:

$$[A] = [A]_0 \cdot e^{-k_1' t}$$

Accordingly, the effective half-life of the reaction is:

$$t_{1/2} = \frac{\ln 2}{k_1'}$$

While this is comparatively straight-forward, experiments investigating QA degradation rates have shown that the determination of reliable degradation rates is far from simple.

2.1.3 Determining quaternary ammonium group degradation

To determine the degradation of a QA it is necessary to measure its concentration at sufficiently short time intervals. In the membrane form this is usually done by measuring conductivity or IEC after some time in a caustic environment. Unfortunately, widely varying and even conflicting results are reported in the available literature (Figure 2.5) suggesting that this type of experiment may be more difficult than anticipated.

The most notable current example of this is a controversy regarding the stability of aromatic guanidinium and imidazolium functional groups, which were reported to be both more[48,50,51] and less[31,33,34,49,52,53] stable than trimethylammonium in hydroxide exchange membranes.

A likely cause for this is the considerable complexity introduced by the polymer membrane. The reactivity of the QA may be significantly affected by the chemical nature of the backbone it is attached to, the degree of functionalization (i.e. IEC), the water content and the inhomogeneous nature of the membrane. In addition to varying experimental conditions this may well explain variances in half-lives found between (but not limited to) 2.7 h and >1500 h[35,54] for similar cations.
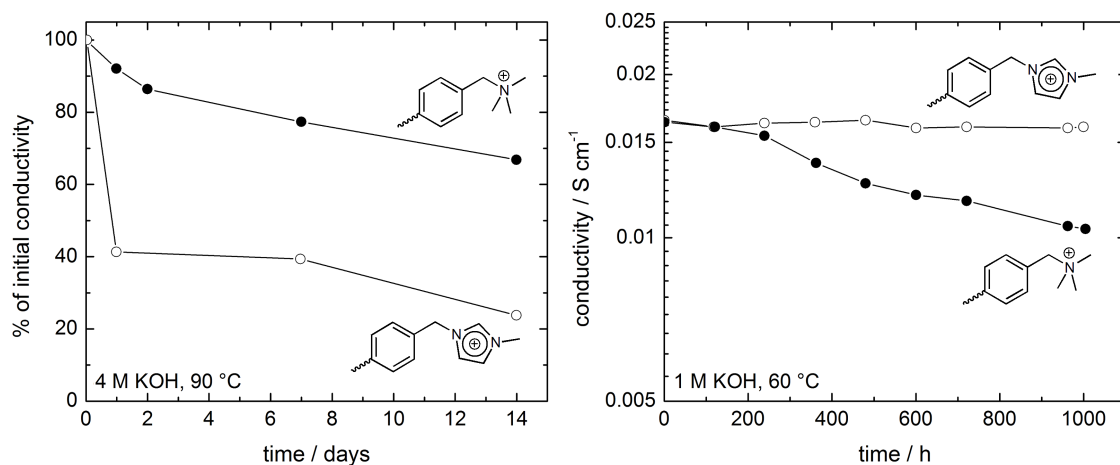
Figure 2.5: Example of two reported opposing results concerning the stability of imidazolium and methylammonium functionalized membrane materials. [48,49]

To remedy these issues related to the polymer backbone the QAs need to be investigated in their simple salt form ($NR_4^+X^-$) in aqueous solution under identical conditions. In this way it is possible to exactly control the number of water molecules per hydroxide, the hydroxide to ammonium ratio and temperature in a homogeneous environment. Determination of degradation rates is much simpler in solution than in a membrane and by keeping QA concentration low inter-cationic interaction can be reduced to a minimum. This makes a discussion of relative and absolute QA stabilities possible, which is based solely on their molecular structure.

The concentration of a QA during a degradation experiment can be determined through UV/Vis spectroscopy, utilizing the fact that the positively charged chrome complex of the ammonium salt $NH_4[Cr(SCN)_4(NH_3)_2]$ known as Reinecke's salt (RS), precipitates quantitatively with large cations such as cadmium, mercury and also tetraalkylammonium in the reaction:[55–58]

$$NH_4[Cr(SCN)_4(NH_3)_2] + NR_4^+ \longrightarrow NH_4^+ + NR_4[Cr(SCN)_4(NH_3)_2] \downarrow$$
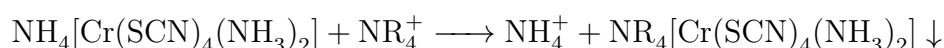
Since RS solutions are strongly violet and display an undistributed absorption maximum at 520 nm, a calibration curve can be recorded using the Beer-Lambert law (Figure 2.6). By precipitating a known concentration of RS ($[RS]_0$) with a QA degradation sample, the

leftover $[QA]$ can be calculated from the residual $[RS]$ according to the simple formula:

$$[QA] = [RS]_0 - [RS]$$

If the concentration decays logarithmically over time (Figure 2.7), the reaction follows a pseudo-first order kinetic and the slope of the curve corresponds to the effective reaction rate k_1', with the half-life of the substance being $t_{1/2} = \ln 2/k_1'$, as outlined above.
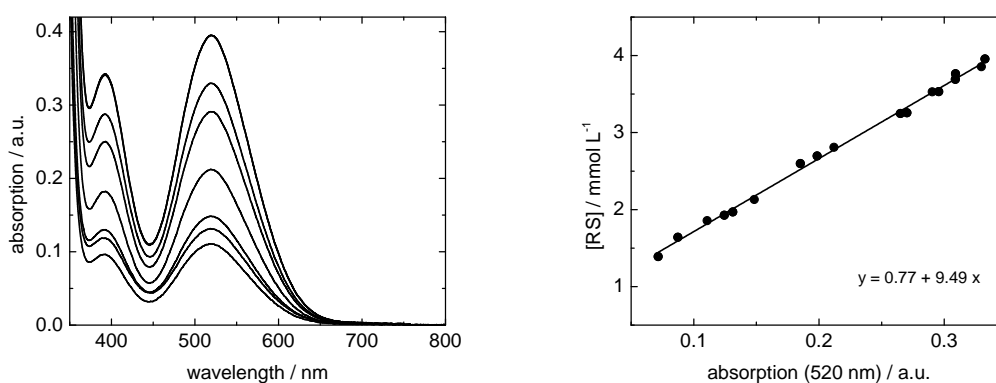

Figure 2.6: On the left the absorption spectra of RS solutions with varying concentrations are displayed. The absorption maximum at 520 nm can be used to draw a calibration curve as shown on the right with which the QA concentration in a given solution can be determined.
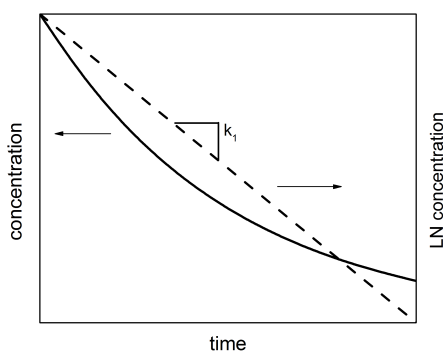
Figure 2.7: If the concentration decays logarithmically with time (dashed line) the slope corresponds to the effective reaction rate constant k_1'.

2.1.4   Stabilizing the quaternary ammonium

To stabilize a QA in an alkaline environment the degradation reactions have to be suppressed or inhibited completely. This might be achieved through specific molecule structures that are resistant against the various attack pathways of the hydroxide anion. In the following a brief literature discussion will outline previous stabilization approaches and examine their advantages and drawbacks.

All degradation pathways and especially substitution reactions that take place at the α-carbon can in principle be slowed down by sterically shielding the reaction center with bulky substituents. The problem with this approach is that increasingly bulky ammonium groups are difficult to synthesize, since the ammonium ion is relatively small and the space around it limited. Additionally, bulky ammonium groups are difficult to attach to a polymer backbone since their nucleophilic characteristic required for substitution decreases with large substituents. Excessive steric shielding of the positive charge is more suited for cations other than nitrogen, such as phosphorus or metal complexes as those shown in Figure 2.1.

For quaternary ammonium groups one of the most important stabilization strategies is the inhibition of β-elimination through the removal of all β-protons which also removes any possibility for this reaction pathway. Since elimination is considered to be one of the fastest degradation reactions, this can in principle greatly increase alkaline stability. Structures that are examples for this approach are benyzltrimethylammonium (BTM) groups frequently encountered in literature and neopentyl based QAs which have recently received some attention as well (Figure 2.8).[59,60]
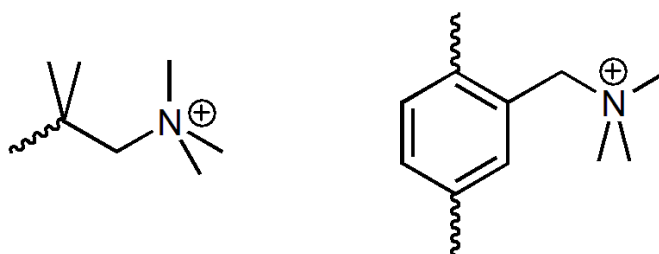
Figure 2.8:   A neopentyltrimethylammonium (NTM) and a benzyltrimethylammonioum (BTM) functional group containing no β-protons to avoid elimination. Wavy bonds mark potential attachment sites to a polymer.

While this strategy precludes β-elimination, alternative pathways such as rearrangement reactions may emerge, especially with benzylic or other aromatic substituents (Figure 2.3). It is therefore difficult to predict whether β-removal will result in slower or faster decomposition without experimental verification or at least simulations.

Another approach intended to slow down elimination that does not require the removal of β-protons is rotationally constraining the C-C bond between nitrogen and proton involved in the elimination into a geometry in which the anti-periplanar position (180° angle between nitrogen and hydrogen), which facilitates elimination, is not available.

This can in principle be achieved through ring or cage-like structures based on e.g. diaza-bicyclooctane (DABCO) or pyrrolidine that force the β-protons into a somewhat ecliptic position (Figure 2.9). A drawback of such structures may be their inherent ring-strain necessary for the β-proton constraint and the higher energy of an ecliptic configuration compared to an anti-periplanar one. Since this raises the QA energy, the activation energy for any degradation mechanism is reduced accordingly. Previous researchers reported DABCO based compounds to be comparatively stable ammonium groups,[30,61,62] but other heterocyclic QAs have received little to no attention.
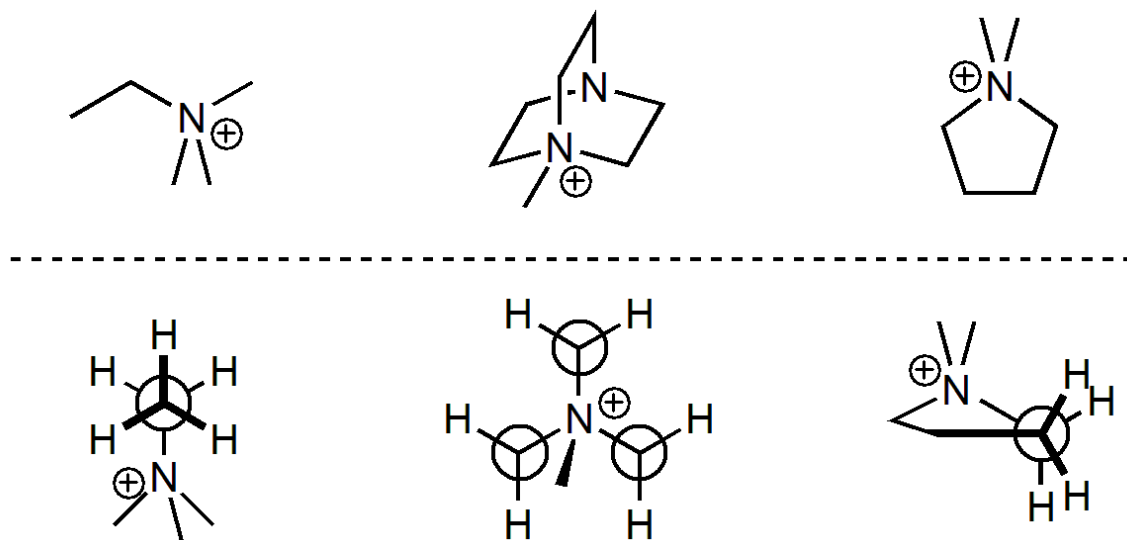
Figure 2.9: In ethyltrimethylammonium (ETM) the β-protons can easily rotate into an 180° anti-periplanar position with respect to nitrogen, facilitating elimination. This is not the case for DABCO (middle) or pyrrolidine (right) based compounds, better visible in the Newman projections below the dashed line.

A completely different attempt to stabilize the QA is the delocalization of the charge

in aromatic functional groups such as imidazolium or guanidinium. This reduces charge density and electrophilicity of the cation, since the charge is distributed between several atom-orbitals (Figure 2.10). Some examples of QAs with aromatic structures are shown in Figure 2.11.
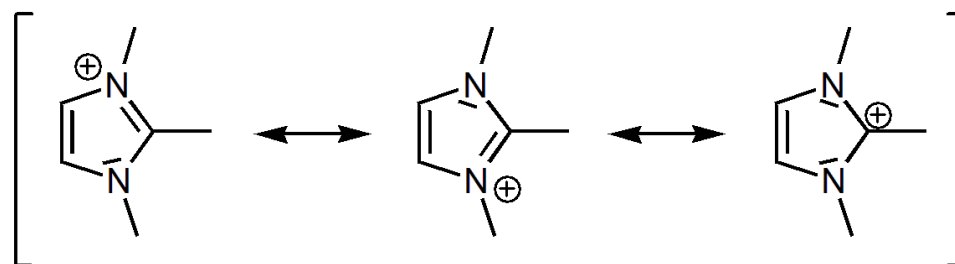

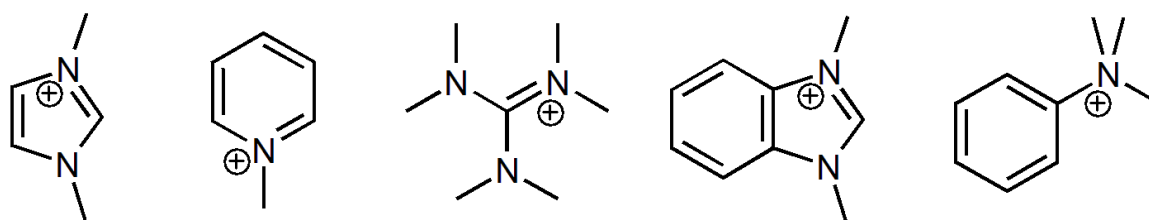**Figure 2.10:** The positive charge is delocalized over several atoms in an aromatic QA.

Figure 2.11: From left to right: Imidazole, pyridine, guanidine, benzimidazole and phenyl based ammonium cations.

Problems may arise through the necessarily planar geometry that exhibits almost no steric shielding, allowing hydroxide to approach closely from above or below the aromatic plane (Figure 2.12). The increased reactivity of neighboring protons due to the aromatic stabilizing effect on radicals and carbanions is a further potential issue. The question is whether the increased stability gained by delocalization can sufficiently compensate the drawbacks.

Some promising works have been published suggesting surprisingly stable aromatic QAs, though their validity is unclear yet,[48,50,51] especially with the background knowledge that e.g. polybenzimidazoles are known to decompose rapidly in alkaline environments even at comparatively mild conditions.[63]

Apart from delocalization, aromatic structures are especially suited for another way to reduce hydroxide induced degradation, namely the introduction of electron inducing groups to increase electron density in the vicinity of the ammonium. Since the ammonium ion is
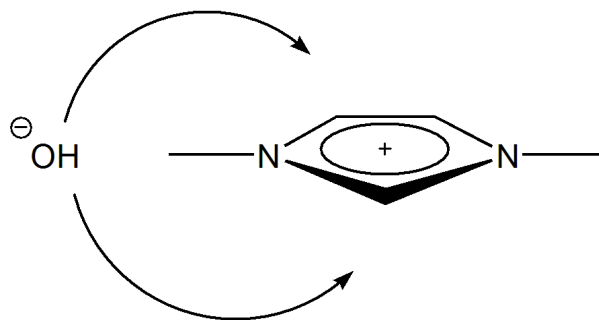
Figure 2.12: Aromatic QAs are necessarily planar and lack steric shielding as a consequence.

itself electron deficient, this can be expected to decrease its susceptibility to nucleophilic attack. Such groups would not necessarily be attached to the ammonium directly but could be part of the polymer structure.

Beside the QA group itself and the nature of the backbone, the way the QA is attached to the polymer likely has a noticeable effect on its stability as well. While this could have been included in the discussion of the variances of the ammonium substituents, special mentioning here seems pertinent. That is because recent studies based on a work from 1997 by Tomoi et al. suggested that alkyl-trimethyl ammonium groups attached to a polysulfone polymer backbone via a several carbon atoms long "spacer chain" improved their alkaline stability.[49,64] Curiously, this seems to be independent of whether the ammonium is attached to the end of the spacer chain or between the polymer and the chain itself (Figure 2.13).[49,65]
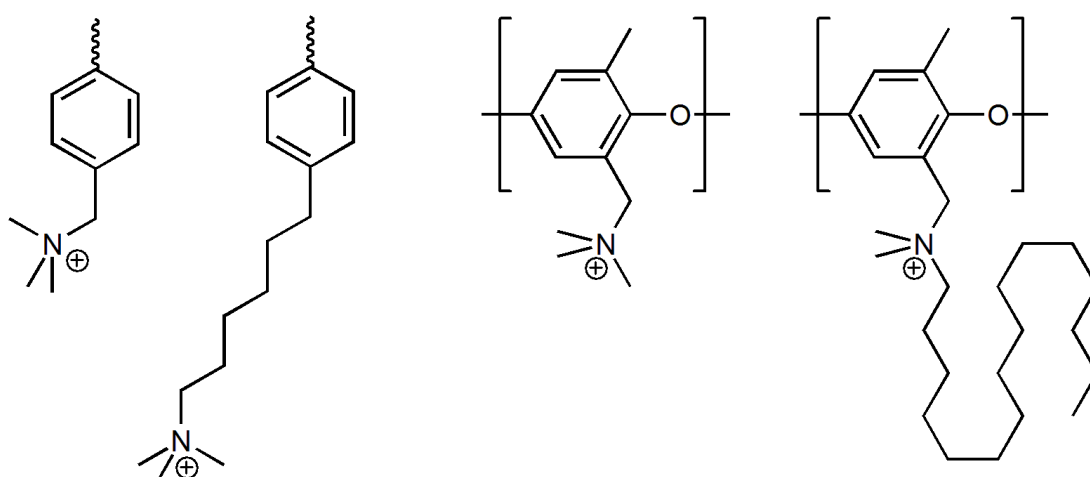
Figure 2.13: Alkaline stability of hydroxide exchange membranes increased, independent of whether the ammonium was attached to the end of the spacer chain, or between the polymer and the chain.[49,65]

A higher stability with increased distance between benzyl and ammonium can be explained by the decrease of the electron withdrawing effect which the aromatic group exerts on the cation. On the other hand, the fact that an alkyl chain also increases alkaline stability if it was not placed between benzyl and ammonium, but is instead only another substituent of the nitrogen atom (Figure 2.13 first structure from the right), can not be explained this way and requires further investigation.

As briefly brought up above, apart from the functional groups at least some polymeric backbones are known to degrade in alkaline conditions as well (Figure 2.14).[35,66] Hydrolysis of quaternary carbon atoms and ether bonds, which are constituent parts of e.g. standard poly(sulfone)s or poly(phenylene oxide)s, appears to be an issue.[35,66] This kind of degradation cleaves the polymer chains and results in a loss of mechanical strength, suggesting that polymers that do not contain such groups are better suited for HEM applications.
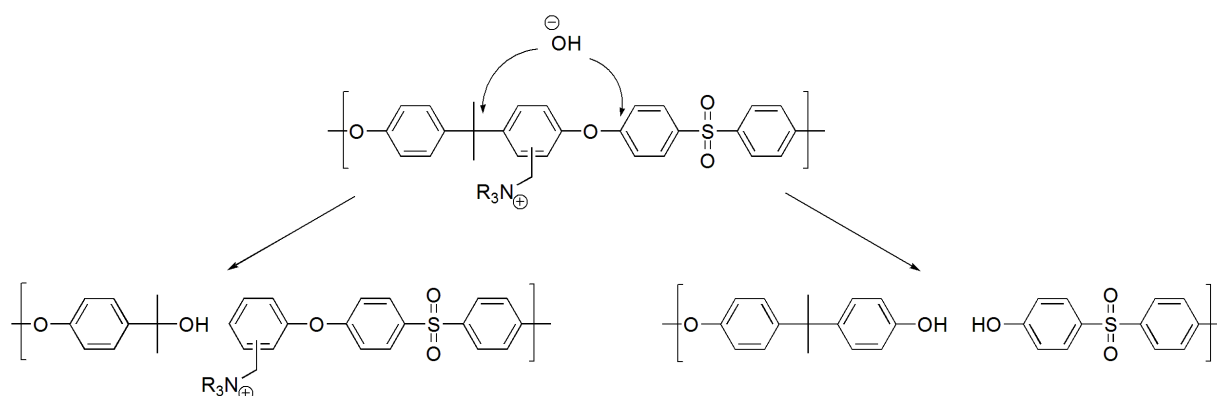
Figure 2.14: Hydroxide induced polymer cleavage of a poly(ethersulfone) was reported to occur at quaternary carbon atoms and ether bonds.[35]

While potentially stable QA compounds and polymers may contain a combination of all the above approaches, they would be difficult to synthesize. The resulting increased effort and cost required to create membranes with such molecules would unfortunately counteract the advantage of comparatively cheap platinum-free alkaline fuel cells.

This is the reason why this work examines relatively simple QAs that are commercially available or easy to synthesize. Apart from an interest in the QA degradation reactions, the intent is to give easily understandable guidelines as to which functional groups, tethers and polymer backbones are beneficial or disadvantageous to membrane alkaline stability to stimulate further development of polymer based AFCs. It should be noted that not only

alkaline stability on which this work focuses, but various other failure modes are important such as radical formation in an operating fuel cell. They also deserve a deeper investigation but this is outside the scope of this thesis.

2.2   Ion and water transport in ion exchange membranes

2.2.1   General aspects

In a low temperature FC or RFB the ionic charge carriers move across a polymer membrane from one electrode to the other. The resistance the ionic current experiences dominates a significant proportion of the cell potential drop at a given current density (see current-voltage curve in Figure 2.15).
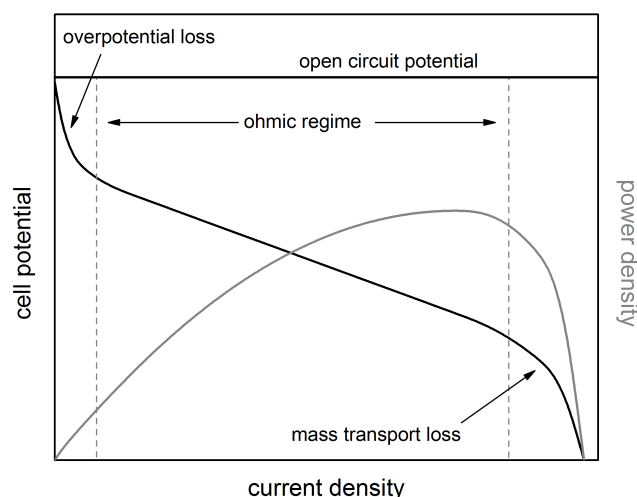
Figure 2.15: Idealized current-voltage diagram of a fuel cell, showing overpotential, ohmic and mass transport regime.

The thermodynamic open circuit potential of 1.23 V in a hydrogen fuel cell is diminished by several types of losses. a) Initial overpotential voltage loss, a consequence of electrode activation energy b) linear ohmic loss regime, which is mainly due to the resistance the ionic current through the membrane experiences, and c) mass transport losses due to insufficient reactants reaching and leaving the electrodes for reaction with the available electrons resulting in a cell resistance approaching infinity and causing rapid potential decay. Increasing the ionic conductivity of a membrane leads to a less steep slope in the ohmic region which is desirable in a FC as this can improve power output considerably.

Ionic conductivity is dependent on the mobility and concentration of mobile ions, both of which are themselves influenced by factors such as temperature, amount and kind of solvent, and – in a membrane – also by the nature of the polymer, its morphology, and ion-solvent-polymer interactions. Apart from the ions, the solvent molecules are moving through the membrane as well because of electro-osmotic drag and gradients in the chemical potential of the solvent (e.g. concentration gradients).

For RFBs, where several kinds of mobile anions and cations exist that can interact and influence the membrane water uptake, specific conduction of anion versus cation (i.e. permselectivity) becomes important as it is beneficial if the electrochemically active species do not diffuse to the other electrode.

2.2.2   Diffusion

The term diffusion is based on the Latin term *diffundere* (meaning: to spread out) and describes the random thermally activated translational movement of particles. These can be for example a molecule in air/liquid, a macroscopic object like a pollen grain in water, ions and water in an ion exchange membrane or even non-particle entities such as defects inside a solid. This process is also termed Brownian motion, being the result of random collisions with other particles.[67]

There are two ways to describe the coefficient of diffusion D. One is by invoking Fick's law, which describes diffusion as induced through macroscopic concentration gradients.[68] The other is the Einstein-Smoluchowski relation, which expresses diffusion as the displacement of particles in the absence of a driving force.

In the latter case, the diffusion coefficient is described as the probability $P(x, \Delta)$ that a randomly diffusing particle is encountered at a distance x away from its initial position after a certain diffusion time interval Δ has elapsed. This probability corresponds to a Gauss distribution (Figure 2.16) with the formula

$$P(x, \Delta) = \frac{1}{z} e^{-\frac{x^2}{2z}}$$

with

$$z = \sqrt{2D\Delta}$$
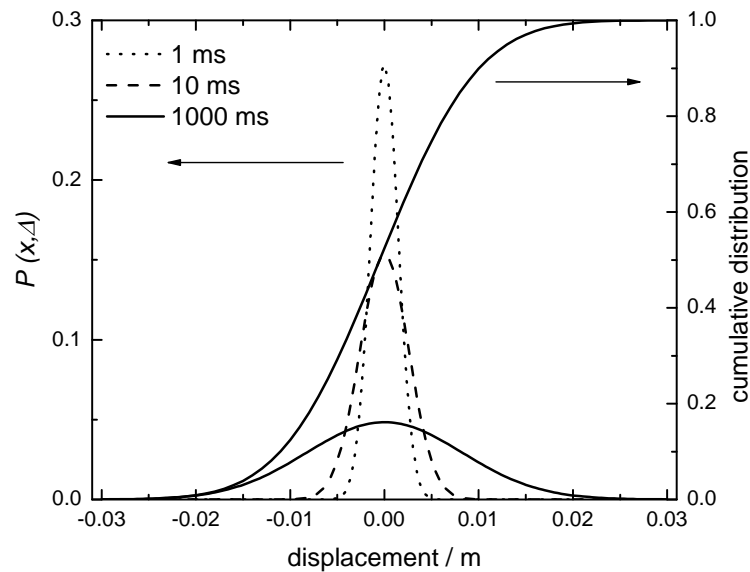
Figure 2.16: Probability of finding a water molecule with $D_{H_2O}= 2.3 \cdot 10^{-9} m^2 s^{-1}$ at a distance x in meters after a diffusion time Δ of 1, 10 and 1000 ms. The cumulative distribution is given for 1000 ms.

For a large number of particles the average diffusional displacement $\bar{x}$ will always be 0 due to its Gaussian nature (see Figure 2.16). The mean square displacement $< x^2 >$ is not zero though, as it is the mean distance each particle has moved away from its original position during the time Δ. For a 3-dimensional system it corresponds to the Einstein-Smoluchowski equation[69,70]

$$< x^2 >= 6D\Delta$$

and if $< x^2 >$ can be determined as a function of the diffusion time, the diffusion coefficient of the particle is simply the slope of the resulting line (see Section 2.3.2). If the diffusing species carries a charge and is contained within an electric field it moves in a preferred direction, resulting in an electric current. By invoking the Nernst-Einstein equation it is possible to calculate the diffusion coefficient of the charged species via its conductivity (see Section 2.3.1). To experimentally determine the diffusion coefficients in these two different ways, pulsed field gradient nuclear magnetic resonance and impedance spectroscopy can be utilized.

2.3   Determining diffusion coefficients

2.3.1   Impedance spectroscopy

Impedance spectroscopy (IS) is used to determine the complex conductivity of electrochemical systems. An alternating current (AC) of varying frequency is applied to a sample. Since the entities in the sample react to the reversal of the current flow with a certain inertia, the sample exhibits not only simple resistive but also capacitive properties. Thereby e.g the polarization of electrons and nuclei or, in the case of this work, the relaxation (i.e. movement) of ions can be studied.

In contrast to a direct current (DC) measurement in which reversible electrodes are required that allow a continuous ion transfer with the electrolyte, for AC impedance, blocking electrodes made from gold or platinum are sufficient as no exchange current is necessary. Furthermore, the frequency dependent response in an AC experiment results in detailed information about the occurring transport processes (e.g. electrode/electrolyte, grain-boundaries, RedOx reactions), whereas DC only gives an effective resistance.

When the current flow inside a circuit is reversed or alternated with a given frequency (ω), its various components respond at different time scales. This corresponds to the circuit either having inductive or capacitive properties in addition to its resistance, with the sinusoidal current (I) ahead or behind the potential (U) by a certain phase angle (θ).[71] Mathematically, impedance is the square root of the sum of the squared real (Z') and imaginary (Z'') resistance

$$|Z| = (Z'^2 + Z''^2)^{1/2}$$

with the phase angle θ being:

$$\theta = tan^{-1}(Z''/Z')$$

IS allows to separate the various contributions with the help of equivalent circuits (EC). In Figure 2.17 the frequency dependent response of an equivalent circuit consisting of a parallel capacitive (C) and resistive element with another capacitor in series is shown with the corresponding EC displayed in Figure 2.18. Such a case and much more complicated situations that potentially combine multiple complex components can be fitted and simulated using appropriate ECs to determine resistances and complex contributions.
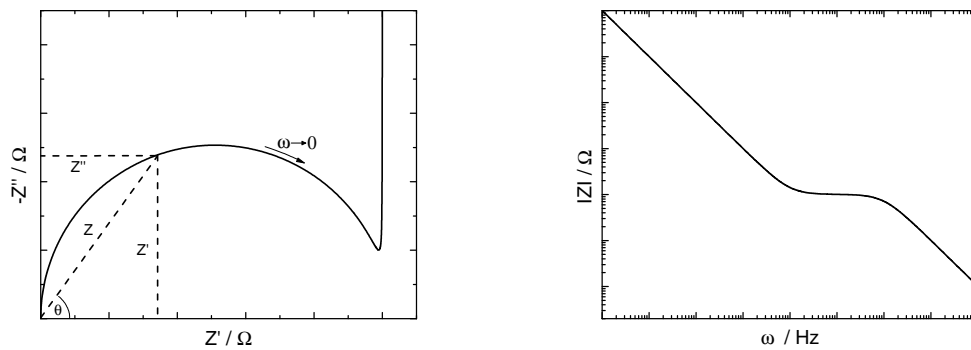
Figure 2.17: Nyquist and Bode plots for the equivalent circuit in Figure 2.18.
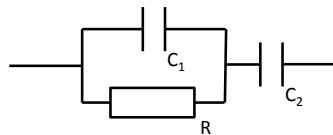
Figure 2.18: Equivalent circuit containing a capacitor and resistor in parallel representing a sample and an additional capacitive element representing blocking electrodes.

For this work the resistance of the ionic contribution was of interest. This ohmic ionic resistance R_Ω of the measured material can then be used to determine conductivity, activation energy, and diffusion coefficient. The ionic conductivity σ is the reciprocal of the resistance R_Ω

$$\sigma = \frac{1}{R_\Omega \cdot G_{form}}$$

with G_{form} as the form factor of the membrane

$$G_{form} = \frac{A}{L}$$

where A = electrode area and L = thickness of the membrane stack in the through-plane measurements that were performed in this work (Figure 2.19).

Once the conductivity of a sample is determined it is possible to calculate the conductivity diffusion coefficient D_σ with help of the Nernst-Einstein equation

$$D_\sigma = \frac{\Lambda \cdot R \cdot T}{z^2 \cdot F^2}$$
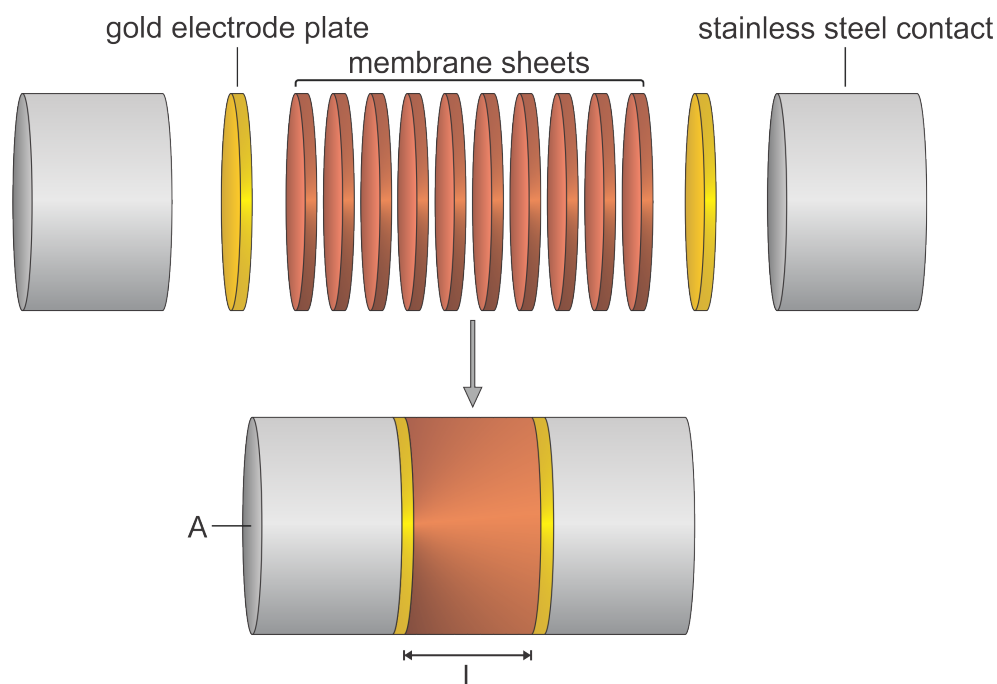
Figure 2.19: The dimensional parameters of the membrane stack made from stamped out membranes that are required to calculate conductivity and diffusion coefficient are electrode or membrane surface area A and membrane stack thickness L.

where Λ = molar conductivity, R = ideal gas constant, z = charge number of the mobile ions, T = temperature and F = Faraday's constant. For ions with a single charge ($z = 1$) the above equation becomes:

$$D_\sigma = \frac{\Lambda \cdot R \cdot T}{F^2}$$

By substituting the molar conductivity $\Lambda = \sigma/[X^-]$, with $[X^-]$ as the concentration of all anions in the sample we receive

$$D_\sigma = \frac{\sigma \cdot R \cdot T}{[X^-] \cdot F^2}$$

where $[X^-] = n_{X^-}/V$ with n_{X^-} as the number of anions in the volume V of the sample and the volume V calculated from $V = A \cdot L$. Substituting the concentration gives the formula:

$$D_\sigma = \frac{\sigma \cdot R \cdot T \cdot V}{n_{X^-} \cdot F^2}$$

Since n_{X^-} is the product of ion exchange capacity IEC and dry membrane weight m_{dry}, it

is possible to further substitute $n_{X^-} = m_{dry} \cdot \text{IEC}$ to receive

$$D_\sigma = \frac{\sigma \cdot R \cdot T \cdot V}{m_{dry} \cdot \text{IEC} \cdot F^2}$$

which was used to calculate D_σ throughout this work. D_σ has the unit $[area \cdot time^{-1}]$ and can be directly compared to the tracer diffusion coefficient determined by pulsed field gradient nuclear magnetic resonance.

2.3.2   Pulsed field gradient nuclear magnetic resonance

Pulsed field gradient nuclear magnetic resonance (PFG NMR) measures the tracer diffusion coefficient of diffusing nuclei with a nuclear magnetic moment.[72] This model free method does not require the determination of ion concentration, sample dimension, or weight.

NMR takes advantage of the fact that nuclei with a spin of $I \neq 0$ have a spin magnetic moment μ with $m = 2 \cdot I + 1$ degenerate energy states E_m, which split in an external magnetic B_0 field in z-direction (Zeeman effect). The energy state is dependent on the gyromagnetic ratio γ of the nucleus and B_0:

$$E_m = -\gamma B_0 \hbar m$$

With the reduced Planck constant $\hbar$ and the equilibrium population of the states determined by the Boltzmann factor. The magnetic moments precess around the z-axis with a Larmor frequency $\omega_0 = \gamma B_0$ (a rotating reference frame is used that rotates with ω_0) and create a measurable equilibrium magnetization in z-direction (Figure 2.20).[73]

The magnetization is rotated through radio frequency (RF) pulses. After an RF pulse the magnetization returns to its equilibrium state, with the components that are in parallel (longitudinal) and perpendicular (transversal) to the B_0 field affected by the T_1 and T_2 time respectively. A 180° RF pulse inverts the magnetization (Figure 2.21) and the time t the magnetization $M(t)_z$ requires to return to equilibrium $M(t)_{eq}$ is exponentially dependent on the T_1 time (spin-lattice relaxation).

$$M(t)_z = M(eq)_z \cdot (1 - 2 \cdot e^{\frac{-t}{T_1}})$$
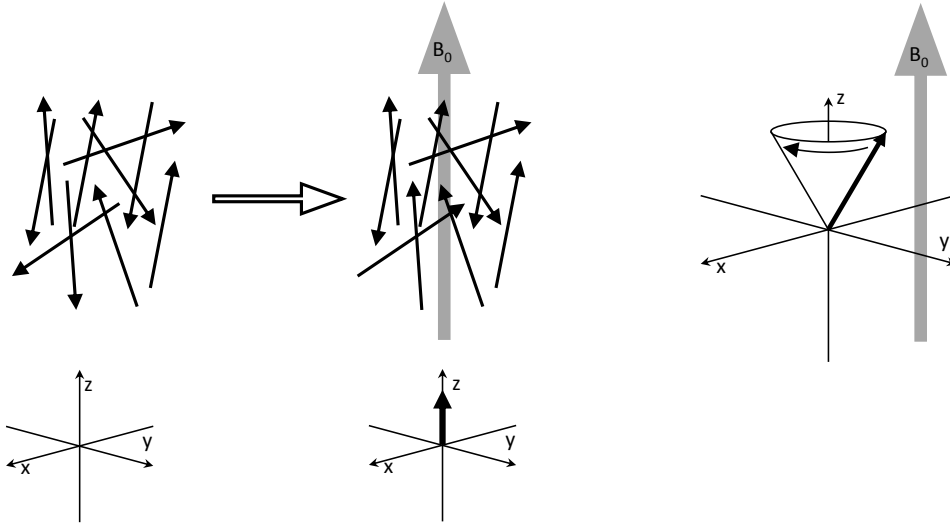
Figure 2.20: The randomly oriented individual magnetic moments align along the axis of an applied magnetic B_0 field (top left), resulting in a magnetization in the same direction at equilibrium (bottom left). The magnetization of the individual nuclei precesses around the z-axis with a given Larmor frequency (top right).

A 90° pulse rotates the magnetization from z-direction into the x,y-plane $M(t)_{xy}$, were they rotate with a Larmor frequency ω_{eff}. If all spins in the transversal plane rotate with the same Larmor frequency they are in phase, but due to minute difference in the effective Larmor frequency ω_{eff}, caused by the local environment of the nuclei, they dephase. This causes the transversal magnetization $M(t)_{xy}$ to exponentially return to equilibrium with T_2 (spin-spin relaxation, Figure 2.21).

$$M(t)_{xy} = M(eq)_{xy} \cdot e^{\frac{-t}{T_2}}$$

By applying a magnetic field gradient of strength g in z-direction in addition to B_0, the Larmor frequency ω_{eff} of the spins becomes a function of their position on the z-axis, since the effective field strength B_{eff} is now z-axis dependent ($\omega_{eff} = \gamma \cdot B_{eff}$). The implication of this is that ω_{eff} can be used as a tool to determine how far the nuclei diffuse during a defined time interval. To do this in this work the spin-echo and stimulated-echo experiments were used (Figure 2.23).

In the spin-echo (SE) experiment the macroscopic magnetization is rotated by a 90° pulse into the x,y-plane. A gradient pulse of duration δ is applied during the first delay time τ. If the center of the gradient corresponds to the center of the sample, the spins below and above this point experience an increasingly positive or negative change in ω_{eff}, due to the
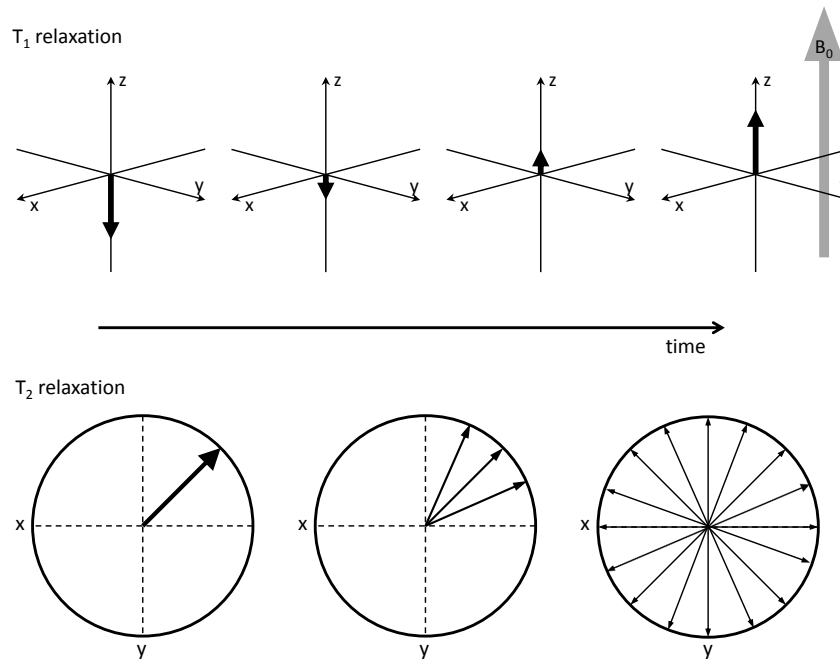
Figure 2.21: Illustration of the magnetization behavior in a T_1-inversion recovery relaxation after a 180° RF pulse that inverted the magnetization, and in a T_2 spin-spin relaxation after a 90° pulse which deflected the magnetization by the respective angle.
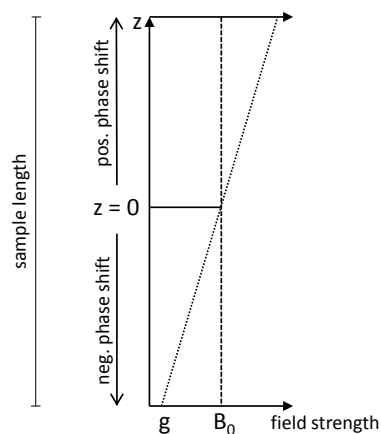
Figure 2.22: Visualization of the change in the gradient field strength g along the z-axis in addition to the homogeneous B_0 field. Above and below $z = 0$, the spins experience phase shifts in opposite directions due to the gradient (see also Figure 2.24).
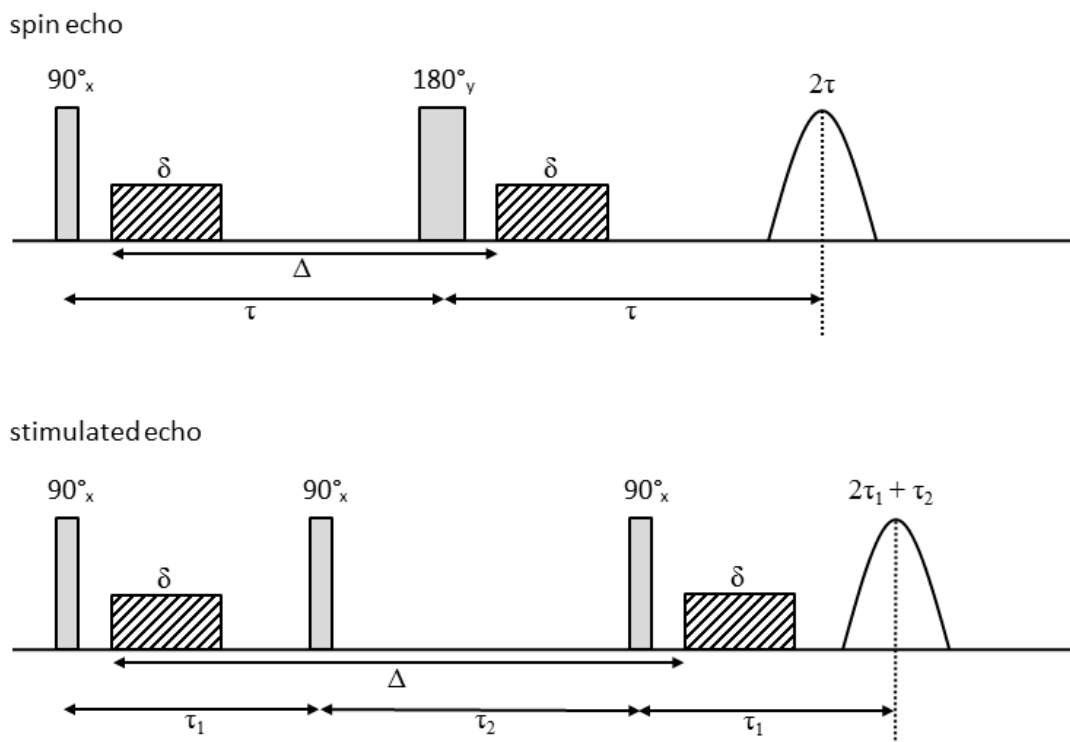
Figure 2.23: PFG NMR spin echo (SE) and stimulated echo (STE) pulse sequences.

sign and strength of the gradient (Figure 2.22). At the end of the first delay time τ a 180° pulse is applied, inverting the sign of the Larmor frequency, followed by a second gradient pulse identical to the first.

In the absence of diffusion (i.e. random translational movement) of the nuclei along the z-axis, ω_{eff} for the spins at the two gradient pulses is the same and all spins refocus according to T_2 relaxation with echo intensity I_0. If diffusion occurs during the time Δ, ω_{eff} is different at the first and second gradient pulse, due to the different field strengths the nuclei experience. This causes a dephasing of the spins which is proportional to the displacement of the nuclei along the z-axis. Accordingly, the refocussing and consequent echo intensity I at 2τ is attenuated (Figure 2.24).

The STE experiments works in a similar fashion, with the difference that the magnetization is rotated into the z-axis after the first gradient pulse at the end of τ_1. During τ_2 the magnetization now decays according to T_1. STE allows one to employ an additional spoiler gradient pulse during τ_2, which eliminates interfering higher order correlations. At the end
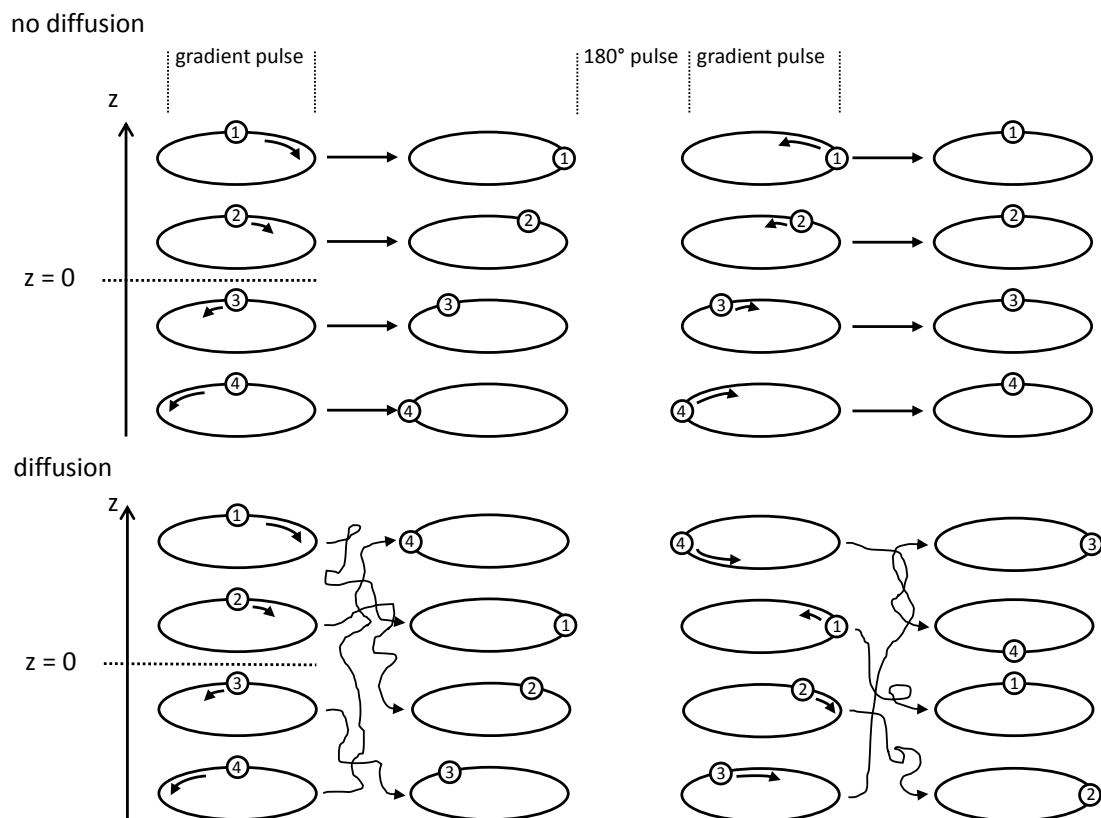
Figure 2.24: A 4-spin ensemble during a PFG experiment with and without diffusion occurring.[72] Without diffusion all spins refocus, resulting in a maximum echo signal. With diffusion, the nuclei will be at different positions along the z-axis at each gradient pulse and accordingly, the spin echo signal will be attenuated.

of τ_2 the magnetization is rotated back into the x,y-plane followed by another gradient pulse, leading to a refocussing of the spins similar to the SE experiment $(90° + 90° = 180°)$.

The echo attenuation is proportional to the root mean square displacement $< x^2 >$ of the nuclei along the z-axis during the time Δ. To determine the diffusion coefficient, the signal attenuation is measured at varying gradient strengths g and plotted according to the Stejskal–Tanner equation[72,74]

$$\frac{I}{I_0} = -\gamma^2 G^2 \delta^2 (\Delta - \frac{\delta}{3}) D$$

where I is the measured signal intensity, I_0 the signal intensity in the absence of gradient pulses, γ the gyromagnetic ratio, g the strength of the magnetic gradient, δ the gradient pulse duration, Δ the diffusion time between the gradient pulses and D the diffusion

coefficient. By plotting the signal intensity over $\gamma^2 G^2 \delta^2 (\Delta - \frac{\delta}{3})$, the diffusion coefficient is received as the slope (Figure 2.25).
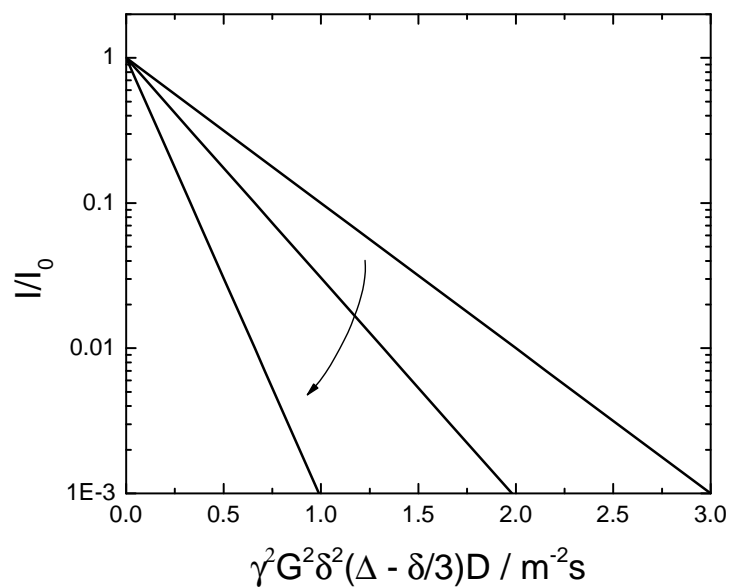
Figure 2.25: A Stejskal–Tanner plot used to determine diffusion coefficients. The diffusion coefficient decreases in the direction of the arrow.

2.4   Morphology of ion exchange membranes

In an AEM the ion and water transport can not occur uninhibited in all directions on the nano scale, in comparison to the case of dilute aqueous solution. In addition, the cations are covalently bound to the polymer backbone and thereby immobilized. In the presence of water the ions can become solvated and the anions dissociate from the immobile cations, i.e. a charge separation occurs. Both the mobile and immobile ions bind water to some extent, separating them from the polymer phase, which leads to a separation of hydrophilic and hydrophobic phases on the nano-meter scale (Figure 2.26). This can only happen due to the covalent polymer-cation bonds, hindering the ions to leave the membrane due to electroneutrality conditions. If this were not the case the ions would leave the polymer membrane and diffuse into the aqueous solution, resulting in two macroscopically separated phases.

Among other factors, ionic interactions are a prominent driving force for the formation of the nano-morphology. Conversely, the nano-morphology can give ideas about the distribution of charges, dissociation, and the formation of ion aggregates. A method with which the nano-morphology can be investigated is small angle X-ray scattering.

2.4.1   Small angle X-ray scattering

With small angle X-ray scattering (SAXS) the nano-meter scale structure of ion exchange membranes can be investigated. The elastic scattering occurs at boundaries with contrasting electron densities in the sample,[75,76] which is different for the polymer and the water phase. SAXS is fundamentally based on the Bragg equation

$$n\lambda = 2d\sin\theta$$

with the spacing between boundaries d, the wavelength λ, the scattering angle θ, and the order of diffraction n. For ionomer membranes, the spacing between boundaries d is the sum of the water and polymer layer thickness, i.e. the correlation length. In comparison to crystalline compounds, the scattering maxima in inhomogeneous amorphous materials such as AEMs are relatively broad due the disorder introduced by variations in the separation length (see Figure 2.26).
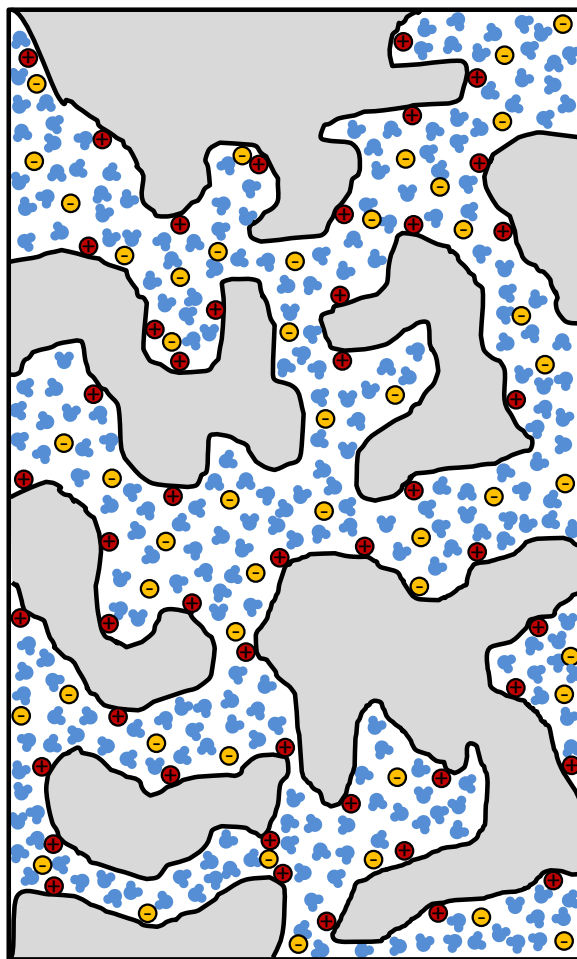
Figure 2.26: Depiction of the nano-morphology of a polymeric anion exchange membrane in the hydrated state. The ion transport occurs in the blue aqueous hydrophilic phase, while the gray polymeric hydrophobic phase give the membrane mechanical stability. Formation of ion-water complexes and details of the polymeric structure are omitted in this figure.

SAXS patterns are usually plotted as the scattered intensity over the angle dependent scattering vector q (Figure 2.27) described by:

$$q = \frac{4\pi}{\lambda} \cdot \sin\theta$$

The correlation length at the maximum scattering intensity q_{max} can be determined by combining the two formulas above ($n = 1$):

$$d = \frac{2\pi}{q_{max}}$$

Unfortunately SAXS can not elucidate all structural features, since many morphological models (e.g. ribbons, columns, tubes) result in the same pattern. For more definite evaluations additional information is required, e.g. from the scaling behavior of the correlation length with water content, conductivity and diffusion measurements. Still, this is not necessarily enough as even for the most investigated membrane material Nafion, the details of its nano-morphology has been debated for decades[77] and termed by some researchers a "never-ending story".
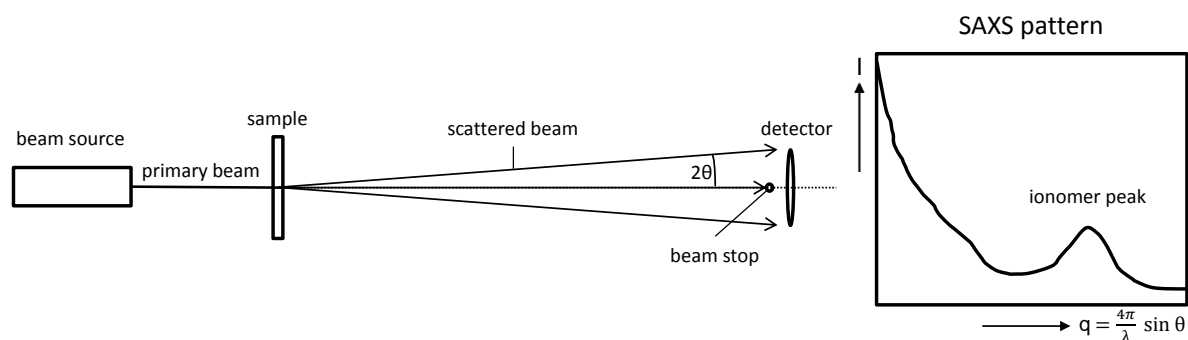
Figure 2.27: Depiction of a SAXS setup with a typical polymer membrane pattern.

Chapter 3

Results and discussion

3.1 Alkaline stability of quaternary ammonium groups

3.1.1 Synthesis of quaternary ammonium groups

A prerequisite for the comparative investigation of quaternary ammonium (QA) compounds is their availability. This required a large number of chemical syntheses since many QAs groups were either commercially unavailable or exceedingly expensive. The chosen reaction to synthesize the QAs was always a nucleophilic substitution of an amine with one or more halocarbons, although experimental procedures and yields varied considerably depending on the phase, reactivity, and stoichiometry of reactants. Because the required halocarbons are highly toxic and even cancerous (especially methyl iodide) great care had to be taken to avoid contact and contamination.

Figure 3.1 shows three reactions for this substitution with methyl iodide, 1-bromopropyl and 1,5-dibromopentyl used to synthesize MAABCO (1-methyl-4-aza-1-azoniabicyclo[2.2.2]-octane), PTM (propyltrimethylammonium) and ASU (6-azonia-spiro[5.5]undecane) respectively. A list of all reactions including yields is shown in Table 3.1. Generally, the bigger the residues on the reaction centers, the more inhibited the reaction, resulting in lower yields. This becomes apparent when high yield reactions of trimethylamine with ethyl bromide or propyl bromide are compared to triethylamine with benzylchloride. The comparatively large benzyl and especially ethyl groups inhibit the reaction from occurring at a fast rate,

resulting in a comparatively low yield.
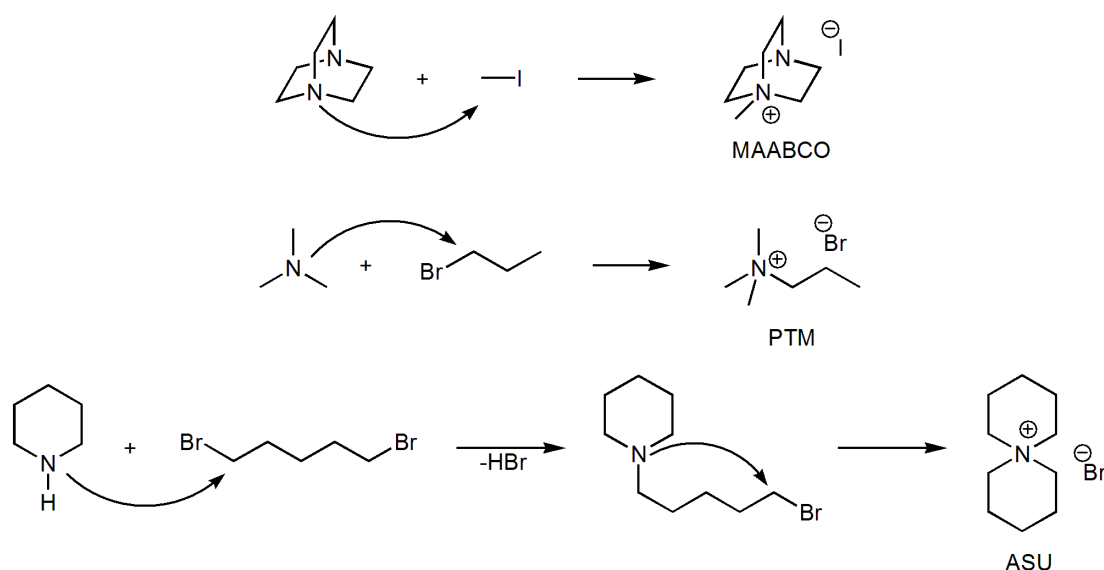
Figure 3.1: Three examples for the synthesis of different QAs.

The nucleophily of the amine which is in relation to its basicity, and the electrophily of the halocarbon has to be taken into account as well. Most simple amines have a pK_A of around 10 (of the conjugated acid) and aromatic functions tend to reduce this value, either by delocalizing the free electron pair or by decreasing the p-character of the sp-hybridization. Both lead to a reduction of the nucleophilic character of the amine, reducing reactivity and corresponding yield, which can be found for TMI (1,2,3-trimethylimidazolium) and BP (N-benzylpyridinium) synthesis.

It should be noted that the low yield of DTG (1,1-dibenzyl-2,2,3,3-tetramethylguaninidi-nium) is not due to its lower basicity, as it is an exeption to the aromats in which the delocalization actually increases basicity, with the pK_A of tetramethylguanidine almost being 14.[78] In this case the low yield of the reaction is due to the inefficient purification process which required several recrystallization cycles.

The synthesis of ASU and ASN (5-azonia-spiro[4.4]nonane) are especially interesting compared to the other reactions due to an internal ring-closing (Figure 3.1). In principle, various side product are imaginable which do not occur in significant quantities though.

Using the synthesized and some other commercially available QAs it was possible to investigate the stability influence of external factors such as temperature, hydroxide concentration

and solvent, as well as the importance of the cation molecular structure.

Table 3.1: List of all synthesis reactions with respective amine, halocarbon, product QA, and yield.
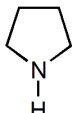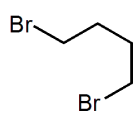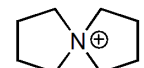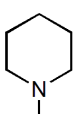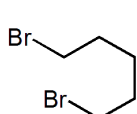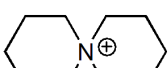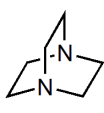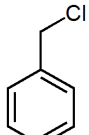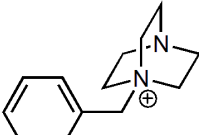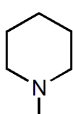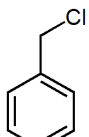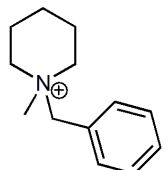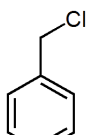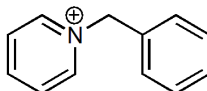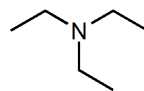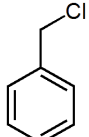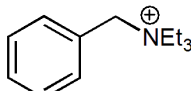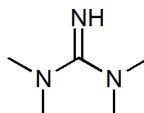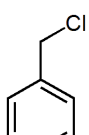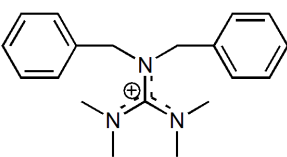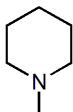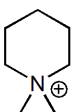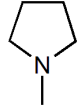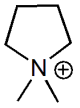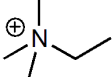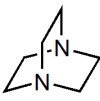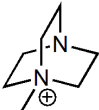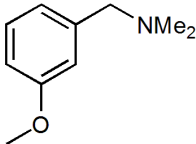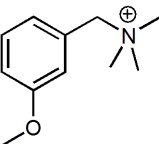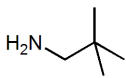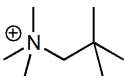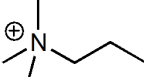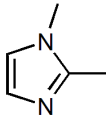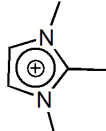
amine	halocarbon	QA product	QA name	yield (%)
			ASN	93
			ASU	77
			BAABCO	84
			BMP	60
			BP	21
			BTE	5
			DTG	<5
	H_3C-I		DMP	97

Table 3.1: List of all synthesis reactions with respective amine, halocarbon, product QA, and yield.

amine	halocarbon	QA product	QA name	yield (%)
	H₃C—I		DMPy	99
	Br⌐		ETM	91
	H₃C—I		MAABCO	78
	H₃C—I		MBTM	76
	H₃C—I		NTM	72
	Br⌐		PTM	100
	H₃C—I		TMI	33

3.1.2   Effect of temperature, hydroxide concentration, solvent, and anion

As it is with virtually any chemical reaction, temperature, solvent and reactant concentration have a significant effect on the rate of the hydroxide-induced decomposition of QA compounds and accordingly for AFC applications using HEMs.

The temperature dependency at constant hydroxide concentration follows an Arrhenius-type behavior and the activation energy of this process can be determined by plotting the effective rate constant k_1' (see Section 2.1.2) over the temperature (Figure 3.2). For BTM it is about 120 kJ/mol while it is higher for TMA, indicating that the benzylic group in BTM is more susceptible to nucleophilic attack, which will be discussed in more detail below.
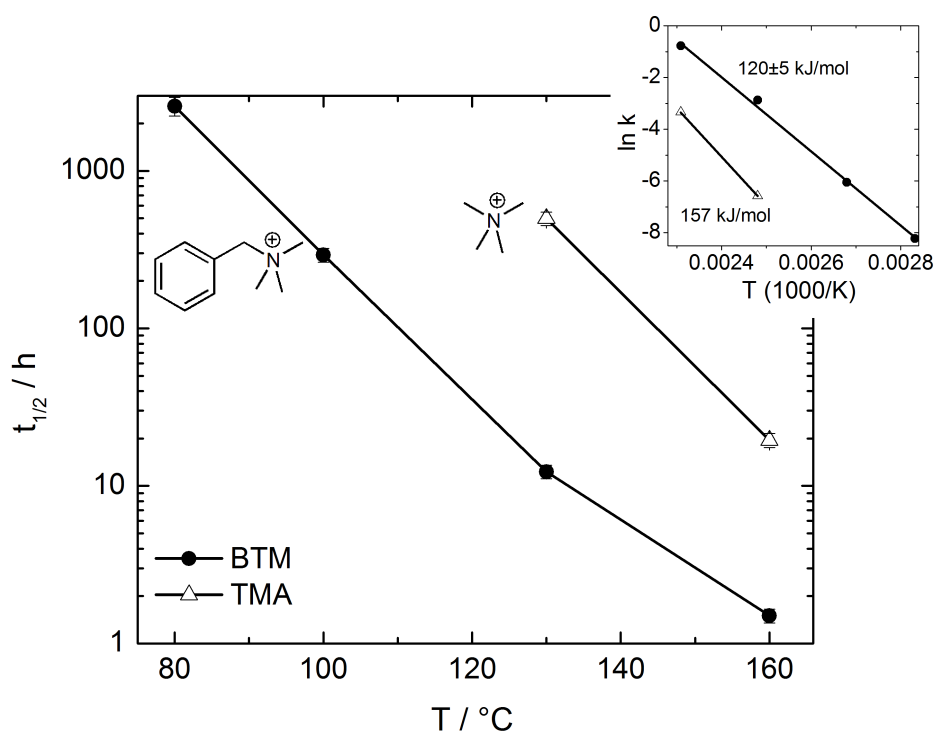
Figure 3.2: Temperature dependent half-life of benzyl-trimethylammonium (BTM) and tetramethylammonium (TMA) in aqueous 10 M NaOH solution. The insert shows the Arrhenius plot used to determine the activation energy of the overall degradation.

Apart from an increased degradation rate with increasing temperature, higher NaOH con-

centrations have a similar detrimental effect on the QA stability (Figure 3.3). In principle this can be explained by a shift of the equilibrium towards the products according to $NR_4^+ + OH^- \rightleftharpoons NR_3 + ROH$. It should be noted though that the amount of available water must not be neglected at such high hydroxide concentrations. For example, in a 6 M NaOH solution only about 10 water molecules per hydroxide group exist and they also have to solvate the sodium cation and the QA. The number of available water molecules per ion becomes smaller with increasing hydroxide concentration. This leads to smaller hydration shells that can not screen the charges effectively, which accelerates decomposition. Ultimately this leads to instant decomposition when one tries to isolate a pure solvent-free hydroxide form QA.[79]
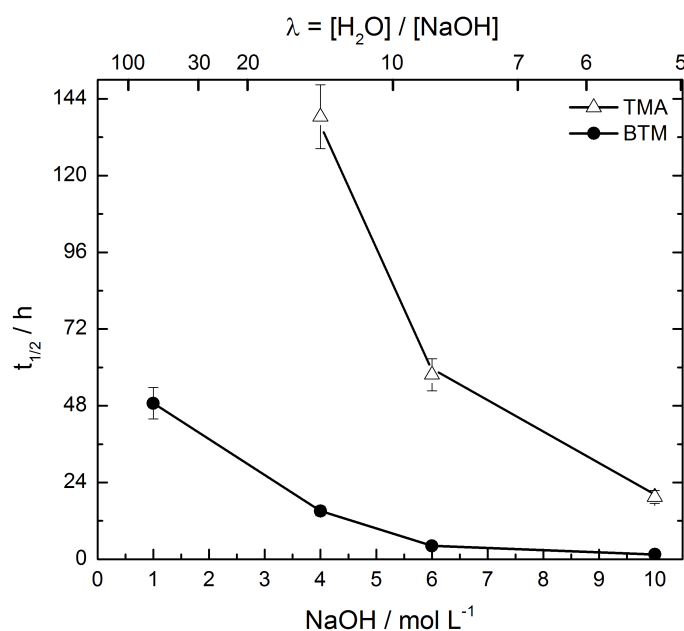
Figure 3.3: NaOH concentration dependent half-life of TMA and BTM at 160 °C. With increasing hydroxide concentration half-life decreases.

The substantial change of degradation rates with hydration provides an explanation for the current controversy regarding the alkaline stability of AEMs containing aromatic QAs, mentioned in the introduction. Membrane water uptake, and with it the degree of solvation, changes easily depending on temperature, relative humidity, IEC, crosslinking, and the nature of the backbone. This is even further complicated if NaOH solutions of varying concentrations are used as caustic environment for accelerated degradation. It is easy to imagine that a membrane containing a hypothetical QA_1, which on its own would be more

stable than a QA$_2$ at equal hydration, could actually found to be less stable due to the lower water uptake of its corresponding membrane.

Reduced solvation increases the rate constant of many chemical reactions which becomes not only apparent in highly concentrated solution but also by using solvents with inferior solvating properties for the reactants and transition states in question. The magnitude of this effect is shown in Figure 3.4 for the degradation of BTM in water, glycol and a 50:50 weight percent mixture of both. Varying the solvent changes the absolute reaction rates of different QAs and their relative stabilities as well, which stresses the importance of examining the base-stability of QAs in aqueous conditions, similar to those encountered in HEM AFCs to avoid fruitless conclusion.
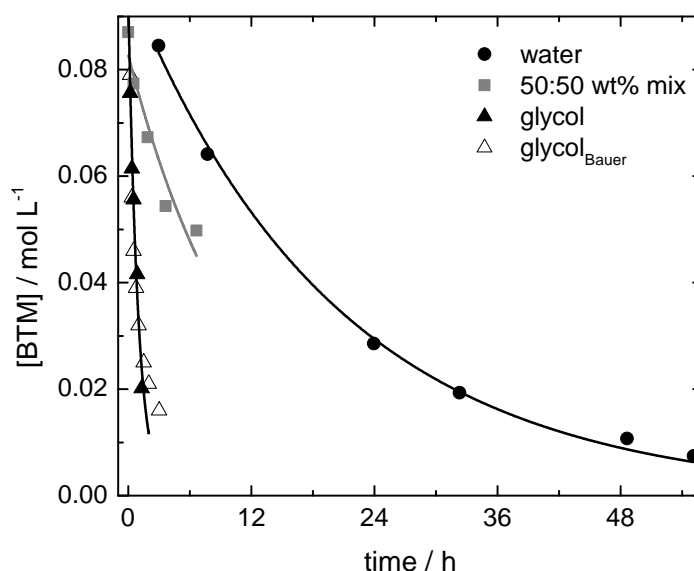
Figure 3.4: The degradation of BTM in water, glycol and a 50:50 wt% mixture of both solvents demonstrates the impact a change in the solvent can have on the absolute stability of a QA. The data is in line with the fact that the highly influential experiments by Bauer et al.[30] were conducted in glycol and not in water, as previously believed.

This has to be stressed at this point, since one of the most influential articles on AEMs actually compared the relative stabilities of a few QAs in alkaline solution, but reported highly different results from those in this thesis.[30] The reason was that their experiments were carried out in ethylene glycol instead of aqueous solution as expected, which was unfortunately not mentioned in the publication and only found out by perusing the diploma thesis where the work was first published (Figure 3.4).[61] Additonally, ethylene glycol causes

a number of further issues with this experiment which are described in more detail in Section 3.1.4.

To ensure that the experimental conditions in this work mimic those in a HEM sufficiently, aqueous NaOH concentrations of 6 mol/l (corresponding to a hydration number $\lambda = [H2O]/[QA] \approx 8.6$) were chosen for the general QA comparison experiments, which is comparable to reported hydration numbers of HEMs (λ = 6-15).[80–84] The degradation reactions were carried out at a relatively high temperature of 160 °C as otherwise the half-life of most QA species would have exceeded 100 h (see Figure 3.2). All decomposition experiments followed a pesudo-first order kinetic, allowing for simple calculation of the half-lives as outlined in Section 2.1.2.

The investigated QA salts in this thesis contain different counter anions (Cl^-, Br^- or I^-) because of commercial availability and preparation. In addition to differences in their structure this leads to differences in solubility, constraining the starting concentrations. To ensure that neither of these factors had a significant influence on the degradation rate, the half-life of the most simple QA TMA was determined in all three anion forms at different concentrations and fortunately found to be the same (Figure 3.5). Nonetheless, QA starting concentrations were limited for all experiments to 0.11 mol/l or below to minimize potential interaction between cations such as micelle formation or dimerization that could influence the degradation.

This section shows that HEMs for AFCs should always be highly hydrated, especially at elevated temperature to maximize their life time. The importance of the molecular structure of the ammonium group itself is investigated in the following section.

3.1.3 Influence of the molecular structure

The molecular structure is the factor that determines the relative alkaline stability of QA compounds at otherwise equal conditions. A considerable number of decomposition reactions exist that can neutralize the positive charge, and a change in the cation molecular structure that inhibits one reaction pathway often accelerates another one. This makes the prediction of relative stabilities of QAs with differing structures challenging for the most part, although results can generally be explained in retrospect.
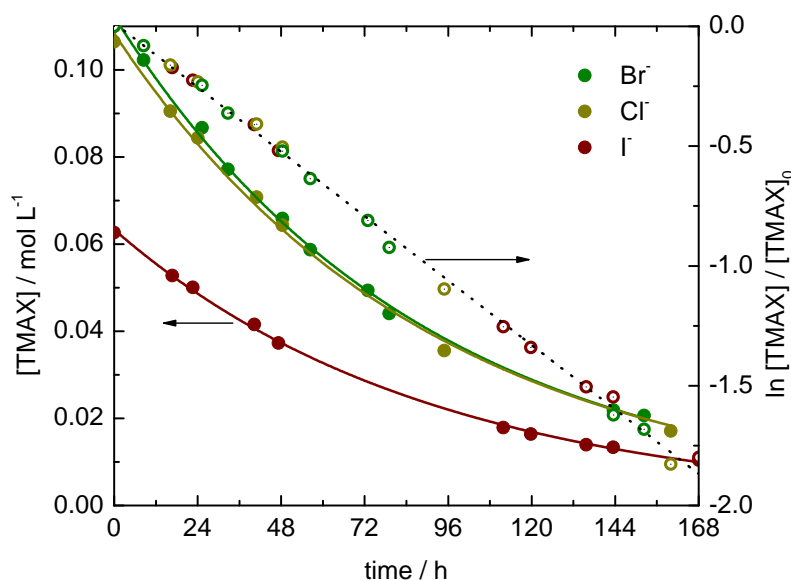
Figure 3.5: Decomposition of TMA in Cl^-, Br^- and I^- form at 160 °C in 6 M NaOH. The first order decay of $t_{1/2} = 62$ h is independent of anion and starting concentration.

Several molecule classes representing different attempts to maximize alkaline stability are outlined below. They are relevant for the design of the QA, its attachment to a polymer backbone and the molecular structure of the polymer. Tetramethylammonium (TMA) will be used as a benchmark throughout this work, since it is the QA with the simplest structure and also comparatively stable with a half-life of 62 h at 160 °C in 6 M NaOH.

Benzylic groups

The benzylic group is of particular importance to AEM development as it is currently the standard tether by which QAs are attached to the polymeric backbone. This is mostly because it is simple to functionalize poly(sulfone)s (e.g. Udel, Radel) with this group, giving fast access to a wide variety of IECs for membrane characterization.[82] The benzyl tether can be mimicked to some extent by the benzyltrimethylammonium (BTM) group. It does not contain any β-protons but an aromatic π-system and allows investigation of the influence of some types of polymer links, since the aromatic ring can be modified with electron donating or withdrawing groups (Figure 3.6).

Figure 3.6: A benzyl group with various polymer linking groups (X) typically encountered in HEMs can be mimicked to some extend by comparable substitutents (Y) on a BTM cation.

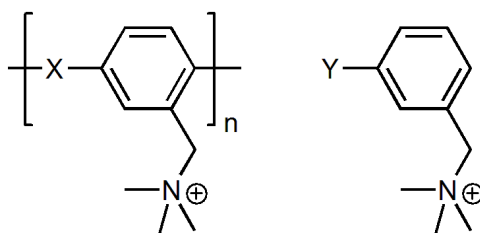AEMs based on such polymers are also convenient from another fundamental standpoint since cation exchange membranes with sulfonic acid groups are often based on the same backbones, which allows direct comparison of polymers with opposite charges. While poly(sulfone)s with sulfonic acid functional groups are comparatively stable in acidic conditions, the same is not the case for their HEM counterpart in alkaline environment unfortunately.

An issue with the benzyl tether is that the aromatic ring has a small but noticeable -I effect, i.e. it is electron-withdrawing. A reduced electron density at the QA increases its electrophilic character, thus making it more susceptible to an attack by the nucleophilic hydroxide. Additionally, the π-system of the benzyl group makes radical formation more facile (Figure 3.7). Since radicals are constantly produced in an active FC this may be an additional cause for membrane failure.
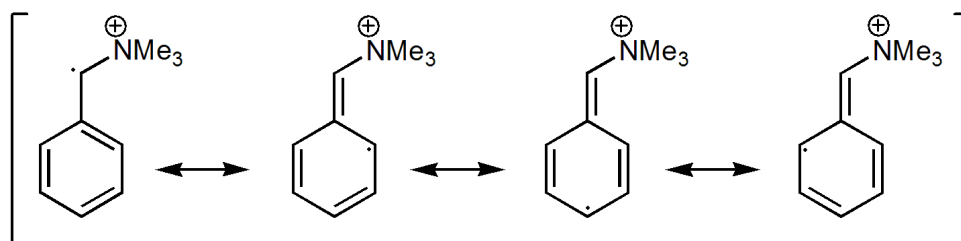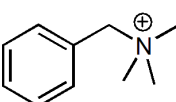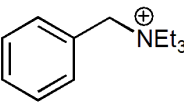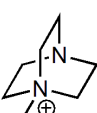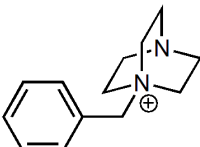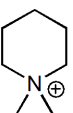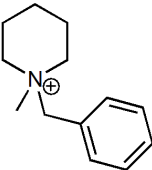
Figure 3.7: Delocalization in a BTM molecule benefits radical formation and may cause degradation in an active FC.

When the half-life of BTM is compared to that of TMA at 160 °C in 6 M NaOH it is found to be 14 times shorter (Table 3.2). It is obvious that the benzylic group represents a structural weak point at which hydroxide can attack to form benzyl alcohol and trimethylamine in spite of the bulky aromatic ring, which should inhibit hydroxide approach to some extent.

In comparison, substitution at the methyl groups is very slow even though the benzyl to methyl ratio is 3:1.

Table 3.2: Half-life of QA compounds in 6 M NaOH at 160 °C. Introducing a benzyl group always reduces the half-life of a given aliphatic ammonium ion by about an order of magnitude. Ethyl may be the only more reactive aliphatic group.

QA	short	half life (h)
	TMA	62
	BTM	4.2
	BTE	0.7
	MAABCO	13.5
	BAABCO	1.4
	DMP	87.3
	BMP	7.3
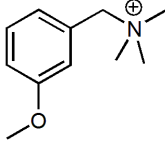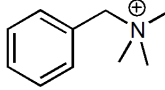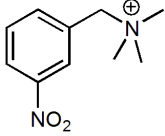
Interestingly, the benzyl appears to negatively impact the alkaline stability of structurally very different aliphatic QA compounds to about the same extent. Independent of the other ammonium residues half-life decreases by about an order of magnitude with the

introduction of a benzyl group (Table 3.2). The only exception to this are ethyl groups, in which β-elimination proceeds even faster than substitution at the benzyl group.

While this makes benzyl groups appear to be a suboptimal choice as structural component in HEMs, their detrimental effect can be influenced by modification of the aromatic ring with electron-withdrawing (-I) or donating (+I) residues. A methoxy group (+I) in meta position for example increases half-life from 4.2 to 16 h, while a nitro group (-I) further withdraws electron density from the QA, reducing half-life to only 0.7 h (Table 3.3). These large differences emphasis the importance of the chemical structure of the polymers and molecules of which the QA is not directly a part of.

For HEMs it follows that benzylic groups should best be avoided in favor of more suitable compounds or at least be attached to a polymer that contains electron-inducing groups. Even in non-benzylic structures, components with a +I effect are likely beneficial. Electron withdrawing groups such as $-SO_2-$ are expected to exacerbate degradation on the other hand.

Table 3.3: Half-life of QA compounds in 6 M NaOH at 160 °C with electron withdrawing (NBTM) and electron donating (MBTM) residue compared to a neutral BTM.

QA	short	half life (h)
	MBTM	16.6
	BTM	4.2
	NBTM	0.7

Aromatic cations

Aromatic cations have received a great deal of attention following the work by Yan et al,[48,85] in which imidazolium based HEMs were reported to exhibit high alkaline stability. Subsequent studies partially supported and opposed these findings (see Section 2.1.4) resulting in considerable confusion in the AEM community. These conflicting results may partially be caused by insufficiently controlled hydration states of the membranes or interactions with the polymer backbone. To conclude whether aromatic QAs are suitable functional groups, comparing their stability to simple aliphatic molecules will definitely be helpful.

In the available literature, monomeric imidazolium based QAs are generally found to be unstable in the presence of bases, even at relatively mild conditions.[86] Similarly, methylated polybenzimidazole is known to decompose rapidly in KOH[63] and decomposition rates of phenyl or anilinium based QAs were found to be orders of magnitude faster than comparable saturated QAs.[87,88]

Still, the relationship between alkaline stability and molecular structure is complex, which has recently been demonstrated for imidazolium type cations. It was suggested that in addition to steric and electronic factors, competing deprotonation reactions dominate their alkaline stability (Figure 3.8).[60]
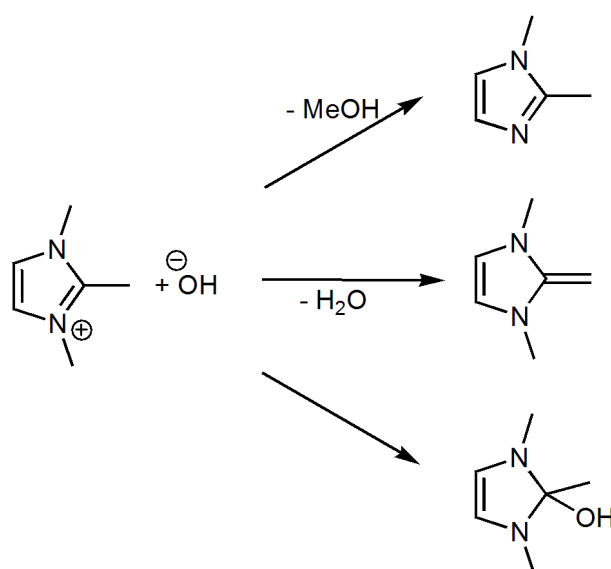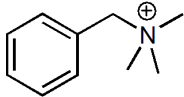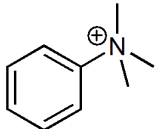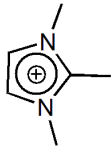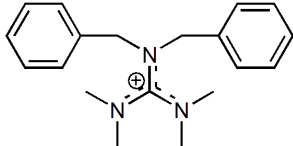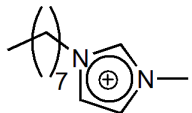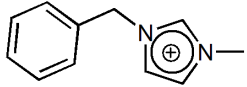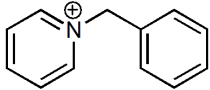
Figure 3.8: Degradation pathways for 1,2,3-trimethylimidazolium.[60]

This led to counter-intuitive results, e.g. a higher stability of 1,2,3-trimethylimidazolium (TMI) compared to the more sterically shielded 2-benzyl-1,3-dimethylimidazolium and 2-*tert*-butyl-1,3-dimethylimidazolium. Nevertheless, even the most stable imidazolium compound TMI was reported to have a measurably lower half-life than an aliphatic neopentyl based QA.[60] Another work that investigated guanidinium based QA showed that dibenzyl-tetramethylguanidinium is stable at mild alkaline conditions of 60 °C in 1 M NaOH for 50 h but its mono-benzylated counterpart decomposed rapidly at the same conditions.[89]

All this indicates a low potential for the utilization of aromatic QAs in HEMs and indeed, all such compounds that were investigated in this work decomposed almost instantly at 160 °C in 6 M NaOH (Table 3.4). Some aromatic QAs were instantly destroyed during addition of the caustic solution at room temperature, making half-life determination impossible. Even TMI had an insignificantly short half-life compared to TMA or BTM.

From this data it is obvious that delocalization alone can definitely not stabilize the positive charge. If no precautions are taken to create additional steric shielding or increase electron density, aromatic groups should be avoided in favor of simpler aliphatic QAs. Even if the above precautions are taken it remains questionable whether aromatic QA stability will be adequate.

Table 3.4: Half-lifes of BTM and various aromatic QA compounds at different temperatures in 6 M NaOH.

QA	short	half life (h)	T (°C)
	BTM	4.4	160
	PhTM	0.13	160
	TMI	too short to measure	160
	DTG	too short to measure	160
	MOI	too short to measure	60
	BMI	too short to measure	25
	BP	instant decomposition	25

Spacer-chains

The way in which a QA is attached to the polymer backbone can have a large influence on its alkaline stability. Benzylic groups for example are highly reactive next to a QA as shown above and removing them by inserting a spacer-chain between benzyl and QA is expected to result in more base resistant substances. Indeed, introducing such a "spacer-chain" (similar to the side-chain structure of Nafion) has been shown to increase the hydroxide stability of the corresponding membranes. [49,64] Interestingly though, even attaching a chain to a benzyl tethered QA seems to be beneficial (Figure 3.9) which can not be explained by the same rationale.
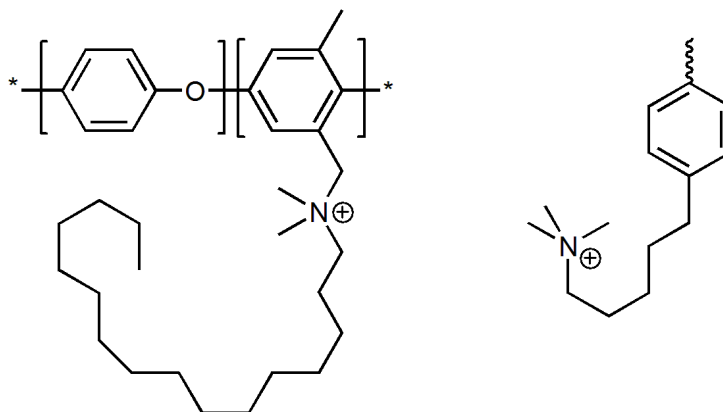
Figure 3.9: Structures of AEM polymers containing alkyl-chains that were shown to improve alkaline stability when compared to a chain-length of only one CH_2 group. [49,65]

When the influence of the side chain length on the stability of QA salts is investigated, no simple relationship between half-life and the number of carbon atoms in the chain can be observed (Figure 3.10).

TMA with the shortest possible methyl chain is by far the most stable of those compounds, indicating that substitution at the methyl groups is the slowest degradation pathway, since it is the only available mechanism for TMA. With longer chains, elimination at the β-protons occurs at a much higher rate and dominates the degradation. Increasing the chain length by an additional carbon to create an ethyl group dramatically decreases the half-life by a factor of >20 upon which stability increases again with further elongation.

The elimination proceeds most readily with an ethyl group because a) the β-protons exhibit no steric shielding, b) the acidity of the protons is higher, as no +I effect from a longer
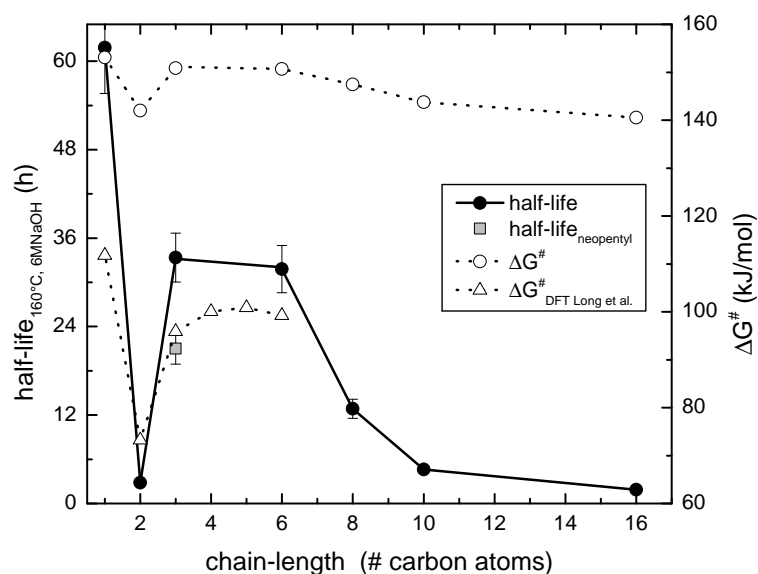
Figure 3.10: Half-life of alkyltrimethylammonium functional groups containing one alkyl chain of varying length in 6 M NaOH at 160 °C. Corresponding reaction free energy barrier $\Delta G^{\#}$ data was calculated by using the Eyring equation. DFT data by Long et al. follows the same qualitative trend but absolute values differ by about 50 kJ/mol.

alkyl residue is present and c) there are 3 freely rotating protons available, compared to only 2 somewhat inhibited ones in longer chains.

This explains why half-life increases from ethyl to propyl group and since the chain orients itself or "grows" away from the positive charge,[46,90] any additional steric or inductive effect diminishes with further CH_2-groups, resulting in a stability plateau or maximum, at least at the chosen conditions. Earlier experimental works reported similar results, finding that, while elimination rate decreases with chain-length up to around 4 carbon atoms, substitution at the methyl groups remains unaffected.[59,91–93]

Surprisingly, the alkaline stability then decreases again with even longer chains. While the trend up to hexyl can be rationalized in relatively simple terms, the renewed decrease of the half-life above hexyl is more difficult to explain. More than steric or inductive factors have to be involved. Potentially, a similar reason causes QAs in membranes to decompose much faster than their simple salt counterparts, as was observed in the past.[54,60,94]

It is imaginable that the elimination products of longer chains are removed more quickly

from the reaction equilibrium due to an increased tendency for phase separation with the aqueous solution (Figure 3.11). A potential back-reaction which can occur in the presence of a strong base[95,96] may thus be inhibited or the long hydrocarbon chain might disrupt the solvent shell, reducing the effective solvation number and increasing the reaction rate.
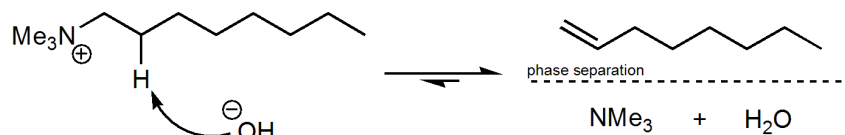
Figure 3.11: Elimination reaction of alkyltrimethylammonium potentially results in a fast phase separation of organic products and aqueous phase, inhibiting a potential back-reaction.

Another factor that increases parallel to the chain length is micelle formation. Micelles are known to influence the rate of chemical reactions[97] and can also lead to decreased dissociation.[98–101] Critical micelle formation concentration (CMC) decreases with the addition of other salts but increases by more than an order of magnitude between 25 and 160 °C.[100,101] Alkyltrimethylammonium hydroxides exhibit relatively high CMCs and a lower aggregation number compared to halides,[98,99] so the extent of micelle formation at the relevant experimental conditions is difficult to assess without further experiments.

Independent of why exactly the stability maximum exists, an optimal chain length between 3 to 6 carbon atoms is discernible, which also seems to appear in the free energy barriers $\Delta G^{\#}$ calculated by Long et al. for elimination and substitution reaction of hydroxide with alkyltrimethylammonium groups. Unfortunately, the calculation only went up to hexyl chain length and micelle formation was not regarded.[59]

A comparison of the data by Long et al. with the present experimental results is possible as $\Delta G^{\#}$ can be calculated from the degradation rate constants using the Eyring-Polanyi equation for solutions:[102,103]
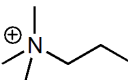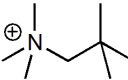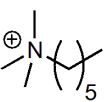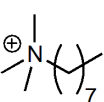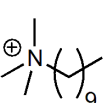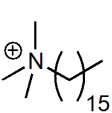
$$k = \kappa \frac{k_B T}{h} e^{-\frac{\Delta G^{\#}}{RT}}$$

in which k is the reaction rate constant, κ the transmission coefficient (assumed to equal 1), k_B the Boltzmann constant, T the temperature in kelvin, h the Planck constant and R the ideal gas constant. The data follow the same relative trend, with absolute values differing by about 50 kJ/mol (10 kcal/mol).

The present data together with previous results strongly suggest that β-elimination is the primary degradation pathway in side-chain containing QAs, which is slowed down to some

extent by the steric and electron inducing properties of the chain itself. Consequently, removing the β-protons could potentially lead to higher alkaline stability since the elimination pathway would not be available anymore.

Table 3.5: Half-life of alkyltrimethylammonium cations with varying side-chain length and a neopentyl based QA at 160 °C in 6 M NaOH, ordered with respect to main chain length.

QA	short	half-life (h)
	TMA	62
	ETM	2.8
	PTM	33.4
	NTM	20.9
	HTM	31.8
	OTM	12.9
	DTM	4.6
	HexDTM	1.9

This prediction was tested experimentally with a neopentyltrimethylammonium (NTM) cation containing no β-protons. NTM was found to have a far lower half-life than its propyl based analogue PTM with an equally long main chain (Figure 3.10, Table 3.5). This means another degradation mechanism (probably a rearrangement) occurs at a faster rate in NTM than elimination in PTM.

As such, no trivial relationship between molecular structure and alkaline stability can be observed, even for structurally simple alkyltrimethylammonium cations. Relative stabilities of QAs are difficult to predict in advance, though all results are expected to be easily explainable in retrospect given sufficient experimental data. This unpredictability was reason enough to investigate structurally very different QAs: aliphatic heterocycles.

Aliphatic heterocycles

Aliphatic heterocycles have been treated rather stepmotherly by the AEM community. One reason for this is likely the feared β-elimination, which occurs in the presence of β-protons that the simple heterocycles possess. In N,N-dimethylpiperidinium (DMP) for example these β-protons even prefer an anti-periplanar position and are therefore expected to be highly susceptible to elimination. The same is not the case for N,N-dimethylpyrrolidinium (DMPy) but its ring-strain potentially accelerates ring cleavage (Figure 3.12). Hence the only at least marginally investigated QA heterocycles are based on 1,4-diazabicyclo[2.2.2]octane (DABCO).[30,62]
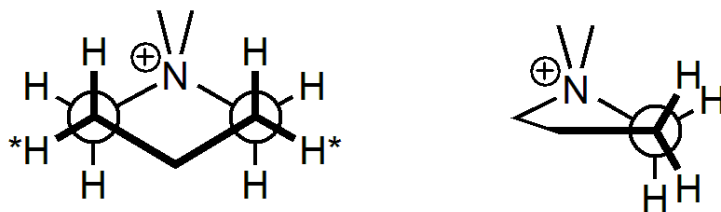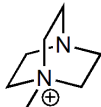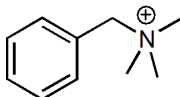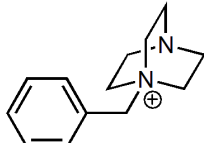
Figure 3.12: Newman projection of N,N-dimethylpiperidinium (DMP) and N,N-dimethylpyrrolidinium (DMPy). The β-protons in anti-periplanar position are marked by asterisks.

In the DABCO molecule the β-protons are rotationally restricted by its cake-like molecular structure, thereby avoiding the anti-periplanar position in respect to the nitrogen, which reduces propensity for elimination (see Section 2.1.4).[30,45–47] The β-elimination should not be considered alone though, as competing reactions and the chemical environment (e.g. steric, base-strength, temperature) influence the dominating degradation pathway. A benzylated version of the DABCO molecule 1-benzyl-4-aza-1-azonium-bicyclo[2.2.2]octane (BAABCO) was actually reported to be the most stable of several QAs by Bauer et al. but only a very limited number of cations were investigated in ethylene glycol with uncertain accuracy (see Section 3.1.4).[30,61]

Contrary to the results by Bauer the measurements in this work show that DABCO-based QAs are considerably less stable than their non cage-like counterparts (Table 3.6). Apparently, rotational inhibition of the β-protons is more than compensated by other reactivity enhancing effects in this type of molecule. The destabilizing effect of the DABCO group is probably the result of two factors. One is the second nitrogen close to the positive charge that exhibits an electron withdrawing effect,[64,104] and two is the ring-strain inherent in this bicyclic compound (compare bicyclo[2.2.2]octane).[105,106]

Table 3.6: Half-life comparison of DABCO-based cations with non-cage-like analogs at 160 °C in 6 M NaOH.

QA	short	half-life (h)
	TMA	61.8
	MAABCO	13.6
	BTM	4.4
	BAABCO	1.4

Utilizing the advantages of the rotational inhibition in DABCO while eliminating the drawback of the second nitrogen might prove beneficial and is in principle possible with the quinuclidine molecule (Figure 3.13), but its synthesis is difficult and the compound expensive. Simpler and more cost effective alternative substances that fulfill the above criteria are therefore required, namely QAs based on piperidine and pyrrolidine heterocycles.

Figure 3.13: A methylated quinuclidine cation.

Just like DABCO, the DMP and DMPyr cations contain β-protons which are somewhat rotationally inhibited along the C-C bond by the ring geometry. The 5-membered ring

structure of DMPyr was expected to stabilize the QA at least to some extent and indeed, a high half-life of 37.7 h was found, which is higher than for all other compounds that were investigated up to this point, with the exception of TMA.

More surprisingly, the 6-membered ring compound DMP surpassed not only the half-life of DMPy but also that of TMA by more than 40 %. This means that while the pyrrolidinium ring is more susceptible to degradation by hydroxide than the methyl groups, the opposite is true for piperidinium. Replacing the residual methyl groups of DMP with another heterocycle should consequently lead to a molecule of even higher alkaline stability. Therefore the molecule ASU was synthesized and found to be the most stable compound of all investigated cations with a half-life of 110 h. The pyrrolidinium based spiro compound on the other hand was less stable than DMPy, supporting the conclusion that degradation at the 5-ring is faster than at the methyl groups (Table 3.7).

While the relatively high stability of DMPy can to some degree be explained by the non-anti-periplanar position of the β-protons, the reason for the extremely high DMP stability is less obvious. To find out why this is the case, the possible degradation pathways of DMP and DMPy were examined in more detail. Three reactions are expected to occur in the presence of hydroxide, which are **a**) nucleophilic substitution at the methyl groups, **b**) ring-opening elimination and **c**) ring-opening substitution (Figure 3.14).
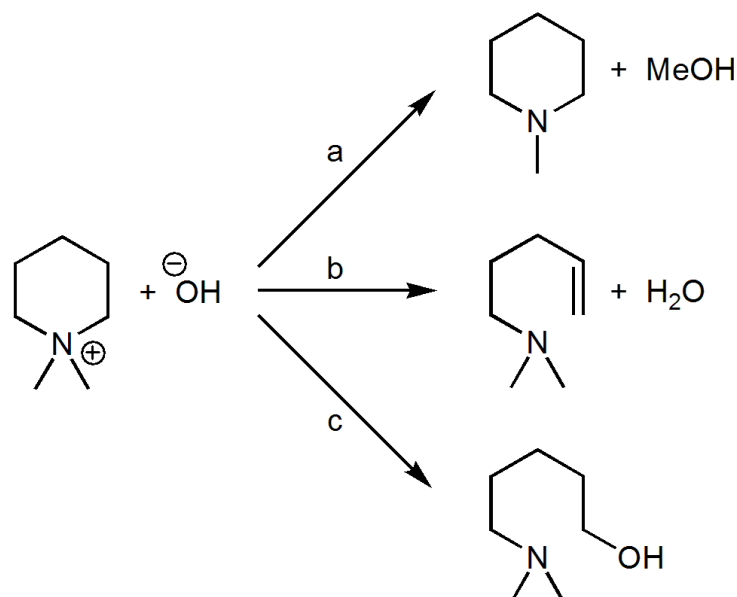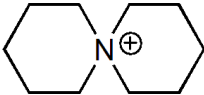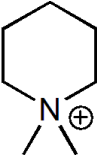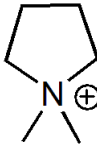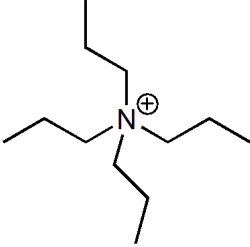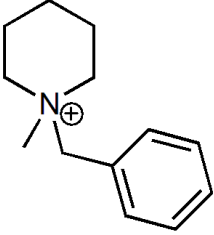
Figure 3.14: The three possible degradation pathways for a DMP cation. **a**) nucleophilic substitution at the methyl group, **b**) ring-opening elimination and **c**) ring-opening substitution.

Table 3.7: Half-life of cyclic QA groups and TPA, the open-chain analogue to ASU, at 160 °C in 6 M NaOH.

QA	short	half-life (h)
	ASU	110
	DMP	88.6
	DMPy	37.7
	TPA	7.8
	BMP	7.4

From the relative half-lives alone it can be deduced that methyl substitution is the dominating decomposition pathway for DMP. This is also discernible through ^{1}H-NMR analysis that shows a strong reduction in the intensity of the methyl group signal after degradation, while other protons remain almost unaffected (Figure 3.15). Interestingly, the integral of the methyl group becomes so small as to suggest removal of both methyl groups to a significant degree. A slight reduction of the signal at three ppm and no additional emerging peaks in the the high ppm region suggest a small amount of ring-opening substitution. The effective reaction rates for DMP are therefore suspected to be $k'_a > k'_c > k'_b$. The spiro compound then likely degrades primarily via ring-opening substitution since no methyl groups are available. This may explain why only the α-proton signal loses intensity in the ^{1}H-NMR spectrum while no high ppm signals emerge (Figure 3.16).
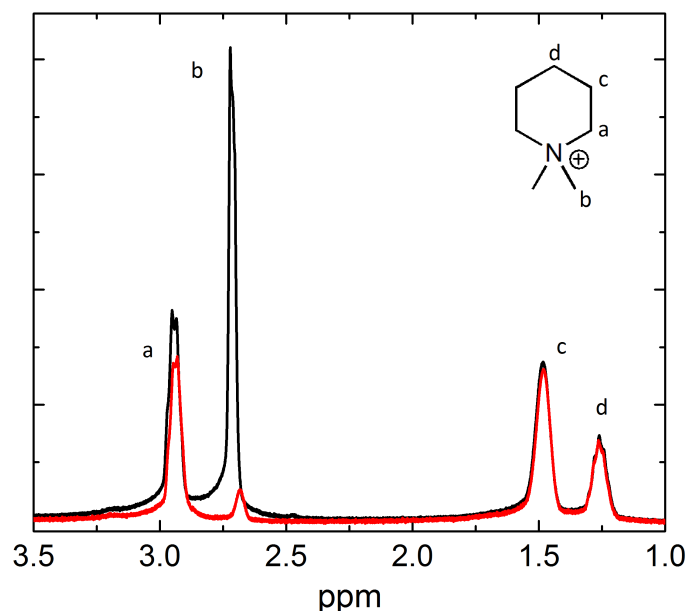
Figure 3.15: ^{1}H-NMR spectra of pristine (black) and in 6 M NaOH at 160 °C degraded (red) DMP. The primary degradation pathway of nucleophilic substitution at the methyl groups causes the **b** signal to lose intensity.

For the 5-membered compounds decomposition is faster and the ^{1}H-NMR spectra harder to interpret. During decomposition of DMPy and ASN furrowed signals emerge suggestive of double bonds but at comparatively low ppm values, while the surfacing signals around 1 ppm conform to what is expected of an open chain product.[107,108] The samples probably contained a mixture of elimination and substitution products together with methanol and butadiene which is why the primary degradation pathway could not be determined from
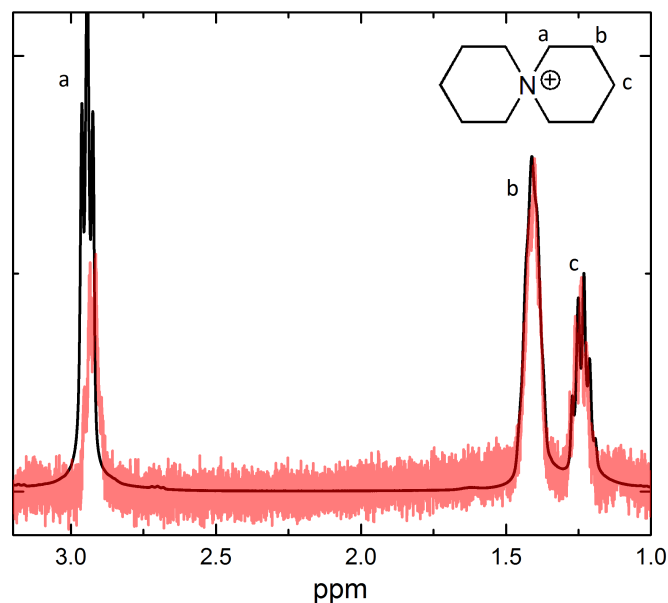
Figure 3.16: ^{1}H NMR spectra of ASU fresh (black) and after 120 h of degradation in ≈ 6 M NaOD at 160 °C. Since no high ppm signals appear and **a** loses intensity ring-opening substitution is probably the main degradation pathway.

^{1}H-NMR (Figure 3.17). It should be noted that the high concentration of NaOD or NaOH in the D_2O solutions moves all signals to lower shifts by at least 0.8 ppm compared to a pure D_2O solution, complicating the interpretation of the spectra.

In a previous work from 1980 where the degradation of heterocyclic ammonium compounds was investigated in a methanolic solution with a concentration of 0.1 M methoxide ions, it was reported that the rate of ring-opening substitution correlates with ring strain while ring-opening elimination rate correlates with ring size.[87,109,110] Consequently substitution dominated for DMPy and elimination for DMP,[87,109,110] but the different solvent may be responsible for the conflicting result for DMP.

Separate from the question which degradation pathway dominates, the reactivity of especially the 6-ring is significantly lower than that of any other aliphatic or aromatic compound. The reason for this high resistance against hydroxide induced degradation is not apparent from the molecular structure at first glance and requires a look at the relevant reaction transition states. Since the transition states resemble both starting materials and products, in the case of the ring-opening elimination in DMP or ASU both a 90° and a 120° angle inside the 6-ring is required (Figure 3.18), because the carbon atoms at the emerg-
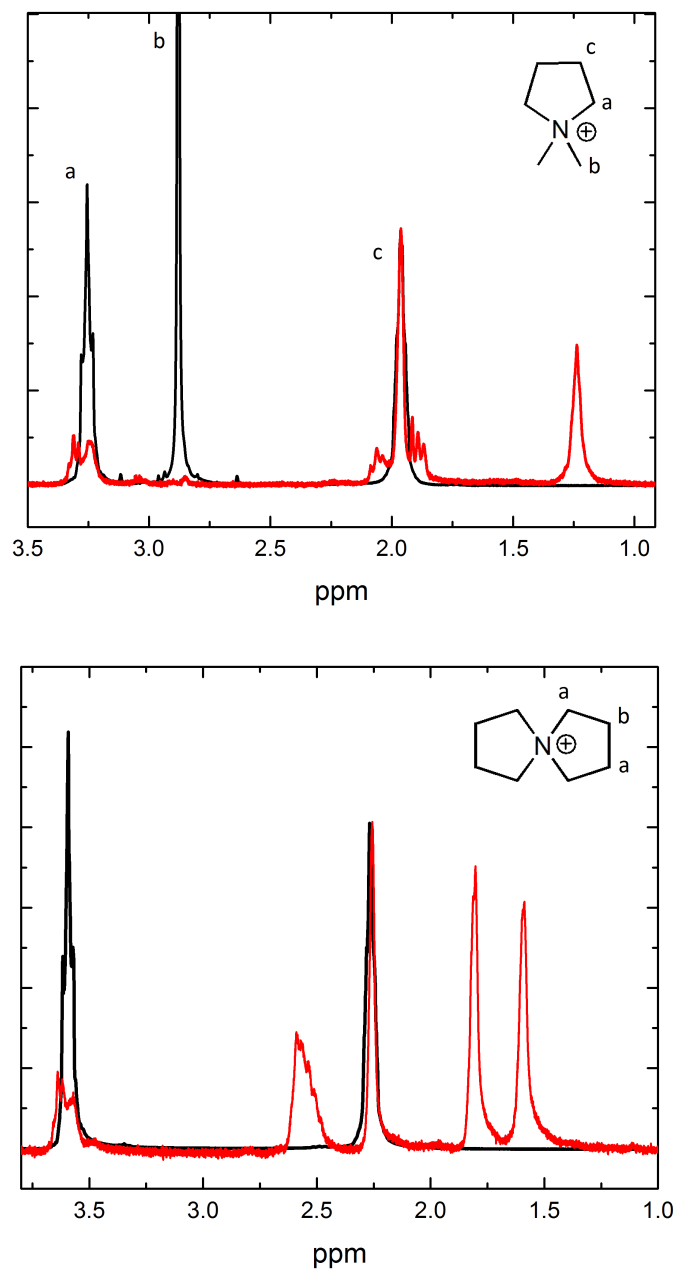
Figure 3.17: ^{1}H-NMR spectra of ASN and DMPy fresh (black) and after degradation (red) in $\approx$ 6 M NaOD at 160 °C.

ing double bond take on a trigonal-pyramidal geometry as a result of the hybridization transition from sp^3 to sp^2. This causes considerable distortion of bond angles and lengths in the heterocycle, raising the activation energy of the reaction process. The distortion is difficult to highlight in any type of chemical projection and most easily visualized and felt using a molecular construction kit.

ring-opening elimination
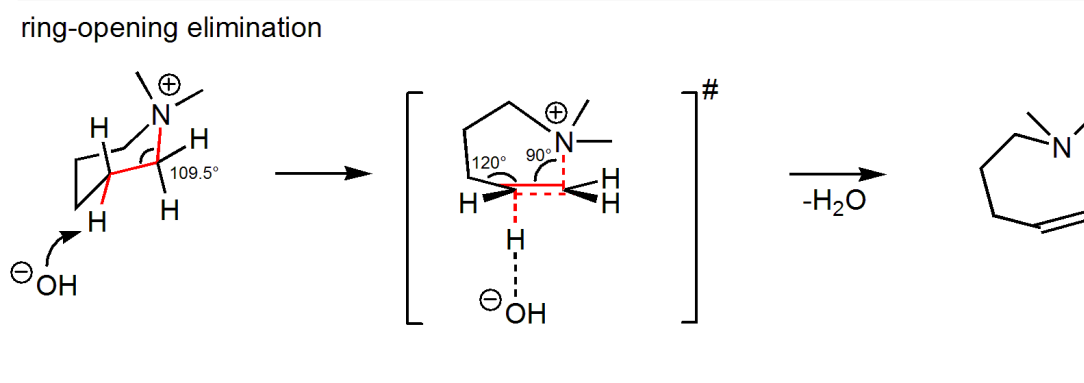
Figure 3.18: Ring-opening β-elimination in a DMP cation requires unfavorable bond angles and lengths.

The heterocycle similarly affects ring-opening substitution, as it preferably proceeds through a trigonal-bipyramidal transition state with 120° and 90° angles in which the distance between the substituents is maximized. While these angles are easily attained in the methyl substitution, the ring-opening reaction again requires either the distortion of the 109.5° sp^3 tetrahedral bond angles and lengths of the ring, or those of the transition state itself (Figure 3.19). Distortion is also required for the reactions in the 5-membered QAs, but their ring-strain seems to decrease the necessary energy to reach the transition state sufficiently to negate the advantages of their constrained geometry. While other attempts to stabilize the quaternary ammonium tend to focus on the removal or steric protection of vulnerable groups (e.g. β-protons), the heterocyclic approach severely decreases their reactivity through an increase of the reaction activation energy in a comparatively simple way.

Of course the above reasoning is speculative for the moment and requires a simulation approach to confirm or disprove. Still, independent of the fundamental reasons it is definitely something about the ring itself that gives it superior alkaline stability. Apart from the above results and those from Section 3.1.3, the fact that tetrapropylammonium (TPA),
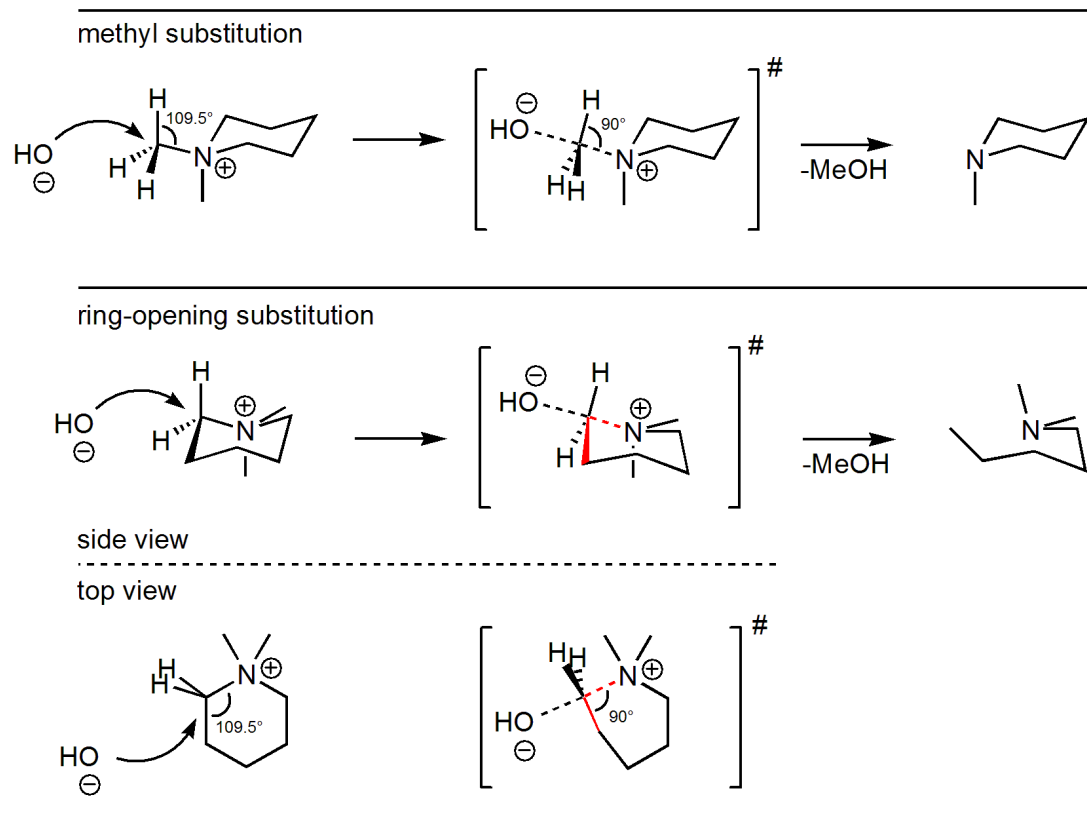
Figure 3.19: Nucleophilic substitution in the DMP cation. The trigonal bipyramidal transition state prefers in-plane and out-of-plane angles of 120° and 90° respectively. In the ring-opening substitution, these angles can only be attained through distortion of the 6-ring.

the open-chain analog of ASU, exhibits a comparatively low half-life of 7.8 h (Table 3.7) supports this conclusion.

The stability of piperidinium heterocycles might further be improved through attachment of residues at appropriate positions in the ring. Positions 3, 4 and 5 for example are interesting for further residues as they would likely increase the strain on the transition states. Residues at 2 and 6 are bound to decrease stability though, since an alkyl side chain that contains freely rotating β-protons that do not suffer from the geometric constraint of the ring are created, promoting ring-opening elimination[110] (Figure 3.20).
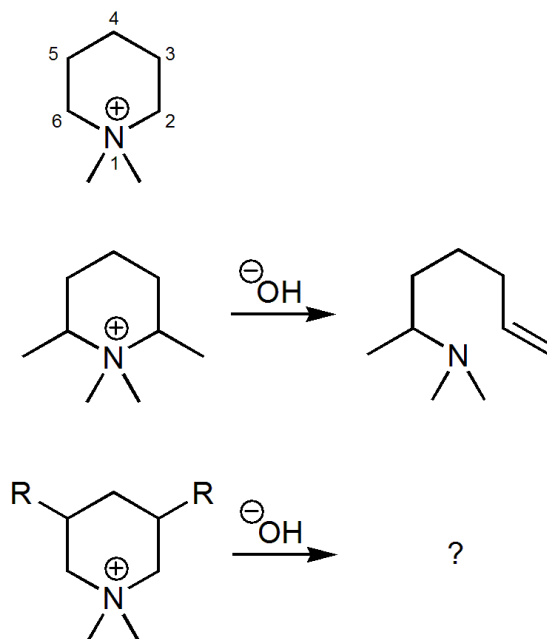
Figure 3.20: Stability of piperidinium based QAs can probably be further enhanced via substituents at the 3, 4 or 5 position. Residues at 2 and 6 cause rapid elimination[110] on the other hand, as this creates side-chain-like β-protons.

3.1.4   Glycol as solvent

The stability investigation in this thesis was inspired by the now 24 year old work of Bauer et al.[30,61] and the recent focus on imidazolium based compounds in the AEM community. After several attempts to reproduce the results by Bauer failed, a more detailed experimental description was sought and fortunately found in the diploma thesis of Bauer. This led to the discovery that all his stability experiments were conducted in ethylene glycol (EG).

The reason for this was likely the high rate at which the caustic solutions corrode glass at high temperatures, creating large amounts of abrasion consisting of very fine particles that are virtually impossible to remove. These steadily increase the viscosity of the solution, making stirring and reproducible sample-taking very difficult. This makes working with prolonged degradation times basically impossible, which therefore had to be reduced by the usage of EG (see Section 3.1.2). EG unfortunately disrupts the experiment by rapid decomposition in the presence of hydroxide, resulting in a dark brown viscous solution that interferes with the UV/Vis measurements used to determine QA concentration.

By using Teflon coated glass cylinders and aqueous alkaline solutions, both particle and glycol issues could be eliminated and the scatter compared to Bauer's data significantly reduced. The improved aqueous experimental conditions showed that QA stabilities were dramatically underestimated through the use of EG. Additionally, information on QA relative stabilities could be ameliorated since the comparatively small difference found by Bauer between e.g. the half-life of BTM- and BAABCO in glycol at 160 °C (31 and 44 minutes respectively) was insufficient to determine which of them is more stable. So while the work of Bauer certainly deserves attention as a first study, the absolute and relative values that were reported should be treated with caution.

3.2   Ion and water transport in anion exchange membranes

3.2.1   General aspects

The mobility of ions and the diffusion of water in AEMs are dependent on a number of factors such as the kind of anion, ion exchange capacity (IEC), temperature, and water content. Before going into the details about the transport inside of a membrane it is therefore useful to consider the transport of the relevant species in aqueous solution.

For solvated ions in water, mobility can be expressed as molar conductivity Λ or as the conductivity diffusion coefficient D_σ, which represents the mobility of individual ions. These parameters are correlated through the Nernst-Einstein equation

$$D_\sigma = \frac{\Lambda \cdot R \cdot T}{z^2 \cdot F^2}$$

in which R is the ideal gas constant, T the temperature, z the charge number of the ion and F the Faraday constant. Measuring both D_σ and the tracer diffusion coefficient D allows comparison of the transport of charged and neutral species (here: ions and water).

	Λ^∞ (S mol^{-1}cm^2)	D^∞ (10^{-5}cm^2 s^{-1})
H^+	349.7	9.3
OH^-	198.0	5.3
HCO_3^-	44.5	1.2
CO_3^{2-}	59.3	0.9
F^-	55.4	1.5
Cl^-	76.31	2.0
Br^-	78.1	2.1
I^-	76.8	2.1
H_2O	-	2.3

Table 3.8: Equivalent conductivities Λ^∞ and diffusion coefficients D^∞ of ions and water in infinitely diluted aqueous solution.[111] The relationship between equivalent conductivity and diffusion coefficient is $\Lambda^\infty = D^\infty \cdot 37.55$ (for the units given in the table).

Molar conductivity and especially diffusion coefficients of the ions vary only inside a small range and, expressed as D_σ, are close to water (Table 3.8). The differences are governed by

the hydrodynamic radius R_H of the species in question, comprised of its own radius and its hydration shell. This is because ions do not move through the water isolatedly but with a noticeable hydration shell (Figure 3.21). Small and hard ions (HSAB concept) generally show a lower diffusion coefficient since they exhibit a more stable hydration shell resulting in a larger R_H (compare F$^-$ with other halides).[112] The correlation of diffusion coefficient and hydrodynamic radius is described by the Stokes-Einstein equation in which k_B is the Boltzmann constant and η the viscosity of the medium.

$$D = \frac{k_B \cdot T}{6 \cdot \pi \cdot \eta \cdot R_H}$$
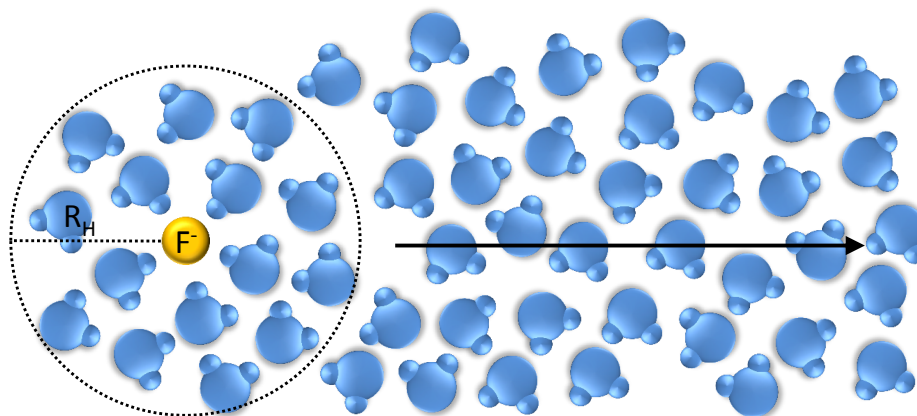
Figure 3.21: Fluoride drags a considerable hydration shell along during diffusion. The large hydrodynamic radius results in a lower diffusion coefficient compared to the other, less strongly coordinated halide ions.[112]

Exceptions to this behavior are observed for hydronium (H$_3$O$^+$) and hydroxide (OH$^-$). Since these ions are small and hard they would be expected to have a comparatively large hydrodynamic radius, but despite that, their conductivity diffusion coefficients are very high. This is because in addition to hydrodynamic vehicular diffusion, their defect protons exchange with the protons of the surrounding water via hydrogen bond rearrangement in a structural diffusion process.[113] It should be noted that this is not a one dimensional mechanism involving several concerted proton transfer events in what is referred to as Grotthuß mechanism. Instead, state of the art theory encompasses a three-dimensional process involving the hydrogen bond breaking and forming of many of the surrounding water molecules, coupled to the proton transfer within the primary hydration shell (Figure 3.22). The implication is that structural diffusion requires the presence of an excess amount of water.
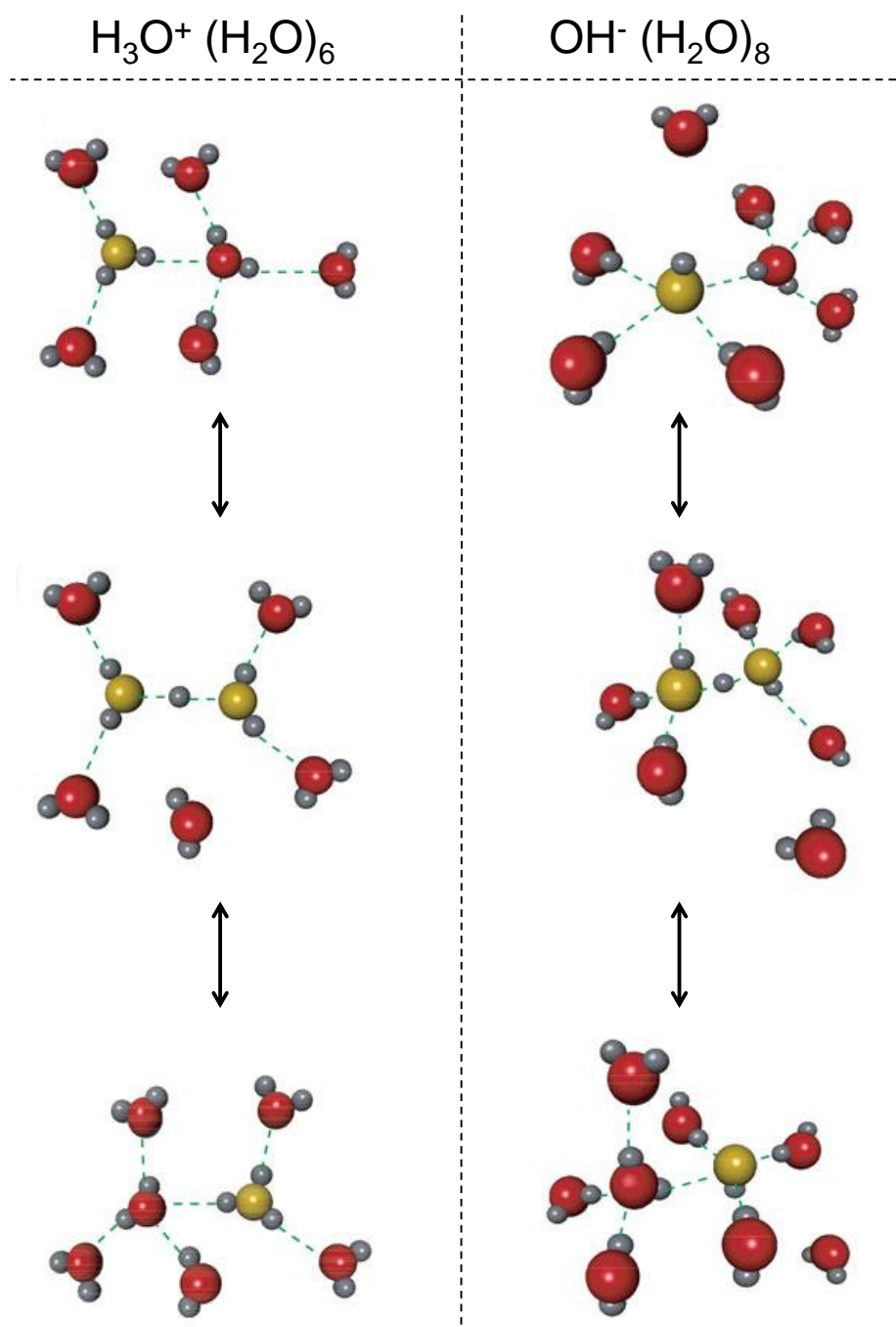
Figure 3.22: Illustration of the hydronium and hydroxide structure diffusion in water showing the rearrangement of the directly involved water molecules. Further solvent relaxation occurring in farther out hydration shells is not depicted. This figure is reproduced from Tuckerman et al 2002. [113,114]

3.2.2   Transport in hydroxide exchange membranes

Judging from the difference in ionic mobility of OH^- and H^+, hydroxide and proton exchange membranes (HEMs and PEMs) would be expected to show a conductivity difference of about a factor of two (Table 3.8). In experiments this is almost never the case and instead HEMs exhibit unexpectedly low conductivities compared to PEMs (especially Nafion) at equal ion exchange capacity.[51,80,82,115–119]

One of the reasons for this observation is likely the rapid carbonate formation that occurs in HEMs which come into contact with CO_2. In the experimental FAA-3 anion exchange membrane that was used throughout this work to investigate transport phenomena, more than 60 % of the hydroxide was converted to carbonate in less than 5 minutes when it came into contact with ambient air (Figure 3.23). As long as hydroxide is available CO_3^{2-} will form and only once OH^- is depleted and further CO_2 is still present, bicarbonate forms in a matter of hours and predominates in the equilibrium.

$$2OH^- + CO_2 \rightleftharpoons OH^- + HCO_3^- \rightleftharpoons H_2O + CO_3^{2-} \overset{CO_2}{\rightleftharpoons} 2HCO_3^-$$
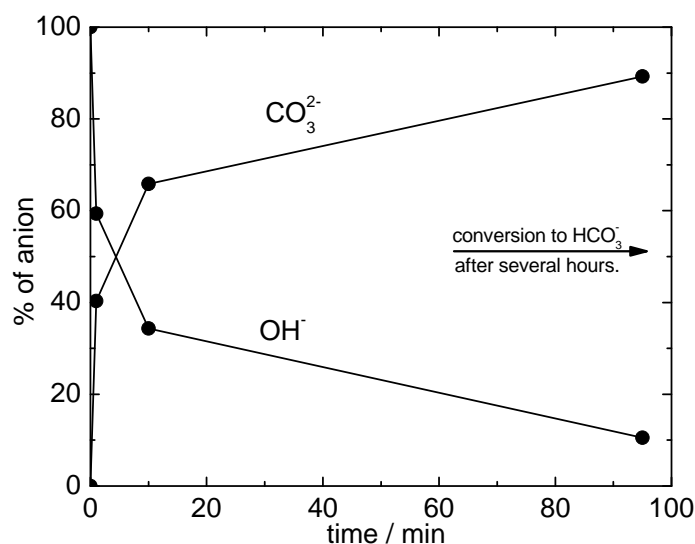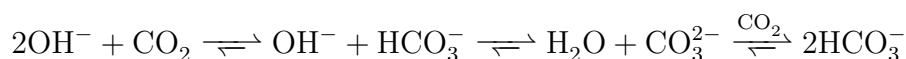
Figure 3.23: The initial conversion of hydroxide to carbonates proceeds rapidly when a HEM is exposed to ambient air. After several hours bicarbonate dominates in the equilibrium if further CO_2 is present.

Carbon dioxide contamination in a HEM results in the replacement of fast hydroxide charge carriers with carbonates that have a lower mobility. Additionally, the conversion to carbonates reduces the water uptake of a membrane noticeably. Both these factors contribute to a considerable reduction of membrane conductivity (Figure 3.24), which means that meticulous exclusion of CO_2 is required to conduct measurements on pure OH^- form membranes. In this work contamination was avoided by conducting all OH^- membrane preparations and measurements in a CO_2-free atmosphere (see experimental section).
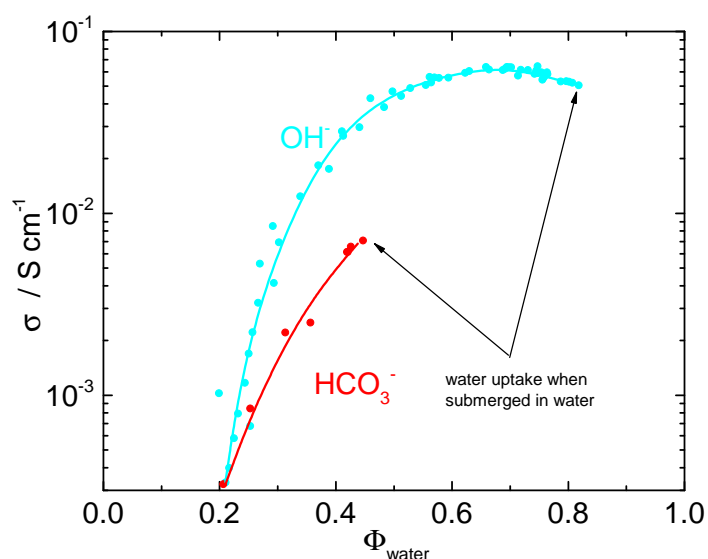
Figure 3.24: Conductivity of the FAA-3 AEM in hydroxide and bicarbonate form at 25 °C. The lower conductivity of a bicarbonate membrane is caused by both the reduced charge carrier mobility and a lower water uptake at equal water activity.

While carbonate contamination has been known to be an issue for several years,[120] the differences in water uptake as a contributing factor were only recently brought to the attention of the AEM community during the course of this thesis.[121] Still, it is hard to imagine that all previous low conductivity results of HEMs were only due to carbonate contamination. Other factors are probably involved and to find them, the diffusion coefficients of water (D_{H_2O}) and hydroxide (D_σ) in a HEM at varying water contents were investigated. In Figure 3.25 these diffusion coefficients are plotted over the water volume fraction Φ_{water} with

$$\Phi_{water} = \frac{V_{H_2O}}{V_{H_2O} + V_{dry}}$$

were V_{H_2O} is the volume of the absorbed water and V_{dry} is the volume of the dry membrane.
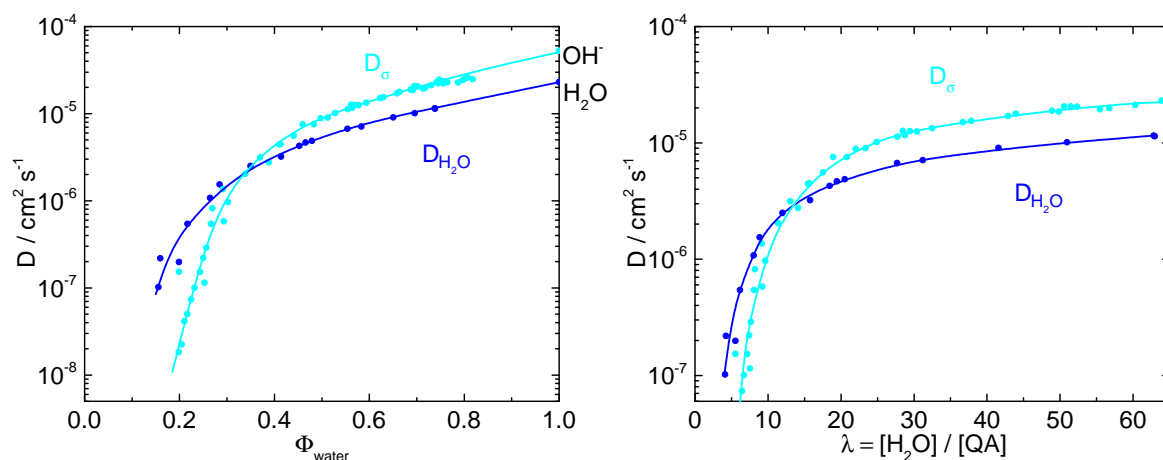
Figure 3.25: Diffusion coefficients of water (D_{H_2O}) and hydroxide (D_σ) for an FAA-3 hydroxide exchange membrane at 25 °C.

Several features and trends can be observed from this plot. In the high water content region were $0.6 < \Phi_{water} < 1$, the water and OH^- diffusion coefficients remain at a constant ratio and approach their respective infinite dilution values (see Table 3.8). This means that the factors that are responsible for the mobility reduction in this region affects both hydroxide and water to the same extent. It seems therefore reasonable to assume that the involved transport processes remain basically unchanged in this region and are locally comparable to those in a dilute solution, which is to say that the transport does not change on a molecular scale. This is supported by the observation that activation energies E_a changes only little here (Figure 3.26). The gradual reduction of the diffusion coefficients are therefore probably caused by decreasing percolation inside the membrane, affecting both species equally.

For $\Phi_{water} < 0.6$, water and hydroxide diffusion decreases much more steeply and the ratio changes, with OH^- mobility falling noticeably faster. It actually falls below those of water despite exhibiting a higher dilute solution diffusion coefficient than H_2O. Obviously, factors that influence water and hydroxide diffusion disproportionally have to be responsible.

The difference between water and hydroxide transport is that hydroxide gains superior mobility due to structural diffusion. As mentioned earlier (see Section 3.2.1), this requires the presence of a sufficient number of water molecules.[114] With a reduction of the water volume fraction, the number of available water molecules for the hydration of both hydroxide and the quaternary ammonium decreases though, and this gradually inhibits structural diffusion until it ceases completely. At this point only hydrodynamic vehicular
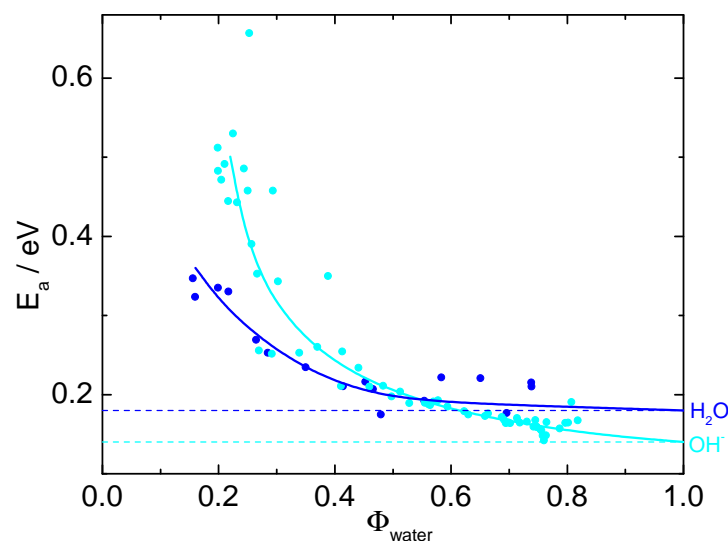
Figure 3.26: Activation energies (25 - 65 °C) of hydroxide and water transport in the FAA-3 HEM at varying water contents. Baseline values were taken from literature data.[122–125]

diffusion remains for the hydroxide transport. Since the OH⁻ anion is stronger coordinated by the surrounding water (and therefore has a larger hydrodynamic radius) than the water molecules themselves, this is one reason why hydroxide mobility falls below the diffusion coefficient of water. The other reason is that the ammonium hydroxide moieties likely begin to condensate with decreasing water content (see also Section 3.2.4), despite quaternary ammonium hydroxides being strong bases.[79,126] To what extent these two factors influence the hydroxide transport in the low water content region is not clear yet though.

The above points become clearer when the transport data of the HEM is compared with those of a perfluorinated sulfonic acid (PFSA) Nafion membrane in which the sulfonic acid groups are attached via long side chains, and a linear sulfonated poly(ether ether ketone ketone) (S-PEEKK), which is structurally similar to the HEM in which the functional groups are directly attached to the polymer backbone (Figure 3.27).

At high water contents, diffusion in the S-PEEKK and HEM decreases with equal ratios with Φ_{water} for OH⁻, H⁺ and H_2O (Figure 3.28). The water diffusion coefficients for HEM and S-PEEKK are actually equal to each other over the whole water content range, suggesting a similar nano-morphology of the polymer/water phase separation. Hydronium diffusion on the other hand decreases noticeably less in comparison to hydroxide at low water contents.
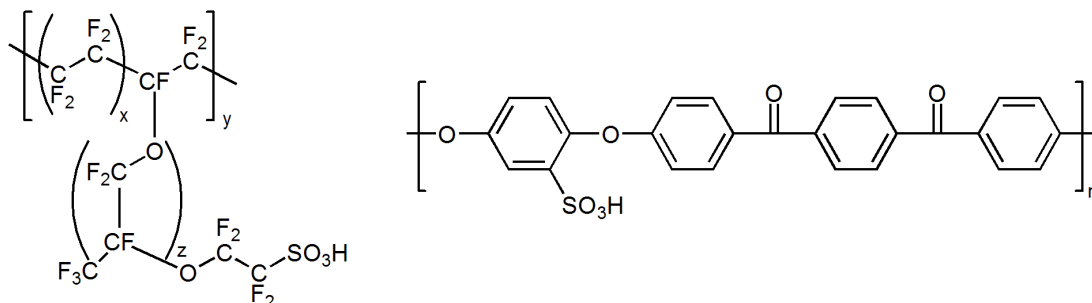
Figure 3.27: Molecular structure of the PEMs Nafion (left) with sulfonic acid groups attached to long side chains and S-PEEKK (right), in which the functional groups are directly tethered to the backbone in a similar fashion as in the HEM, which has a similar structure to the polysulfone shown in Figure 1.5.
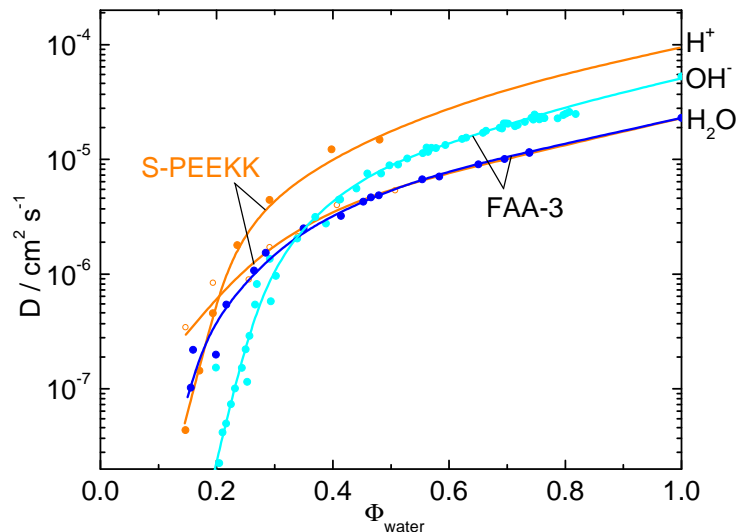
Figure 3.28: Hydroxide mobility of HEM compared to the H^+ mobility in a structurally similar S-PEEKK membrane. While water mobility is basically the same over the entire water content range, hydroxide diffusion falls more rapidly than that of H^+, probably because of its lower tendency to dissociate and a requirement for more water molecules in its structure diffusion process.

Since nano-morphology is assumed to be the same due to water diffusion data and similar backbones, this is likely caused by the different properties of the functional groups ($-NR_3OH$ vs $-SO_3H$) and the charge carrying ions themselves. The stronger tendency for $-SO_3H$ to dissociate when compared to $-NR_3OH$ is probably responsible for a higher charge carrier concentration in the S-PEEKK, increasing the $D_\sigma(H^+)$ values compared to $D_\sigma(OH^-)$. Possibly, differences in the hydration requirements for structural diffusion of H^+ and OH^- plays an additional role, but both ions should be affected to some extent. It is probably a combination of both these factors that results in a reduction of hydroxide mobility compared to excess protons, which also explains the faster rise in E_a (which contains contributions from dissociation and transport processes) of the hydroxide compared to the hydronium (Figure 3.29).
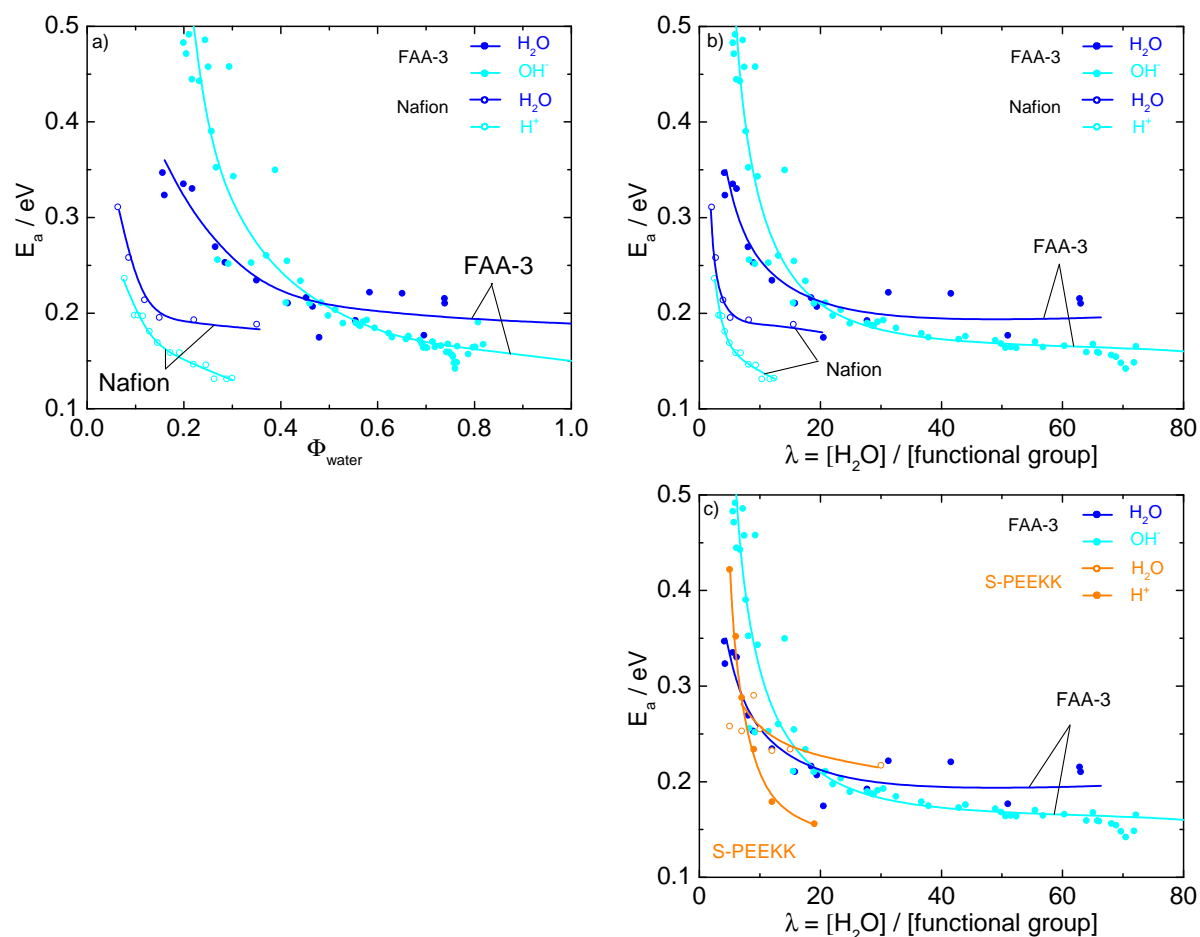
Figure 3.29: Activation energies of ionic charge carrier and water diffusion in the PEMs Nafion, S-PEEKK and the HEM FAA-3 plotted over the number of water molecules per functional group λ and the water volume fraction Φ_{water}.

When the transport properties of the FAA-3 HEM are compared to the literature PEM standard Nafion, even more significant differences are observed (Figure 3.30). Both charge carrier and water diffusion in Nafion are noticeably higher than in HEM and S-PEEKK, which is especially pronounced at low water contents and the activation energies show a similar trend (Figure 3.29). This is mainly a result of its more pronounced phase separation that makes the water domains locally more similar to bulk-water. That means in Nafion, water and hydronium transport is less constraint by the polymer phase and percolation is likely more efficient within the aqueous domain. Additionally, its super-acidic perfluorinated sulfonic acid groups are expected to remain dissociated down to lower water contents compared to S-PEEKK or HEM. The superior transport properties of Nafion are therefore a consequence of high dissociation and locally more bulk-like water in addition to more efficient percolation,[77] even at reduced water contents.
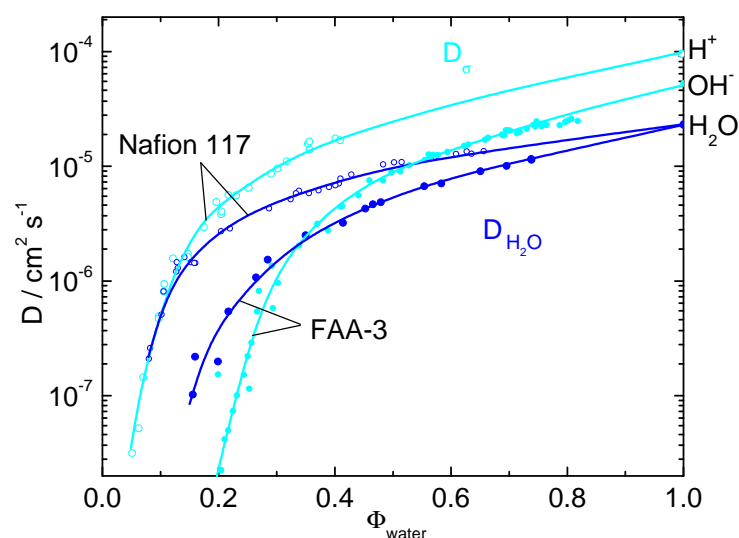
Figure 3.30: Charge carrier and water diffusion in HEM FAA-3 and PEM Nafion.

From the data one can conclude that HEMs can in principle reach conductivities within a factor of two of PEMs at sufficient hydration. At high water contents the difference in mobility is only due to the dilute water transport properties D_σ^∞ of H^+ and OH^-. At lower water contents a reduced degree of dissociation and, compared to PFSA materials, an inferior phase separation and percolation is responsible for lower ionic mobility.

While investigation of the hydroxide form already gave some insights into AEMs, a better understanding of especially counter-ion condensation and the influence of the anion on hydration can potentially be acquired from investigating AEMs in other anionic forms.

3.2.3 Transport in halide exchange membranes

Changing the kind of anion in an AEM influences basically all membrane properties such as water uptake, density, degree of dissociation, conductivity, and morphology, since they are all interdependent parameters. Water uptake and density are the most tangible and easily determined, which is why this aspect is discussed first.

Membrane density in the dry, water-free state increases in a linear fashion with regard to the molecular weight of the anion (Figure 3.31), which is unsurprising since the only difference here is the molecular weight of the anion while other parameters remain equal. By submerging the membranes in water and recording the water uptake something more interesting is observed. Notwithstanding the fact that a rough correlation with respect to the base dissociation constant pK_B is found, an anomaly is evident for the hydroxide and fluoride forms, which absorb around 5 times more water than the other anion forms (Figure 3.32).
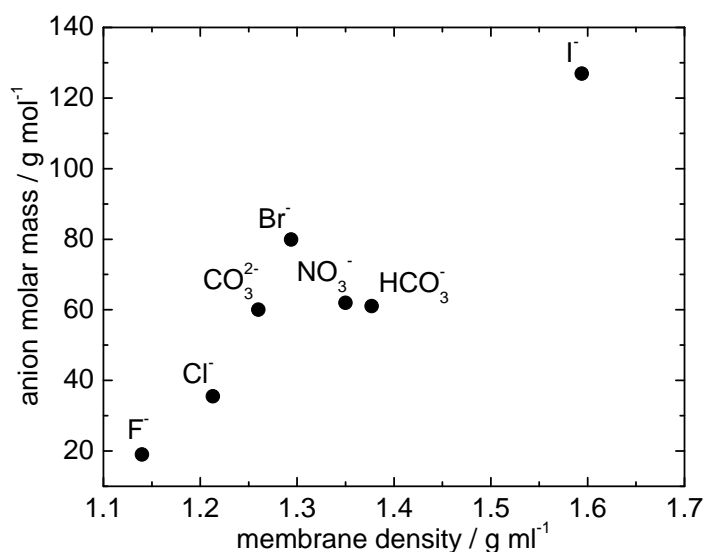
Figure 3.31: Dry density of the FAA-3 AEM changes almost linearly with the molar mass of the anion. The ion exchange capacities in the dry state are $IEC_{F^-} = 2.18$, $IEC_{Cl^-} = 2.1$, $IEC_{Br^-} = 1.92$, $IEC_{I^-} = 1.76$, $IEC_{HCO_3^-} = 1.99$, $IEC_{CO_3^{2-}} = 2.12$, $IEC_{NO_3^-} = 1.99$.

To explain these observations the energetic contributions from the interactions of ions, solvent and polymer, including entropy have to be considered. These include among other factors, enthalpy of dissolution of the ions, entropy of dilution, and the membrane polymer cohesion (i.e. membrane counter pressure).
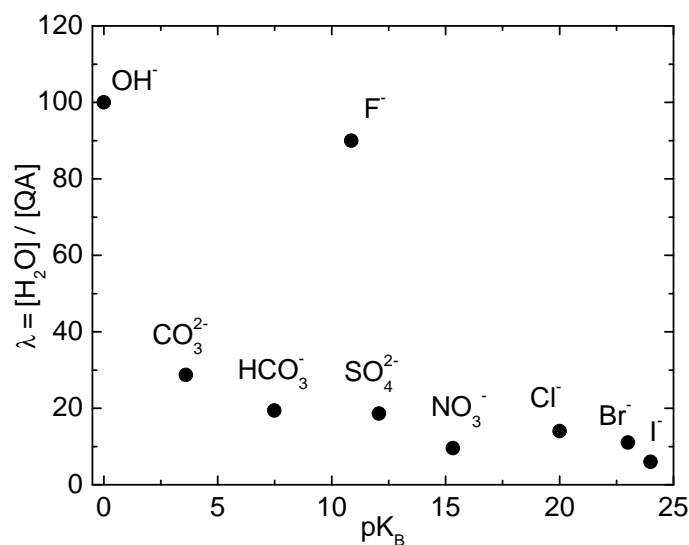
Figure 3.32: Water uptake at room temperature of the FAA-3 AEM scales roughly with pk$_B$, with the exception of the hydroxide and fluoride forms.

The enthalpy of dissolution ΔH_{diss} of a salt includes the processes of dissociation and solvation of ions in water.

$$\mathrm{NR_4X}_{(solid)} + \mathrm{H_2O} \xrightarrow{\text{dissolution}} \mathrm{NR}_{4(solv.)}^+ + \mathrm{X}_{(solv.)}^-$$
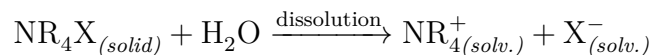
This is also a crucial factor in determining the degree of dissociation of ion pairs in a membrane in the absence of a crystal lattice. The ΔH_{diss} values for a number of ammonium salts are listed in Table 3.9 and provide insights into the general trends. Tetramethylammonium fluoride and hydroxide form data was unavailable, so corresponding cesium salts were included for comparison. The solution enthalpies for chloride, bromide and iodide fall faster for ammonium compared to cesium, so it can be expected that the NR$_4$F and NR$_4$OH enthalpies are even more negative than those of cesium.

The more negative ΔH_{diss} is, the more exothermic is the dissolution process. The same trends as those in Table 3.9 would be expected from Pearson's HSAB concept which states that small and weakly polarizable ("hard") anions bind more strongly to hard cations, while large, highly polarizable ("soft") anions prefer other soft cations.[127] Accordingly, hydration and dissociation (dissolution) of the membrane form ions is expected to follow the same trend and in light of this, it is not surprising that the membrane water uptake in water and in humidified atmosphere (Figure 3.32 and 3.33) does so as well.

Salt	ΔH_{diss} $(kJmol^{-1})$	Salt	ΔH_{diss} $(kJmol^{-1})$
		CsOH	-71.6
		CsF	-36.7
NMe_4Cl	4.5 (72.0)	CsCl	17.8
NMe_4Br	24.8 (71.9)	CsBr	26.0
NMe_4I	42.4 (108.7)	CsI	33.4

Table 3.9: Enthalpies and entropies (in brackets $JK^{-1}mol^{-1}$) of dissolution of tetramethylammonium and cesium salts in water.[111,128] Enthalpies of the F^- and OH^- forms are expected to be even more negative for ammonium than those of cesium.
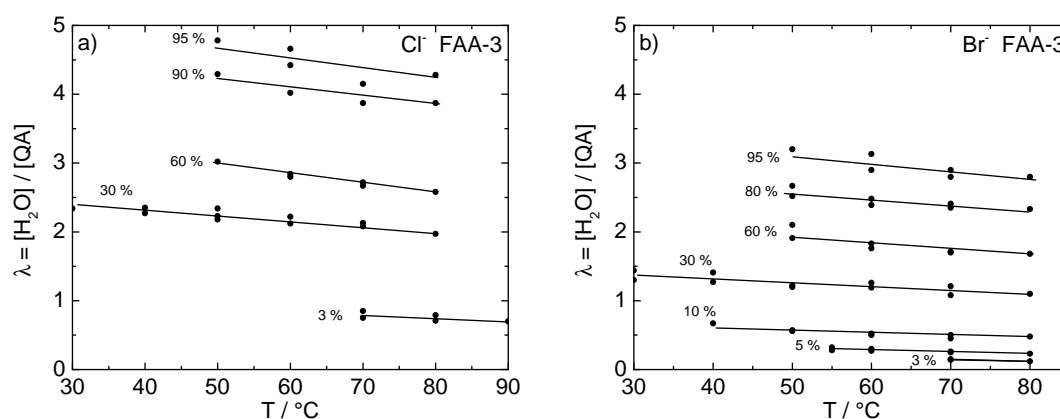
Figure 3.33: Water uptake in λ of the FAA-3 membrane in chloride and bromide form at varying temperature and relative humidity.

The membrane counter-pressure works against the swelling of the AEM. It is a result of the cohesion of the polymer phase, that weakens with increasing temperature due to thermal movement of the polymer chains and changes in their conformational energy. This reduction in membrane counter pressure can indirectly be observed as an increase in water uptake of membranes submerged in liquid water (Figure 3.34).

The onset of exaggerated swelling occurs at lower temperatures for membrane forms with a more exothermic enthalpy of dissolution of the corresponding salt. Since membrane counter-pressure for any kind of anion can be considered equal (as all forms have the same polymer backbone), a higher degree of dissociation (i.e. higher dissociated ion concentration) at a given water content results in an increased entropic driving force (osmotic pressure) for hydration. A higher water content results in further dilution of the ions, increasing their activity and dissociation, which further increases osmotic pressure until membrane counter-pressure is met at the respective temperature. For the iodide form

membrane with a highly endothermic dissolution enthalpy this leads to barely any water uptake even at $T = 100$ °C. While too much swelling can lead to irreversible damage and even membrane dissolution, it is necessary for good ionic conduction.
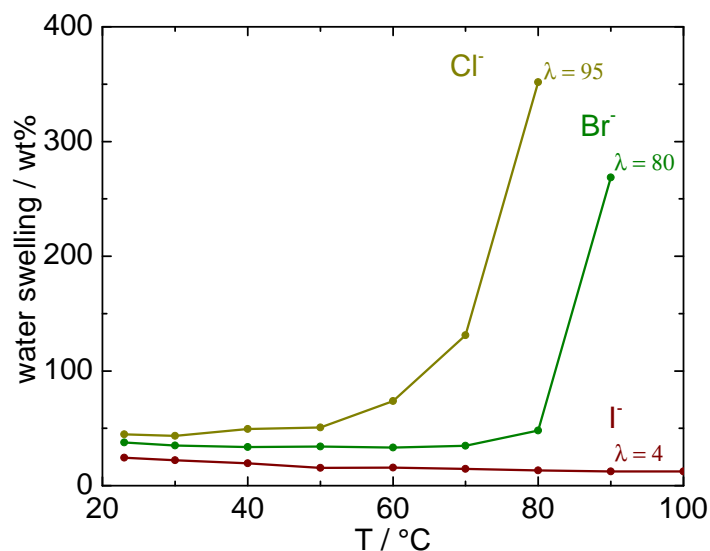
Figure 3.34: Temperature dependent water uptake of FAA-3 AEM in different anionic forms submerged in water.

Membrane conductivity changes, as mentioned above, with the kind of anion just as basically all other properties do, but anion dilute solution mobilities (Table 3.8) are not sufficient to explain the observed membrane conductivity trends in Figure 3.35. Instead the ratios of the conductivity curves of different AEM forms change and intersect with variation in water content.

For water contents above $\Phi_{water} = 0.3$ conductivity of the different ionic forms increases with $(I^-) < (Br^-) < (Cl^-) < (F^-) < (OH^-)$, in accordance with the enthalpies of solution in Table 3.9 but inconsistent with ionic mobilities in Table 3.8. This is especially apparent with the fluoride form, which has the lowest ionic mobility of the plotted anions but the second highest conductivity. In the case of complete ionic dissociation, differences in conductivity should be reflected by ionic dilute solution mobility trends. Since this is not the case, above $\Phi_{water} = 0.3$, among other factors the degrees of dissociation likely differ considerably, with the fluoride form expected to be more dissociated than chloride, followed by bromide and then iodide.
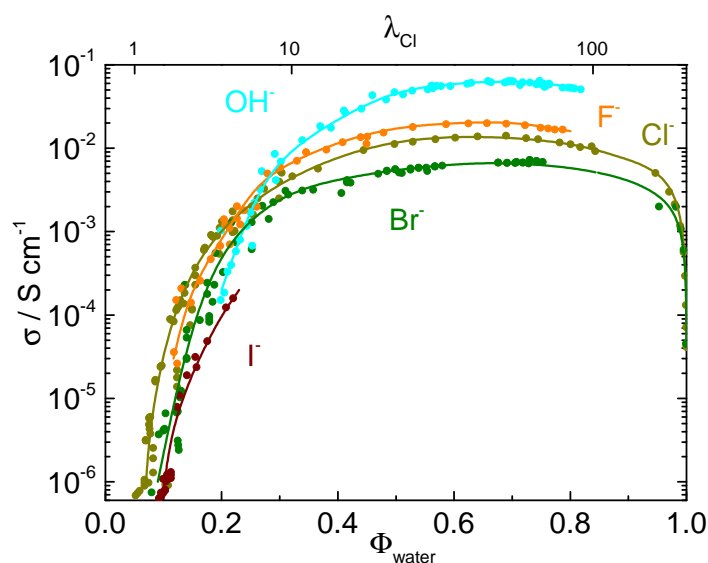
Figure 3.35: AEM FAA-3 conductivities at 25 °C plotted over the water volume fraction. The conductivity curve ratios change and intersect for different anionic forms, due to differences in ionic mobility and degree of dissociation. The top x-axis shows the water content in $\lambda = [\text{H}_2\text{O}]/[\text{QA}]$ for the chloride form membrane.

Below $\Phi_{water} = 0.3$ conductivities sharply decrease, with hydroxide and fluoride form conductivity falling below that of at least some of the other halide forms. With low water contents the ion hydration shells become smaller, reducing electrostatic screening and accordingly the degree of dissociation. The extension of the water domain size is diminished as well, and particularly ions with a large hydration shell are then constraint in their mobility, which can explain the faster conductivity decay for the fluoride form. For the hydroxide form membrane this is also the case, but probably even more severe is its gradual breakdown of structural diffusion with a decreasing number of available water molecules per hydroxide anion (see Section 3.2.1). These factors are apparently sufficient to reduce hydroxide membrane conductivity even below that of all other halides. Above $\Phi_{water} = 0.8$ the reason for the conductivity decrease is due to the high dilution of the charge carriers.

So far, the degree of dissociation α was only discussed in relative terms but it evidently influences membrane conductivity to a considerable extent since only dissociated charge carriers contribute to membrane conductivity. It is actually possible to estimate α in a membrane for hydrodynamically transported ions if certain requirements are met, which is described in the following:

The conductivity diffusion coefficient D_σ is calculated using the Nernst-Einstein equation, with the overall concentration of anions in the sample. Only dissociated ions contribute to conductivity, because undissociated anions are condensed to the immobile cations on the polymer. Accordingly, D_σ is the conductivity diffusion coefficient $D_{\sigma(diss)}$ of the fraction α of the dissociated ions.

$$D_\sigma = \alpha \cdot D_{\sigma(diss)}$$

$D_{\sigma(diss)}$ and α are unknown and have to be derived from available data. For this, it is assumed that $D_{\sigma(diss)}$ can be calculated by multiplying the conductivity diffusion coefficient of an ion in dilute solution D_σ^∞ with a determinable factor P that represents the obstruction of the ionic mobility by the polymer boundaries in the membrane.

$$D_{\sigma(diss)} = D_\sigma^\infty \cdot P$$

If these obstruction effects are the same for ion mobility and water diffusion, P can be estimated by the ratio of the water tracer diffusion coefficient D_{H_2O} to its dilute solution value $D_{H_2O}^\infty$ at a given water content.

$$P = \frac{D_{H_2O}}{D_{H_2O}^\infty}$$

The degree of dissociation can now be calculated from the measured D_σ and D_{H_2O} data, together with the literature values of D_σ^∞ and $D_{H_2O}^\infty$, after substitution and solving for α.

$$\alpha = \frac{D_\sigma}{D_{H_2O}} \cdot \frac{D_{H_2O}^\infty}{D_\sigma^\infty}$$

This formula only holds true for water contents at which the water diffusion coefficient is negligibly affected by its solvation of the ions. If the diffusion of a noticeable proportion of the water molecules is restricted by solvation, the assumption that ion and water diffusion are reduced to the same extent is no longer true.

Therefore, degrees of dissociation can only be calculated for water contents about $\lambda > 20$ or $\Phi_{water} > 0.4$. Below these values the number of H_2O molecules in the hydration shells of cation and anion constitute a considerable proportion of the total water. This can be seen in Figure 3.36, which shows that the diffusion coefficient in the hydroxide form membrane is noticeably lower than in the halide forms. Since the diffusion coefficient of the water of

hydration is lower compared to bulk water, the overall diffusion coefficient decreases. This effect is far more distinct for hydroxide than for the halides, due to its stronger hydrogen bonds. Even so, it likely also exists for the other kinds of ions, which is why only water contents above the mentioned values were assumed to be valid for the above equation. At
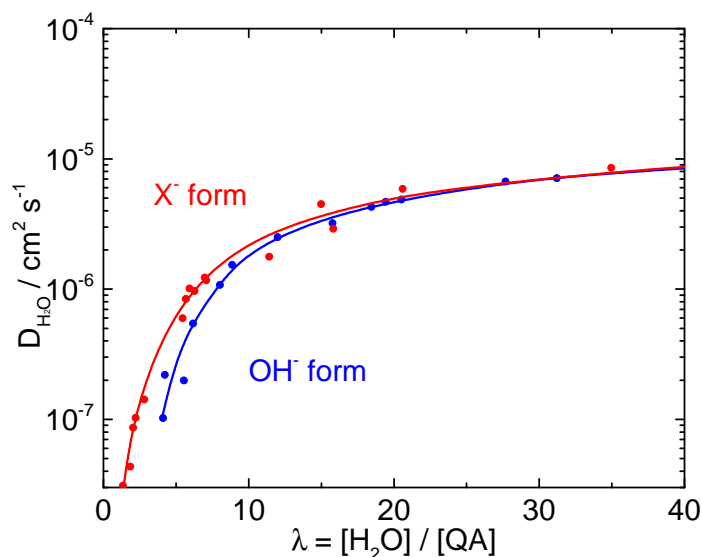
Figure 3.36: The water diffusion coefficient of the hydroxide (blue) and halide form (red) membranes at 25 °C. In the HEM D_{H_2O} is reduced at low water contents due to strong hydrogen bonds.

higher water contents D_{H_2O} is equal for halide and hydroxide (and probably also fluoride which was not measured) forms, since the fraction of water molecules in the hydration shell decreases, until their effect on D_{H_2O} is negligible. D_{H_2O} then equals the diffusion coefficient for the bulk water in the membrane, only obstructed by the polymer walls. This then allows for the determination of α for the hydrodynamically diffusing halides, as described above.

Below $\Phi_{water} = 0.4$ a dramatic increase in the activation energy of the ion transport is observed (Figure 3.37), which is probably caused by an energetically more demanding dissociation due to the decreasing number of water molecules for charge separation in addition to the reduced mobility from polymer obstruction. As it is unclear as to how much these factors contribute to the E_A increase, this is another reason why the equation for the the determination of α only holds at higher water contents.

A prerequisite for the application of the above equation is that the ionic membrane conductivity σ is directly correlated with D_σ via the Nernst-Einstein equation (see Section 2.3),
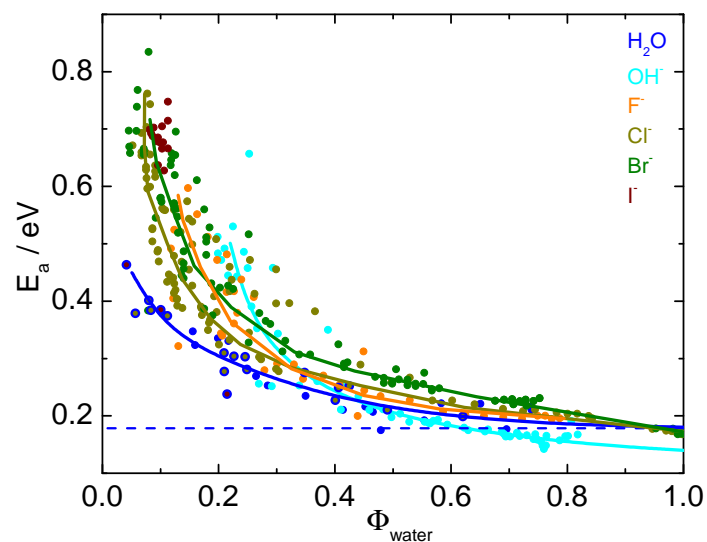
Figure 3.37: Activation energies of halide and hydroxide mobility as well as water diffusion in the FAA-3 AEM (25 - 65 °C). No difference in the water diffusion activation energy can be discerned between the halide and hydroxide forms due to the data scatter. The dashed line marks the pure water diffusion activation energy. Above $\Phi_{water} = 0.4$ E_A for ion transport begins to rise steeply, possibly due to both more energetically demanding dissociation and increased interactions with the polymer at lower wter contents.
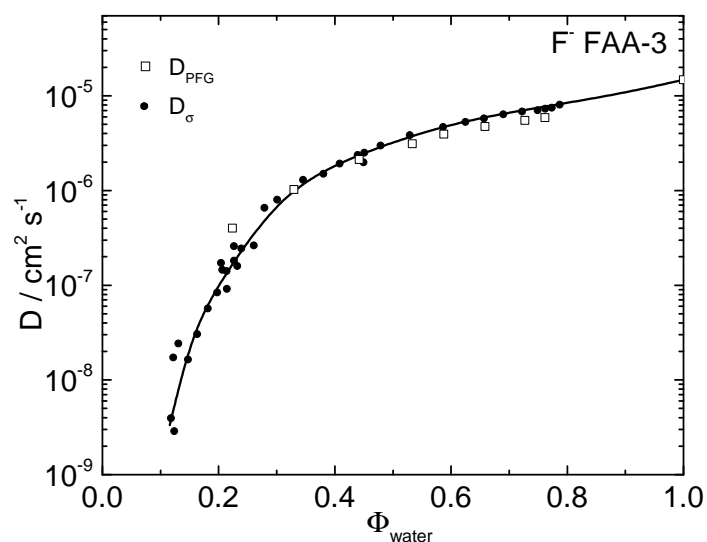
Figure 3.38: Conductivity diffusion D_σ and PFG tracer diffusion coefficient D_{PFG} of the fluoride form membrane at 25 °C are in reasonable agreement, suggesting that the diffusion coefficients calculated from conductivity data using the Nernst-Einstein equation are valid. Note that water tracer diffusion was not measured for the fluoride form membrane.

i.e. ion mobility in an electric field is affected to the same extent as random ionic diffusion. Therefore, fluoride tracer diffusion coefficients $D(\text{F}^-)$ were determined and compared to the corresponding $D_\sigma(\text{F}^-)$ values received from impedance spectroscopy, and fortunately found to be in reasonable agreement (Figure 3.38).

The dissociation α calculated from diffusion data follow the same trend that was qualitatively expected from water swelling and conductivity (Figure 3.39). Interestingly, while the ionic diffusion coefficient varies considerably with the anion, water diffusion is basically unaffected. Note, that no water tracer diffusion coefficient was recorded for the fluoride form membrane; though since $D_{\text{H}_2\text{O}}$ is equal for the other halide forms over the whole water content range, and above $\Phi_{water} \approx 0.5$ even for the halide and hydroxide form membranes (Figure 3.36), the water diffusion trend-line for halide form membranes is also used for the fluoride form.
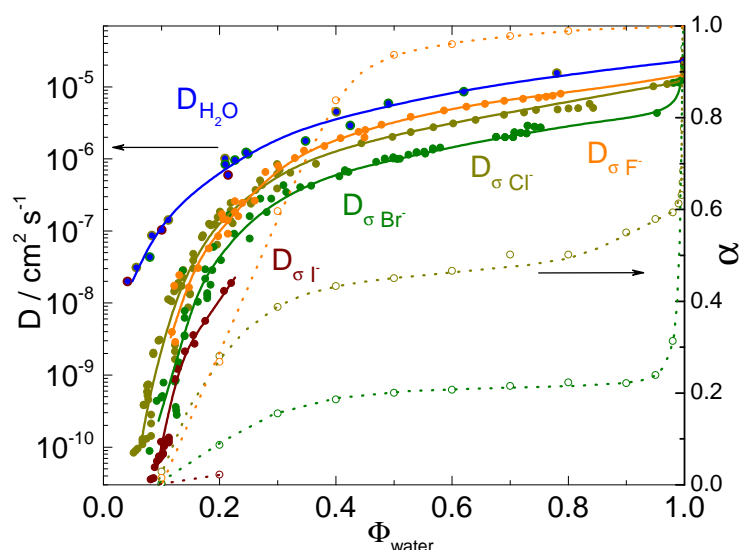
Figure 3.39: Diffusion coefficients (solid lines) and degrees of dissociation (dotted lines) at 25 °C plotted over the water volume fraction. While water diffusion is independent of the anion, the ionic diffusion coefficient changes considerably, resulting in different degrees of dissociation. Below $\Phi_{water} \approx$ 0.4 the dissociation data is speculative, since it is unclear whether the reduced ionic mobility is due to reduced dissociation or interactions with the polymer.

The iodide form membrane barely dissociates, in accordance with its highly endothermic enthalpy of solution and almost non-existent swelling. Dissociation then increases for bromide and even more for chloride. Interestingly, α seems to rise up to $\Phi_{water} \approx 0.4$, where it reaches a plateau on which dissociation remains almost constant. Only at extremely high

water contents dissociation further increases towards 1. The plateaus suggest the formation of positively charged condensates of multiple ions (Figure 3.40) due to electrostatic interactions and ionomer conformation, giving rise to ionic cross-links and tightly packed polymers. Only at very high water contents $\Phi_{water} > 0.99$ these multi-ion condensate apparently fall apart in the course of membrane dissolution, leading to an increased degree of dissociation. This is shown in more detail with a dissolved chloride form membrane in Figure 3.41.
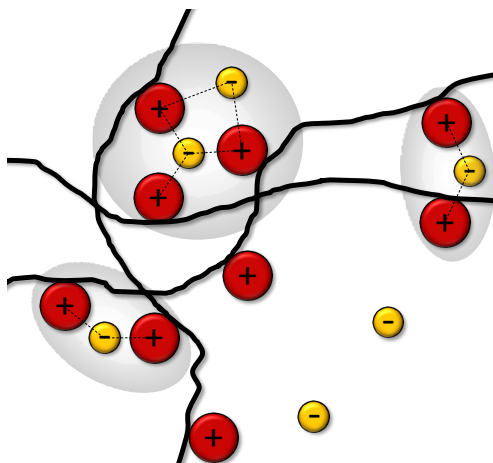
Figure 3.40: Schematic illustration of discreet condensates of multiple ions, which may lead to incomplete dissociation and ionic cross-links. Water molecules are not shown.
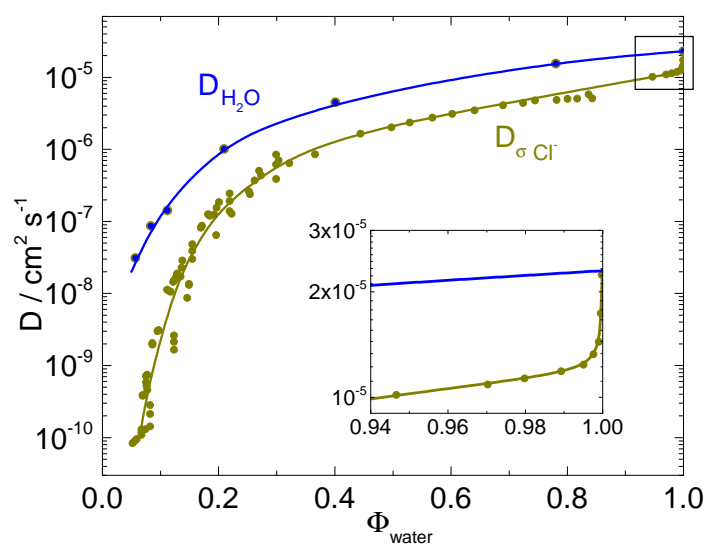
Figure 3.41: Diffusion coefficients of water and chloride in a Cl$^-$ form AEM at 25 °C suggest a complex dissociation behavior.

The plateau is definitely found for the chloride and bromide membrane forms (at $\alpha = 0.45$ and 0.2 respectively) and likely exists for the iodide form as well (at $\alpha < 0.05$). The

fluoride form on the other hand is basically completely dissociated at $\Phi_{water} > 0.5$ with no readily discernible plateau. For the hydroxide form, it seems reasonable to assume that it is completely dissociated to an even higher degree than the fluoride form, since it has a far more exothermic enthalpy of solution and $D_\sigma(OH^-)$ nicely approaches $D_\sigma^\infty(OH^-)$ (with the exception of some minor scatter at $\Phi_{water} = 0.8$, which are probably an artifact due to incomplete electrode contact at these extreme states of hydration).

Complete dissociation would actually be expected from all halide salt forms as well, since the corresponding monomeric alkyl-ammonium species all exhibit strong-electrolyte properties, as evidenced by a straight line in a Kohlrausch plot (Figure 3.42). Apparently, the strong electrolyte property of tetramethylammonium halides changes to a weak electrolyte behavior, simply because of the attachment of the cations to a polymer. Incomplete charge dissociation due to attachment to a polymer chain is a phenomenon known as polyelectrolyte effect. Commonly, the term is used if the distance between charges on a single polymer chain is smaller than the Bjerrum length λ_B of the solvent and the charges are therefore not completely screened. This is not the case here, since even in the dry state of e.g. the chloride form AEM the charge distance is larger (ca. 0.99 nm) than the Bjerrum length in water ($\lambda_B = 0.7$ nm) and α can therefore become 1. The case with the AEMs here might be described as a kind of pseudo-polyelectrolyte effect.
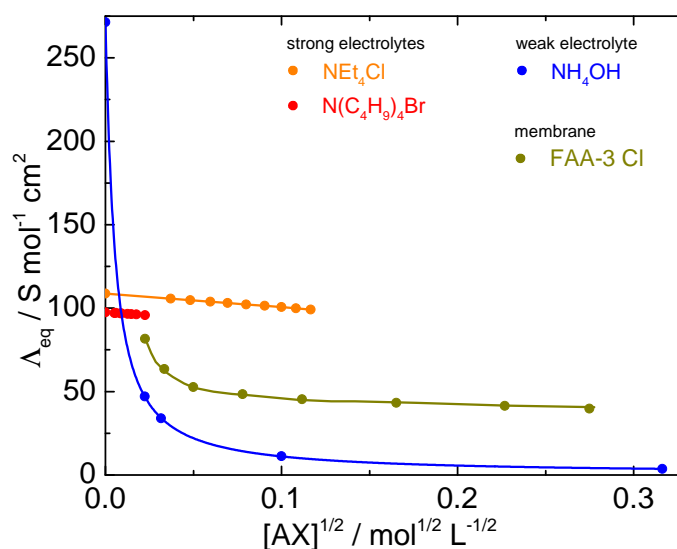
Figure 3.42: The equivalent conductivity of strong electrolytes show a straight line in a Kohlrausch plot. The strong electrolyte behavior expected from quaternary ammonium halides changes to that of a weak electrolyte when attached to a polymer.

3.2.4   Nano-morphology

The spatial distribution of the polymeric and aqueous phase in a membrane constitutes its nano-morphology. Its formation is governed by the interplay of the inter- and intramolecular interactions of polymers, ions, and water. Especially water uptake and electrostatic interactions are significant factors.[77,129] If a membrane exhibits a periodicity of the water and polymer domain structure on the nanometer scale, this structural correlation is observed as an ionomer peak in a SAXS pattern (Figure 3.43).
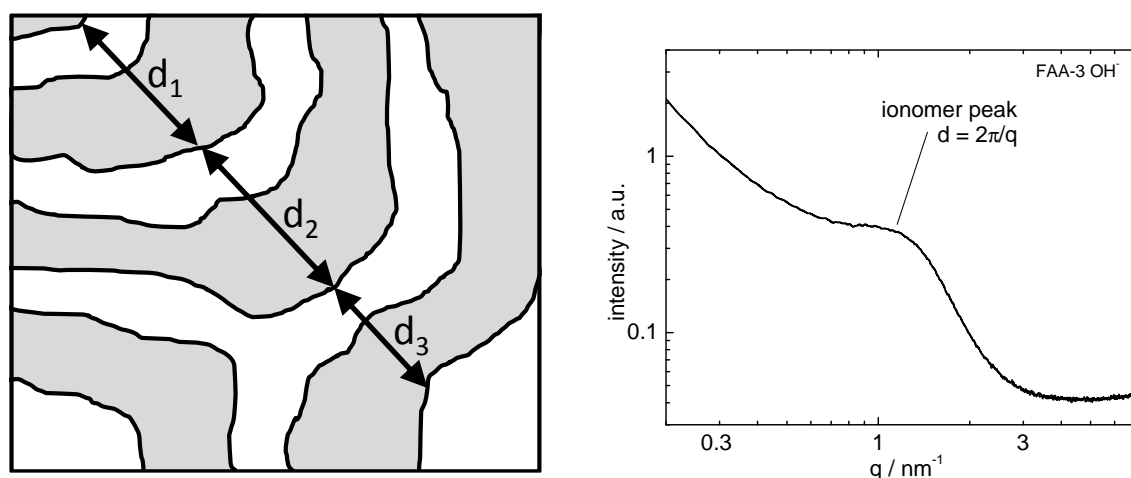
Figure 3.43: The ionomer signal in a SAXS pattern (of an FAA-3 HEM on the right) corresponds to the distances d_n of the correlation lengths of water and a polymer layers (left).

With varying water content the water/polymer ratio in a membrane changes, resulting in different correlation lengths, corresponding to a shift of the ionomer signal. From the scaling behavior of the ionomer peak with varying polymer volume fraction $\Phi_{polymer}$, it is possible to gain information about the dimensionality of the phases (Figure 3.44).

This requires an accurate determination of the ionomer peak position on the q-scale, which was obtained by a fit consisting of the sum of two Gaussian functions (Figure 3.45). Only for the hydroxide form membrane the ionomer peak could always be precisely determined, while other forms (e.g. bromide) did not display distinct correlation lengths (Figure 3.46). This illustrates that for the bromide form, water and polymer layer thickness is uncorrelated on the length scale of the measurement. Since electrostatic interactions, which are dependent on the degree of dissociation, probably drive the formation of the phase separation on the nanometer scale,[77] this is another indication that the bromide form membrane is dissociated only to a low degree, in comparison to the hydroxide form.
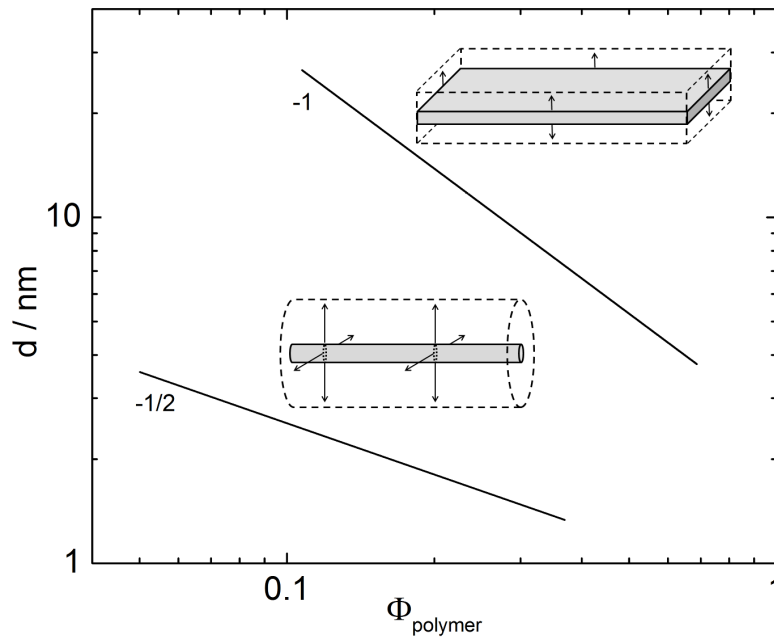
Figure 3.44: In a logarithmic plot of ionomer maximum d over polymer volume fraction $\Phi_{polymer}$ a slope of -1 and -1/2 suggest a one- and two-dimensional scaling respectively.
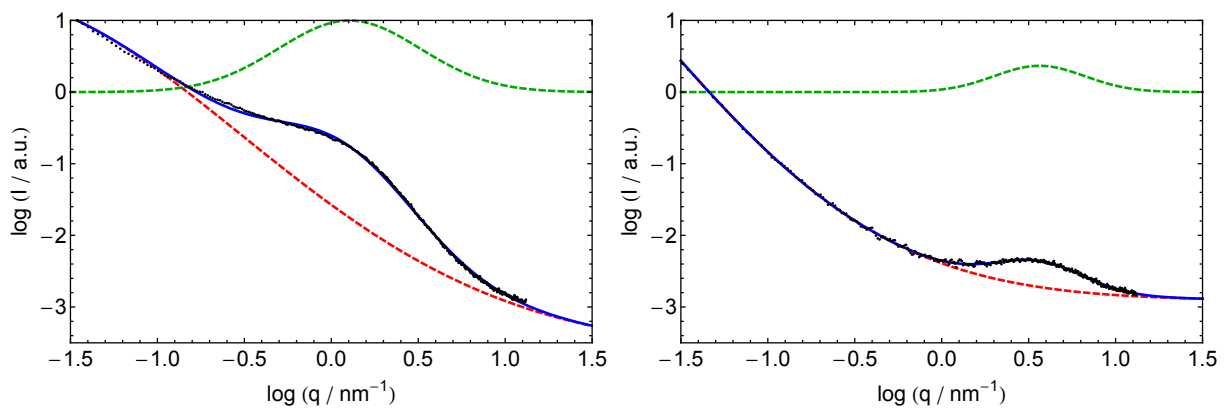
Figure 3.45: Two examples of the SAXS pattern data (black dots) that were fitted with *Mathematica* by the sum of two Gaussian functions (green and red dashed lines), resulting in the blue line. The fits are sufficient to determine the maximum of the ionomer peak, which corresponds to the median of the green curve.
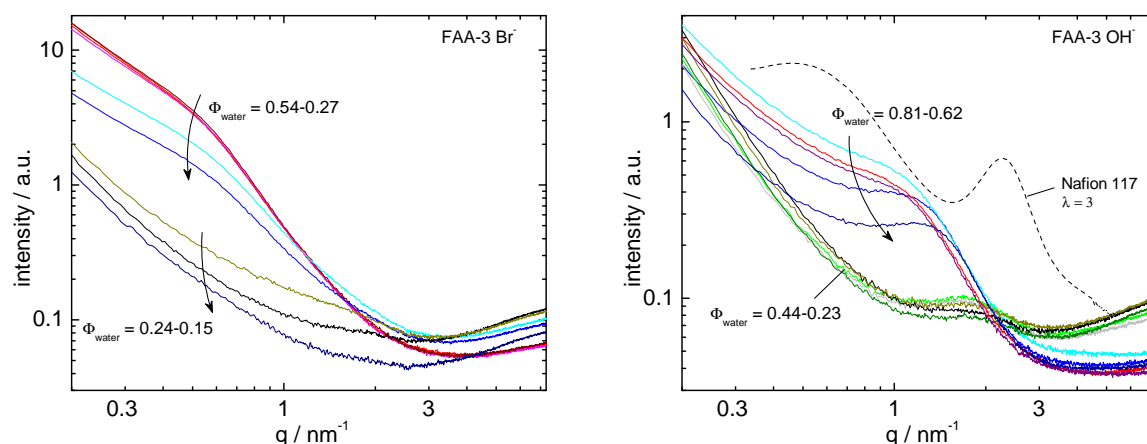
Figure 3.46: In the bromide form no distinct ionomer peaks are observed, while the hydroxide form shows them clearly. This difference probably result from the bromide form being far less dissociated than the hydroxide form. Still, even in comparison to the HEM the super acidic Nafion exhibits far superior phase separation.

The ionomer maximum plotted over the polymer volume fraction $\Phi_{polymer}$ scales with the slope of -1/2 for the HEM (Figure 3.47). As shown in Figure 3.44, this is characteristic for a two-dimensional expansion of the aqueous domain with increasing water content (e.g. tubes, ribbons, columns) The slope remains at -1/2 down to low water contents, in contrast to Nafion in which the scaling behavior changes from -1/2 to -1 below $\Phi_{polymer} = 0.5$ from a two-dimensional to a one-dimensional (e.g. sheets, films, layers) volumetric change.

This scaling change in Nafion has been suggested to be caused by (among other factors) electrostatics.[77] Once the dissociated ion pairs are insufficiently screened by the solvent due to reduced water content, hydronium ions may stabilize between more than one of the negatively charged sulfonate groups on the Nafion polymer chains (ionic cross-links). In flat structures the accumulation of positively charged ions is reduced compared to cylindrical ones (Figure 3.48), lowering electrostatic energy and facilitating the formation of ionic cross-links, thereby driving the rearrangement of the morphology. This only occurs if the charges are dissociated even at low water contents where electrostatic screening is incomplete, as is the case for Nafion due to its superacidic nature. Flat morphologies seem to be a general structural feature of ionomer membranes with this property.[77] If ion-pairs condensate once they are no longer completely screened by the solvent, this would lead to a loss of the structural correlation (i.e. ionomer peak) in the SAXS-pattern, which is not observed for Nafion membranes until $\lambda \approx 1$ (compare Nafion at $\lambda = 3$ in Figure 3.46).[77] In the AEMs on the other hand, this is apparent in the bromide form membrane for the

whole water content range, and to a lower degree for the HEM at reduced water contents. In case of ion pair condensation at reduced water contents, electrostatic interactions of the remaining dissociated ions may be insufficient to drive a rearrangement of the morphology. This is an explanation for the unchanging scaling behavior of -1/2 over the whole water content range for the HEM and again suggests a reduction of the degree of dissociation with decreasing water content, as already pointed out in Section 3.2.2.
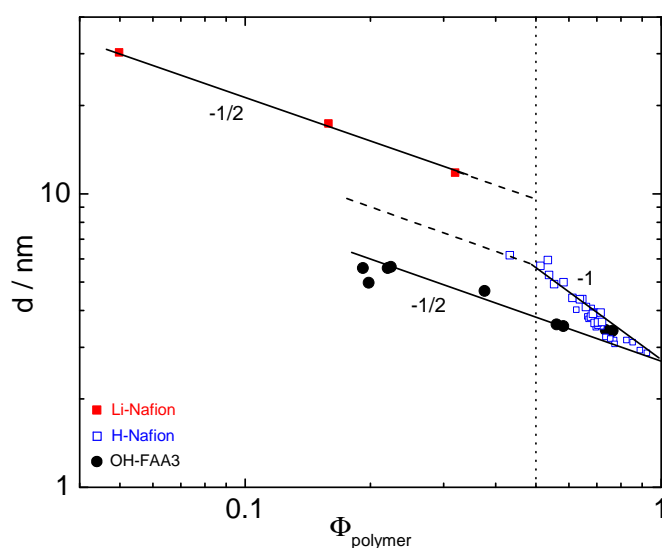
Figure 3.47: While the scaling behavior of Nafion changes from -1/2 to -1 with a water content reduction,[77,129] this is not the case for the HEM. This points towards an insufficient driving force for the restructuring to a locally flat morphology, probably because of counter-ion condensation.
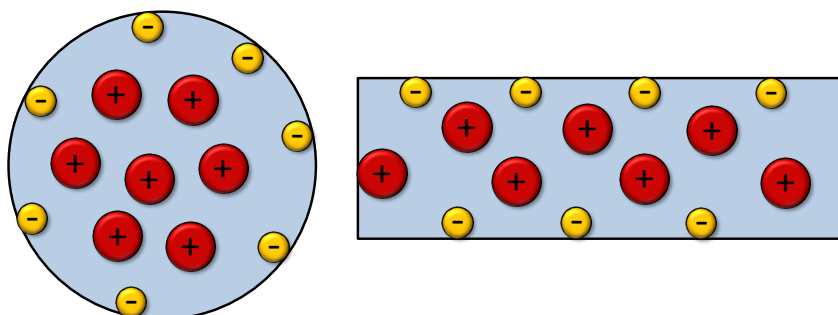
Figure 3.48: In the case of flat water domains, distribution and screening of the positive charges is energetically more favorable compared to cylindrical domains.[77]

Chapter 4

Summary and conclusions

In this thesis two aspects of anion exchange membranes relevant for alkaline fuel cells and RedOx flow battery applications were investigated: The alkaline stability of the quaternary ammonium groups and the transport processes inside the membrane.

Experiments on the alkaline stability of quaternary ammonium (QA) groups unexpectedly revealed an exceptional stability of so far neglected 6-membered piperidine-based cations. It is argued that their resistance against elimination and substitution reactions is a consequence of the cyclic structure of the piperidinium. Considerably distorted bond angles and lengths are required in the heterocycle to accommodate the transition states, increasing the activation energy of these processes.

Smaller 5-membered pyrrolidine-based cations were also found to be relatively stable, but their ring-strain is a destabilizing factor. β-protons where shown to be less susceptible to elimination than anticipated, unless they were located on an ethyl group. Aromatic and benzyl based cations did not prove to be suitable functional groups in an alkaline environment, decomposing at very fast rates compared to aliphatic compounds. Electron inducing and withdrawing substituents in vicinity to the cation respectively displayed a stabilizing and destabilizing effect. DABCO based cations, in which the position of the β-protons is constrained into a non anti-periplanar position, were found to be less stable than their non cage-like counterparts, probably due to the destabilizing effect of ring-strain and the electron withdrawing effect of the second nitrogen atom in proximity to the positive charge.

The maximum stability of ammonium cations with alkyl-chain substituents was found between a length of 3 to 6 carbon atoms, relevant to AEMs with spacer-chain attached QAs. Beyond this length, further elongation decreased stability again, probably as a result of micelle formation. Another factor that increases the degradation rate of QAs is a low water concentration, especially at elevated temperatures.

The stability results suggest that it is possible to create AEMs for AFCs with significantly higher alkaline stability than current materials. Such a base stable HEM should not contain benzylic, aromatic or electron-withdrawing groups, especially in vicinity to the QAs. The QAs should be composed of the piperidinium based 6-azonia-spiro-[5.5]undecane, possibly attached to the polymer backbone via spacer-chains with a length between 3-6 carbon atoms. The HEM must be sufficiently hydrated at all times, especially at elevated temperatures, as the degradation rate increases dramatically otherwise.

Investigating the transport processes of ions and water inside an AEM showed that, at sufficient hydration, hydroxide exchange membranes can reach ionic conductivities within a factor of two of proton exchange membranes, analogous to the relative mobility of hydroxide and hydronium in aqueous solution. Lower conductivities are caused by CO_2 contamination and insufficient hydration, which causes reduced dissociation, percolation and a break down of structural diffusion. At low water contents, the strong hydrogen bonds between hydroxide and its water of solvation result in a large hydration shell that comprise a considerable proportion of all present water molecules, resulting in both a measurably lower hydroxide conductivity diffusion coefficient and water diffusion coefficient compared to halide form membranes.

Dissociation is basically complete for the hydroxide and fluoride form membranes at higher water contents, but the same is not the case for the chloride, bromide, iodide and carbonate forms. This was calculated from the ratio of conductivity diffusion coefficients to water diffusion coefficients and furthermore inferred from enthalpies of dissolution and water uptake at a given water activity. For at least the bromide and chloride form membranes, the degree of dissociation is relatively constant over a considerable water content range, up until the membrane dissolves upon which dissociation becomes complete. This behavior suggest the intermediate formation ion condensates consisting of several ions.

Whereas dissociation follows the same trend as the enthalpies of dissolution of the respec-

tive tetramethylammonium halides (within the region where dissociation could be estimated), ionic membrane conductivity does not always follow suit, since ionic mobility has to be taken into account. This leads to the surprising observation that e.g. the hydroxide form membrane (and the fluoride form to a lesser extent) exhibits a higher ionic conductivity than the chloride form at high water contents, but lower conductivities at reduced water content.

Exchanging the type of anion in an AEM changes almost all its properties noticeable, even for very similar ions such as bromide and chloride. This comprises conductivity, dissociation, water uptake as well as the nano-morphology of the membrane. In regard to the nano-morphology, a distinct ordering was observed only for the hydroxide form membrane and not for other, less strongly dissociating ionic forms.

For a hydroxide form membrane, sufficient hydration is required both for good alkaline stability and conductivity to compete with current PEM materials but adequate membranes are within reach. For other ionic membrane forms, further investigations on especially permselectivity are required, specifically for RedOx flow applications.

Chapter 5

Experimental

5.1   Materials

Reinecke's salt, benzyl chloride (99 %), 1,4-diazabicyclo[2.2.2]octane (DABCO, $\geq$99 %), tetramethylammonium chloride (TMA, >98 %), tetramethylammonium iodide (TMAI, 99 %), benzyltrimethylammonium chloride (BTM, 97 %), benzyldodecyldimethylammonium chloride (BDDM, $\geq$99 %), hexadecyltrimethylammonium bromide (HTM, >99 %), dihexadecyldimethylammonium bromide (DHDM, 97 %), 1-benzyl-3-methylimidazolium chloride (BMI, $\geq$97 %), 1-methyl-3-octylimidazolium chloride (MOI, $\geq$97 %), benzyl chloride (99 %), methyl iodide (99 %), 1,2-dimethylimidazole (98 %), piperidine (99 %), pyrrolidine (99 %), 1,5-dibromopentane (97 %), 1,4-dibromobutane (99 %) and bromoethane (98 %) were acquired from Sigma-Aldrich and tetramethylammonium bromide (TMABr, 98 %) from Alfa-Aesar. Diethylether (>99.8 %), ethanol (>99.8 %) and acetonitrile (>99.5 %) were supplied by Roth. All chemicals and solvents were used as received without further purification.

For experiments on ion and water transport as well as morphology a singular batch (M170 011 09) of the commercial non-crosslinked FAA-3 membrane supplied by the FuMaTech GmbH was used to ensure reproducible membrane properties. 0.02 M $AgNO_3$, Na_2SO_4, 1M NaOH and Poly(vinylalcohol), were obtained from Sigma-Aldrich, NH_3I from Merck, H_2SO_4 and NaCl from Roth.

5.2   Decomposition experiments

5.2.1   Experimental setup and procedure

A solution containing a set concentration of NaOH and about 0.1 mol/L QA was filled into a pressure-tight glass flask with Teflon insert ($\approx$ 3.5 ml), closed with a Teflon coated screw cap and stirred while heating to the required temperature (Figure 5.1). At various time intervals the flask was cooled down by tap water flow for 3 min. After cleaning the residual silicone oil and water with paper towels, the flask was shaken a few times and then carefully unscrewed to remove 200 μl of the solution (exact sample mass was determined gravimetrically) using an Eppendorf pipette. While the flask was immediately closed again and re-submerged in into the hot oil bath, the removed sample was stored at 8 °C until a sufficient number of samples (usually > 5) for QA concentration determination using Reinecke's salt (RS) were available.
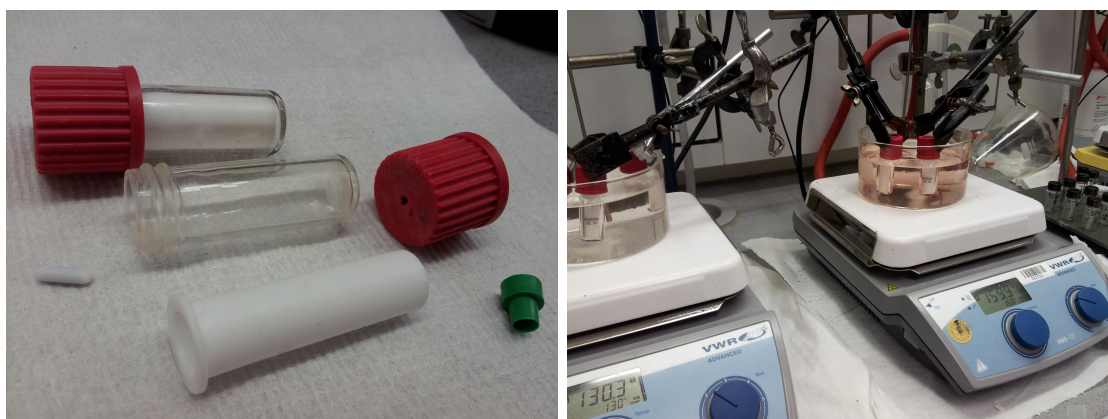
Figure 5.1: The reaction flasks are made of pressure resistant Duran glass with Teflon insert to avoid glass abrasion induced by the caustic solution. Red caps contain Teflon cover plates as well to secure the sealing and protect the plastic. Samples were heated to the desired temperature using a silicon oil bath.

The strongly violet RS solutions decompose over time while forming a green precipitate of probably Cr_2O_3 (Figure 5.2), they were always freshly prepared before use and discarded after 2 h. Therefore a stock of weighted RS amounts was prepared in advance and stored in the dark at 8 °C to allow rapid preparation of 50 - 100 ml RS solution batches with a concentration of 5 mmol/L (e.g 133.9 mg of RS were dissolved in 79.6 g of water). To facilitate the dissolution of the RS, solutions were treated for 3x10 seconds in an ultra-sonic bath.

Figure 5.2: Decay of a 5 mmol/l RS solution in a closed bottle, measured by UV/Vis absorption at 520 nm.

5.2.2   Determination of QA concentration

A 200 μl decomposition sample with a starting concentration of 0.1 mol/l contains a maximum of 0.02 mmol QA. To such a sample, 5 ml of the 5 mmol/l RS solution (containing 0.025 mmol RS) was added, causing all leftover QA to precipitate quantitatively with the RS. The precipitate containing solution was then filtered with a 0.7 μm Chromacol glass syringe filter (sometimes a 1.2 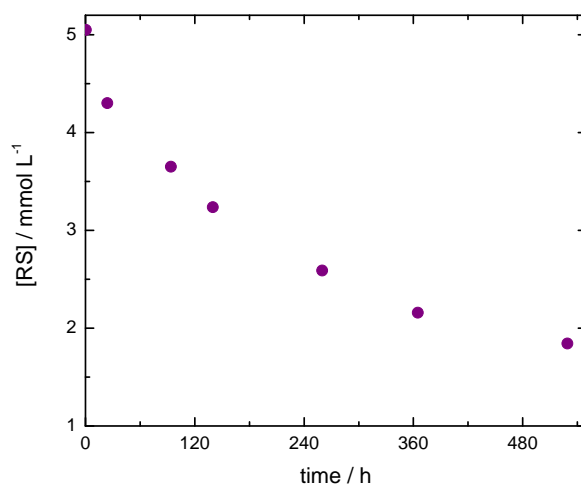μm filter was sufficient, while other samples required a 0.45 μm PTFE filter to reliably remove all particles). A disposable BRAND UV micro cuvette (12.5 x 12.5 x 45 mm, 70 μl, light path 10 mm, center height 8.5 mm) was filled with the filtrate and an absorption spectrum measured using an Uvikon XL UV-Vis Spectrometer (Bio-Tek Intruments) in the range of 350-800 nm with 800 nm chosen as zero absorption reference.

The color of the filtrate gives a visual clue as to the progress of the degradation. The less QA is present in the sample, the stronger the violet hue of the filtrated solution (Figure 5.3). The maximum absorption at 520 nm can be used to quantitatively determine the residual RS concentration. This only requires a RS-calibration curve, with has to be recorded according to the Beer-Lambert law (see Section 2.1.3).

Since the original RS concentration is known and RS precipitates quantitatively with pos-
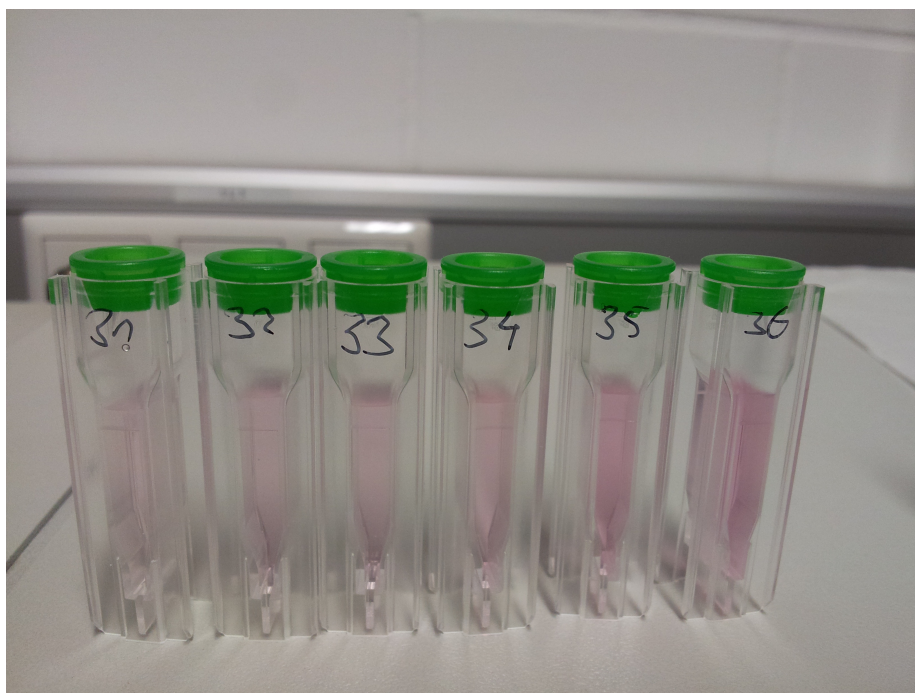
Figure 5.3: UV/Vis cuvettes containing filtrated QA/RS samples. The longer the decomposition reaction takes place, the less QA is left to precipitate with RS, resulting in increasingly violet hues.

itively charged QA, the difference between expected and actual RS concentration can be used to calculate the absolute QA amount in the reaction vessel at the time the sample was taken. Figure 5.4 shows the Excel sheet calculation for a DMP degradation experiment as an example.

	C	F	I	L
sample preparation				
incomple dissolution,				
filtration required.	6 M NaOH	RS [48]	RS [39]	RS [35]
	DMP_01			
M(DMP)	214.14 g/mol	336.43 g/mol	336.43 g/mol	336.43 g/mol
m(DMP)	300 mg	107.5 mg	135.9 mg	138.8 mg
	0.3 g	0.1075 g	0.1359 g	0.1388 g
n(DMP)	0.001401 mol	0.00032 mol	0.0004 mol	0.000412567 mol
mass NaOH (6M)	16.9 g	63.9953 g	80.7671 g	82.5341 g
density NaOH (6M)	1.21 g/ml	0.06396 L	0.08077 L	0.0825341 L
volume NaOH	0.0140 L			
		0.00500 mol/L	0.00500 mol/L	0.00500 mol/L
c(DMP)	0.1003 mol/L	4.996 mmol/L	5.001 mmol/L	4.999 mmol/L

calibration

$[RS] = Abs(0) + Abs * b$

[RS]	Abs(0)	Abs	b
	0.76		9.503

green denotes manually input data
white denotes calculated values
red denotes calculated data used for the diagrams

	#	time (absolute)	m (QA) smpl mg	time at RT min	V (RS) ml	Absorptio 520 nm	V (QA) ml	n (RS)X mol	c (RS)' mmol/L	n (RS)' mol	n (RS)'' = n (QA)'' mol	RT time (total) min	time (relative) h	min	c (QA)'' mol/L	ln c(QA)''	UV/Vis #
	DMP_01		6 M NaOH														
[RS] 48	start	28/03/2014 11:12	240.6	0	5.9110	0.1326	0.1988	2.95E-05	2.02	1.23E-05	1.72E-05	0	0.00	0	0.086	-2.45	63
	1	28/03/2014 13:25	242	5	5.1415	0.0853	0.2000	2.57E-05	1.57	8.39E-06	1.73E-05	0	2.22	133	0.086	-2.45	64
	2	28/03/2014 18:34	242.3	5	5.0078	0.0848	0.2002	2.50E-05	1.57	8.15E-06	1.69E-05	5	7.37	442	0.084	-2.47	65
	3	29/03/2014 09:51	240.0	5	4.9824	0.116	0.1983	2.49E-05	1.86	9.65E-06	1.52E-05	10	22.57	1354	0.077	-2.57	66
	4	29/03/2014 15:39	243.6	5	5.0667	0.1351	0.2013	2.53E-05	2.04	1.08E-05	1.45E-05	15	28.28	1697	0.072	-2.63	67
	5	31/03/2014 08:54	250.0	5	5.0650	0.2158	0.2066	2.53E-05	2.81	1.48E-05	1.05E-05	20	69.45	4167	0.051	-2.98	68
[RS] 39	6	01/04/2014 09:33	255.1	5	5.093	0.2177	0.2108	2.55E-05	2.83	1.50E-05	1.05E-05	25	94.02	5641	0.050	-3.00	74
	7	02/04/2014 09:29	252.6	5	5.0548	0.2982	0.2088	2.53E-05	3.59	1.89E-05	6.37E-06	30	117.87	7072	0.030	-3.49	75
	8	03/04/2014 10:11	247.2	5	5.0110	0.3363	0.2043	2.51E-05	3.96	2.06E-05	4.43E-06	35	142.48	8549	0.022	-3.83	76
	9	04/04/2014 11:00	245.5	5.5	5.0656	0.3268	0.2029	2.53E-05	3.87	2.04E-05	4.96E-06	40	167.22	10033	0.024	-3.71	12
[RS] 35	10	04/04/2014 17:06	245.6		5.0388	0.3233	0.2030	2.52E-05	3.83	2.01E-05	5.10E-06	45.5	173.23	10394	0.025	-3.68	13

Formulas:

- H: D41/1000/C12
- J: (F41/1000)*F14
- K: I21+G41*K21
- L: ((F41+H41)/1000)*(J41/1000)
- L: I41-K41
- M: E40+M40
- N: (C28-C28)*24-(M27/60)
- O: N41*60
- P: L41/(H41/1000)
- Q: LN(P41)

**Figure 5.4:** Excel sheet calculation to determine DMP concentration in a degradation experiment.

5.2.3   Synthesis of quaternary ammonium compounds

These synthetic procedures and NMR-spectra have already been published in an article by the author.[130]

**DMP; N,N-dimethylpiperidinium iodide**

Methyl iodide (1.3 ml, 21 mmol) was added to a mixture of N-methylpiperidine (2.5 ml, 20 mmol) and K_2CO_3(3 g, 22 mmol) in 50 ml EtOH, then the mixture was stirred for 20 h at room temperature. The K_2CO_3 was then removed by filtration and the solvent evaporated using a rotary evaporator. The resulting beige solid was washed with Et_2O and n-Heptane, recrystallized in i-PrOH, then dried *in vacuo* at 80 °C over night. This resulted in 4.97 g of the white product (97 % yield). ^{1}H NMR (300 MHz, D_2O, 25 °C) δ ppm 3.42 (t, 4H), 3.18 (s, 6H), 1.96 (m, 4H), 1.72 (m, 2H).

*Dimethylpiperidinium iodid D2O*
1H
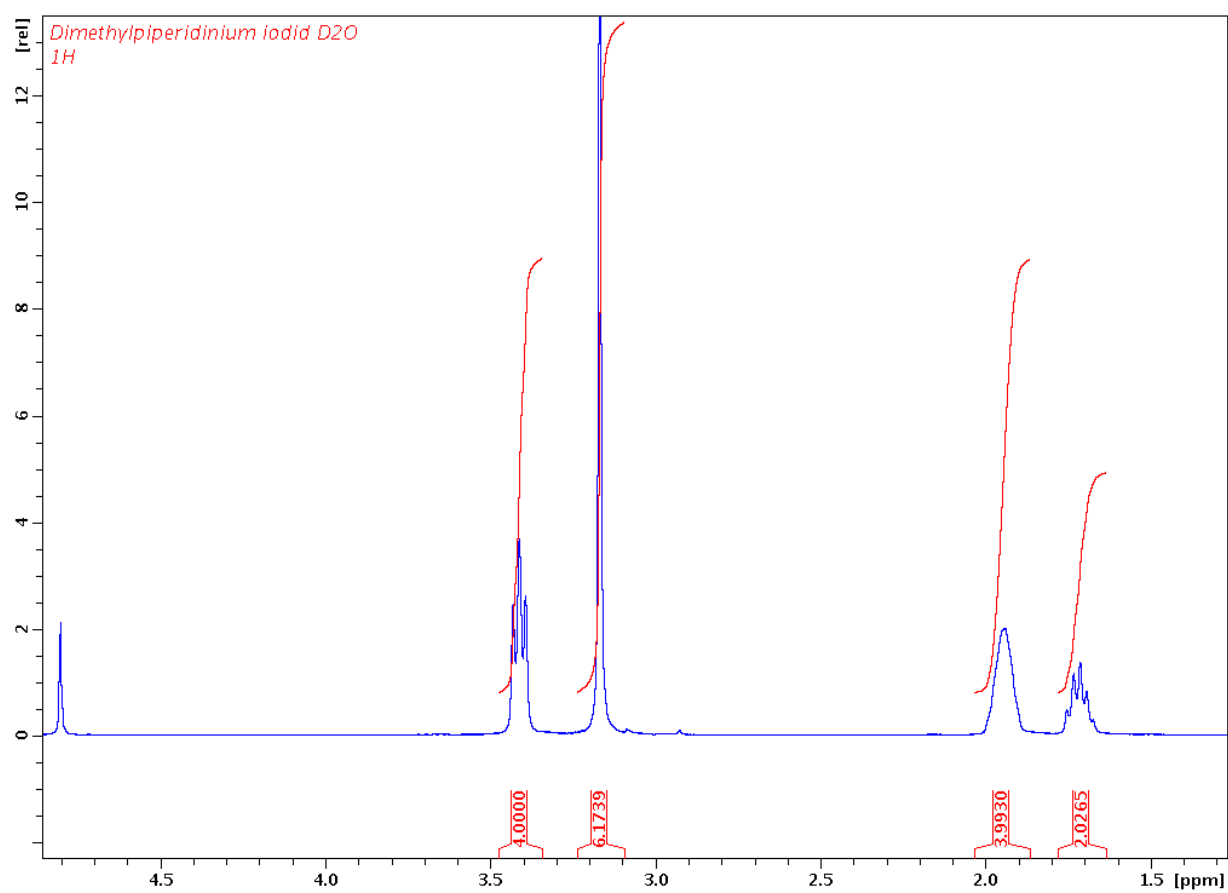
DMPy; N,N-dimethylpyrrolidinium iodide
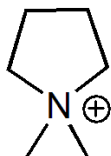
Methyl iodide (1.5 ml, 24 mmol) was added to a mixture of N-Methylpyrrolidine (2 ml, 24 mmol) and K_2CO_3(3.3 g, 24 mmol) in 50 ml EtOH, then the mixture was stirred over night at room temperature. The K_2CO_3 was removed by filtration and the solvent evaporated using a rotary evaporator. The resulting white solid was washed with Et_2O and n-Heptane, then dried *in vacuo* at 80 °C over night. This resulted in 5.46 g of a white solid (99 % yield). ^{1}H NMR (300 MHz, D_2O, 25 °C) δ ppm 3.60 (t, 4H), 3.23 (s, 6H), 2.32 (m, 4H).
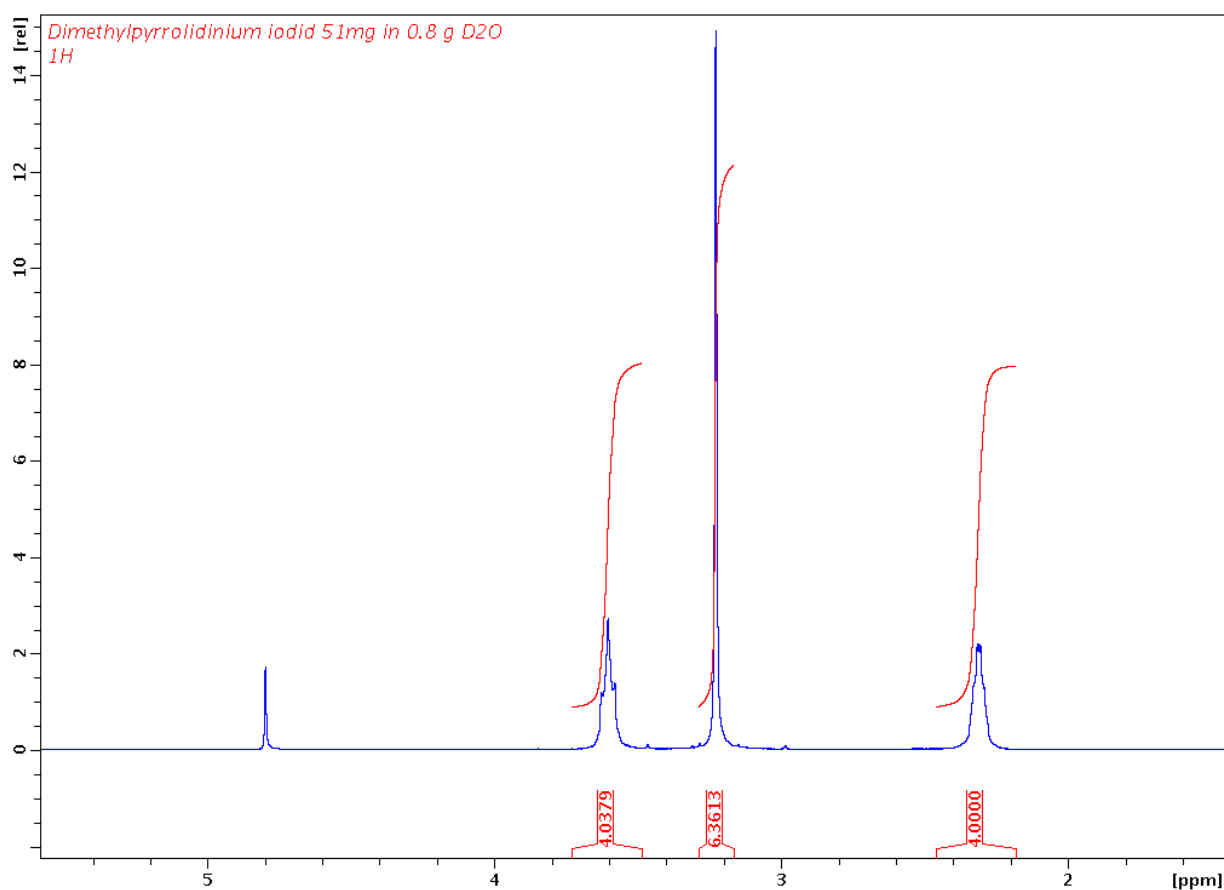
BAABCO; 1-benzyl-4-aza-1-azonium-bicyclo[2.2.2]octane chloride
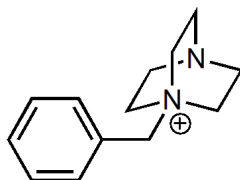
DABCO (1.13 g, 10 mmol) was dissolved in 40 ml of ethanol, then benzyl chloride (1.22 g, 9.7 mmol) dissolved in 10 ml ethanol was added drop-wise while stirring vigorously. The solution was stirred over night and subsequently heated up to 50 °C for 1 hour. The ethanol was then removed using a rotary evaporator (60 °C, 180 mbar), leaving a highly viscous beige-yellow liquid. After cooling down to room temperature again about 20 ml of Et_2O was added and the flask cooled down to 7 °C inside a fridge over night to allow the precipitation of a white crystalline solid. This solid was filtrated (P4 frit, 10-16 μm) and washed with Et_2O and n-heptane. For recrystallization, the solid was dissolved in ethanol. At elevated temperature Et_2O was added until precipitate began to form after which the solution was immediately cooled down to 7 °C and stored for 3 days. The resulting white crystaline solid was filtered and washed again, then dried at 60 °C for 4 hours to afford the product as a white solid (1.94 g, 84 % yield). Comparison of the NMR spectra of the product before and after recrystallization showed no difference and suggests that recrystallization is not required to receive a pure product. ^{1}H NMR (300 MHz, D_2O, 25 °C) δ ppm 7.7-7.47 (m, 5H), 4.49 (s, 2H), 3.44 (t, 2H), 3.16 (t, 2H).

124 mg Benzyl–DABCO+ in 0.56 ml D2O
umkristallisiert
1H
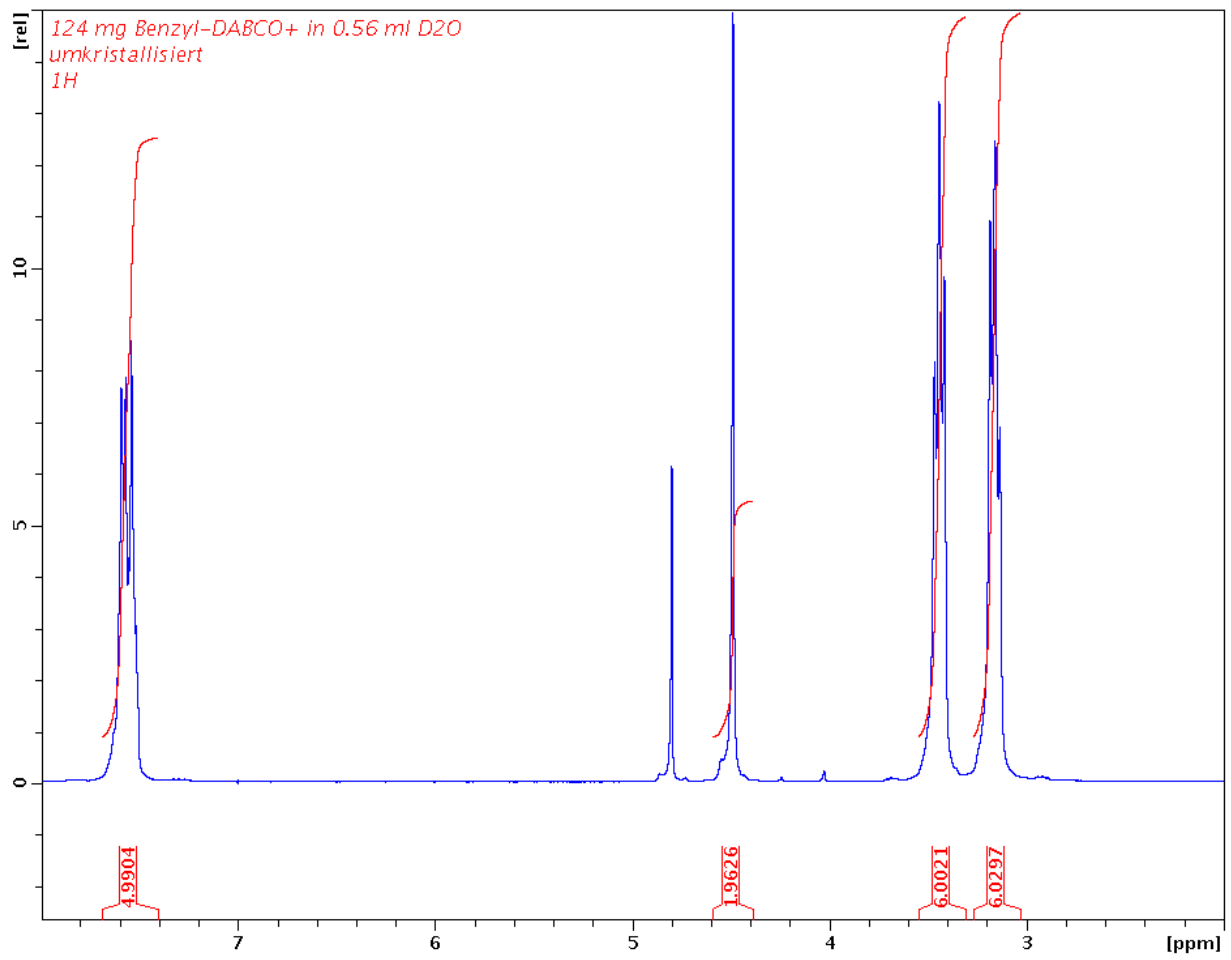
MAABCO; 1-methyl-4-aza-1-azonium-bicyclo[2.2.2]octane chloride
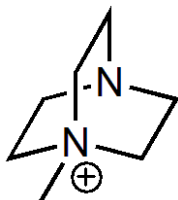
DABCO (1.45 g, 14 mmol), methyl iodide (0.85 ml, 14 mmol) and K_2CO_3 (0.7 g, 15 mmol) in 50 ml EtOH were stirred at RT for 3 days. The mixture was filtrated to remove the K_2CO_3 and the solvent evaporated using a rotary evaporator. The white solid was washed with Et_2O and n-heptane and dried *in vacuo* at $T = 80$ °C over night, resulting in 2.56 g of the white product (78 % yield). ^{1}H NMR (300 MHz, D_2O, 25 °C) δ ppm 3.24 (t, 6H), 3.44 (t, 6H), 3.10 (s, 3H).
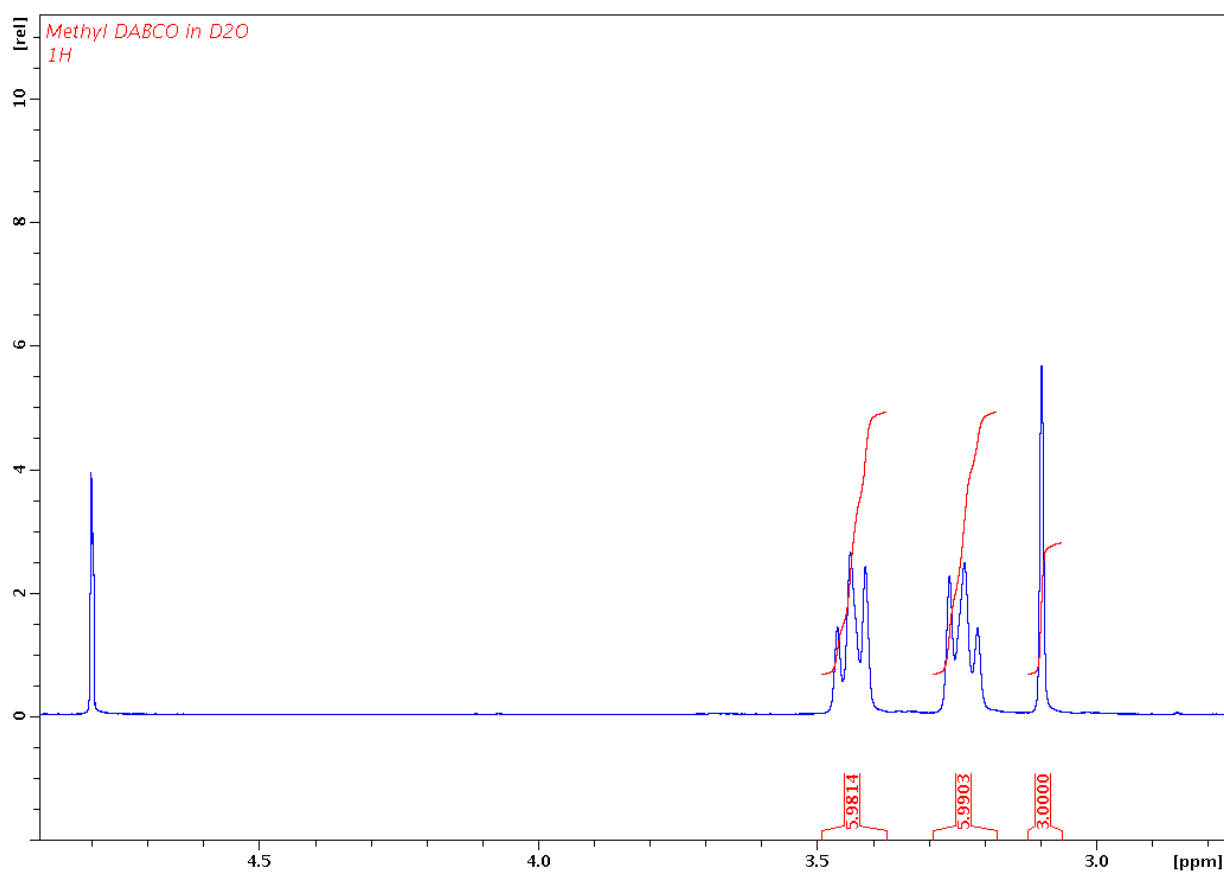
NTM; neopentyltrimethylammonium iodide
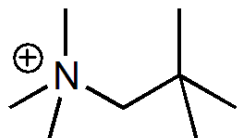
This synthesis is similar to a known literature approach.[131] Methyl iodide (5.1 ml, 82 mmol) was added to a mixture of neopentylamin (3 ml, 25 mmol) and K_2CO_3 (4.7 g) in 50 ml EtOH and stirred for $\approx$ 62 h at room temperature. After removal of K_2CO_3 by filtration the solvent was evaporated via rotary evaporator yielding a slightly yellow solid. This solid was washed with Et_2O and n-Heptane, then dried *in vacuo* at 80 °C over night. This resulted in 4.77 g of a white solid (72 % yield). ^{1}H NMR (300 MHz, D_2O, 25 °C) δ ppm 3.43 (s, H), 3.32 (s, 9H), 1.29 (s, 9H).
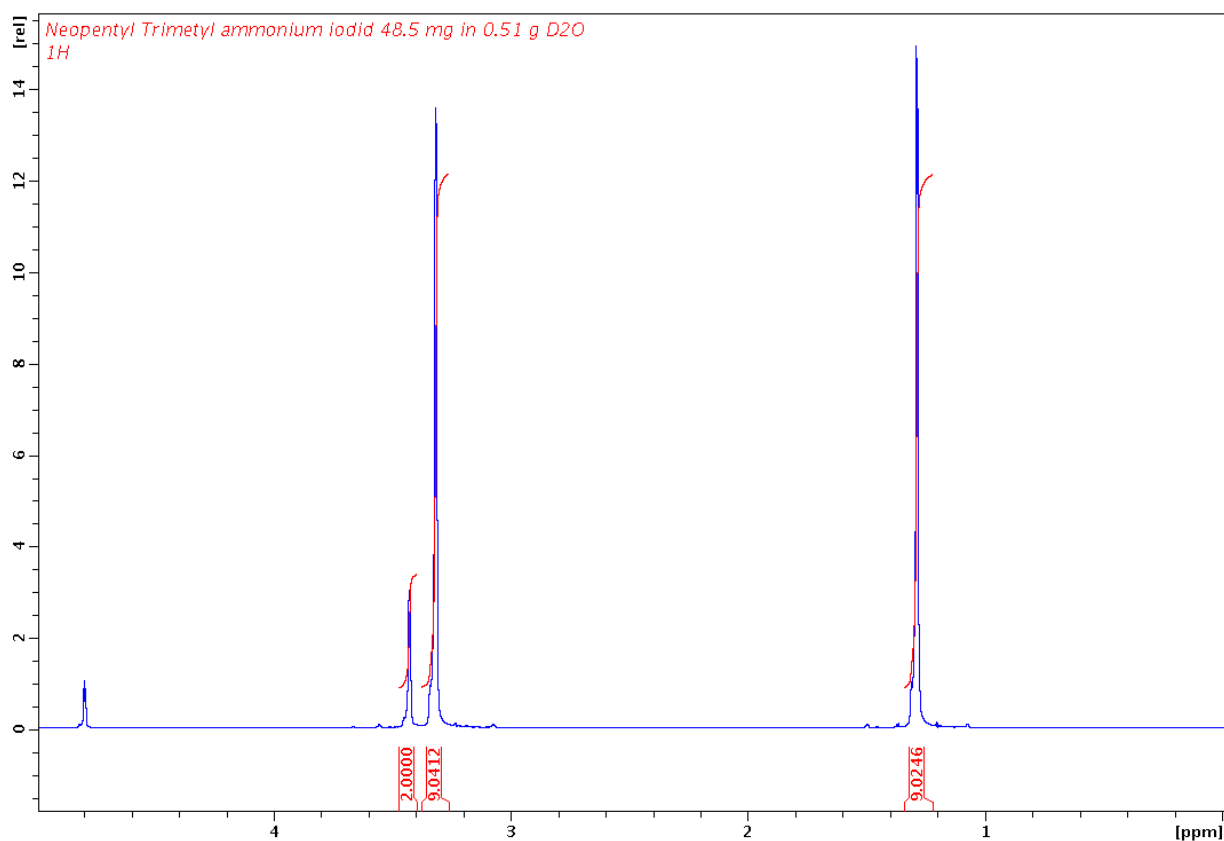
PTM; propyltrimethylammonium bromide
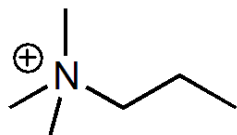
Following a literature approach[132] an aqueous 45 wt% NMe$_3$ solution (3 ml 20 mmol), 1-propylbromide (0.93 ml, 10 mmol) and 2 ml EtOH were stirred in a sealed glass vessel over night at 40 °C. The solution was first pre-dried on a hot plate, then dried *in vacuo* over night resulting in 1.85 g of the white product (100% yield). ^{1}H NMR (300 MHz, D$_2$O, 25 °C) δ ppm 3.32 (m, 2H), 3.15 (s, 9H), 1.84 (m, 2H), 1.01 (t, 3H).
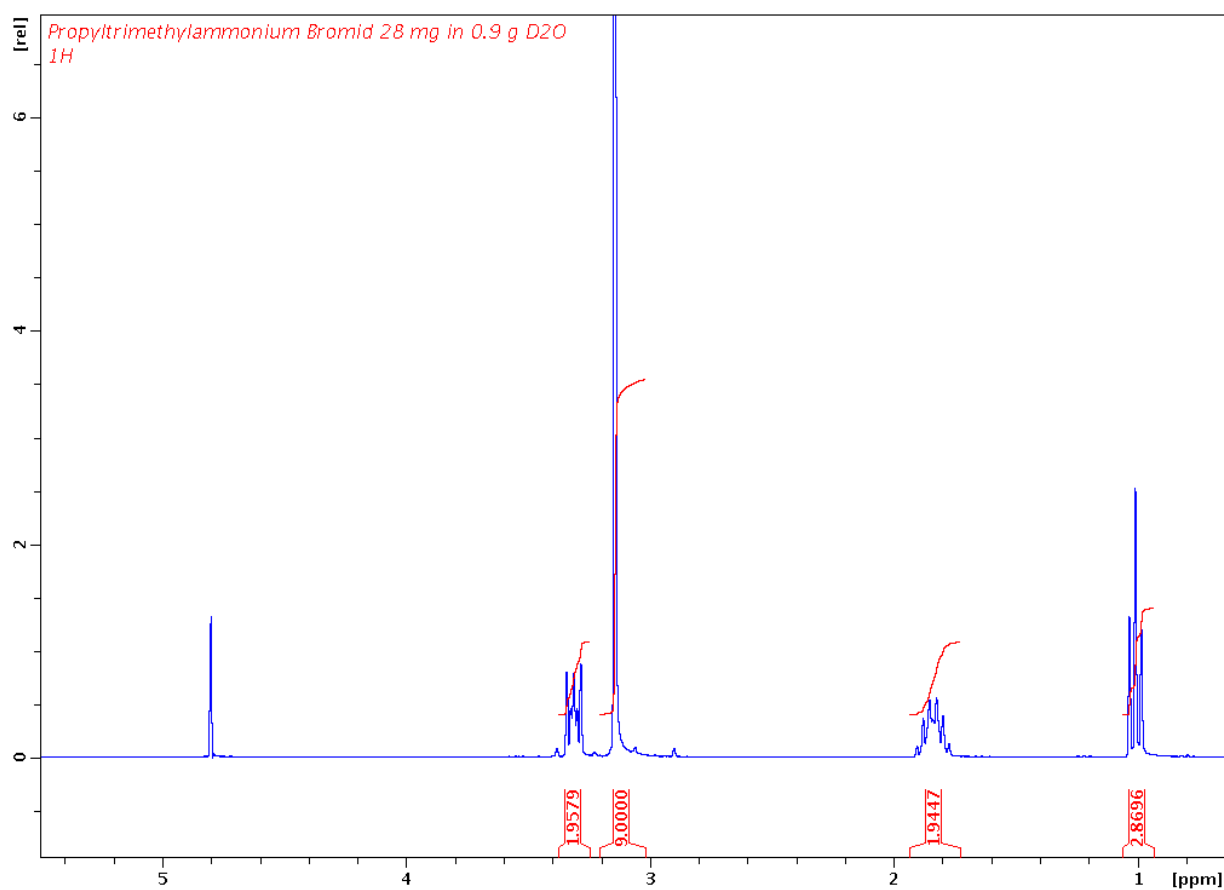
BMP; N-benzyl-N-methylpiperidinium chloride
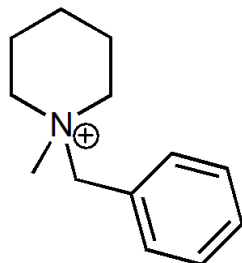
N-methylpiperidine (1.98 g, 20 mmol) and benyzl chloride (2.5 g, 20 mmol) in 50 ml EtOH were stirred over night. The solvent was removed using a rotary evaporator and the resulting white precipitate washed with Et_2O and n-heptane. This gave 2.8 g of the product (60 % yield). ^{1}H NMR (300 MHz, D_2O, 25 °C) δ ppm 7.62 (m, 5H), 4.51 (m, 2H), 3.23 (m, 4H), 2.98 (m, 3H), 1.98 (m, 4H), 1.5-1.9 (m, 2H).
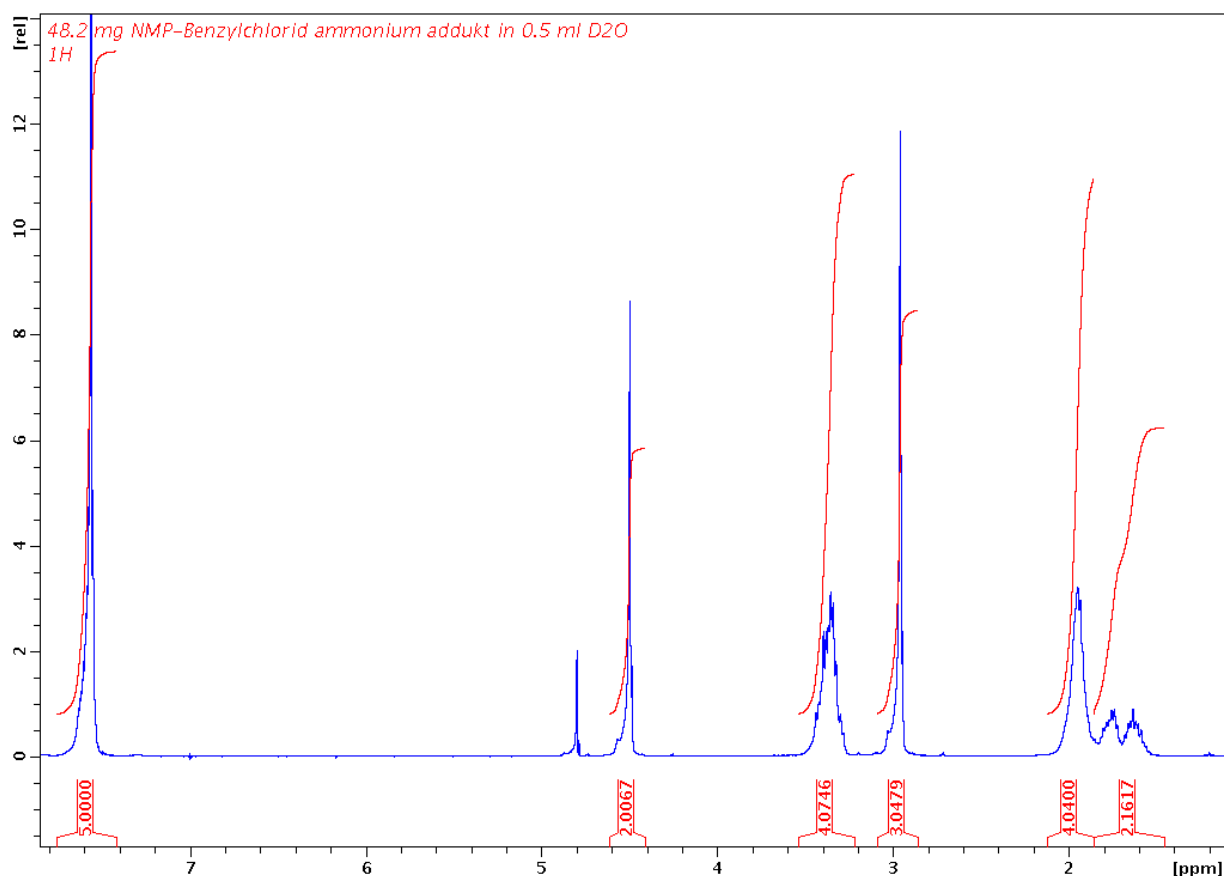
MBTM; (3-methoxybenzyl)-trimethylammonium iodide
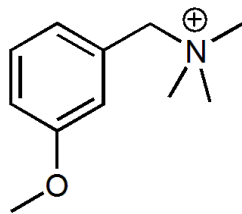
3-Methoxybenzyl-N-dimethylamiun (1.6 ml, 10 mmol), methyl iodide (0.7 ml, 10 mmol) and K_2CO_3(1.6 g, 12 mmol) in 50 ml EtOH were stirred over night. The K_2CO_3 was then removed by filtration and the solvent evaporated using a rotary evaporator. The resulting white solid was washed with Et_2O and n-Heptane, then dried *in vacuo* at 80 °C over night, yielding 2.6 g of the product (76 % yield). ^{1}H NMR (300 MHz, D_2O, 25 °C) δ ppm 7.1-7.6 (m, 4H), 4.55 (s, 2H), 3.90 (s, 3H), 3.22 (s, 9H).
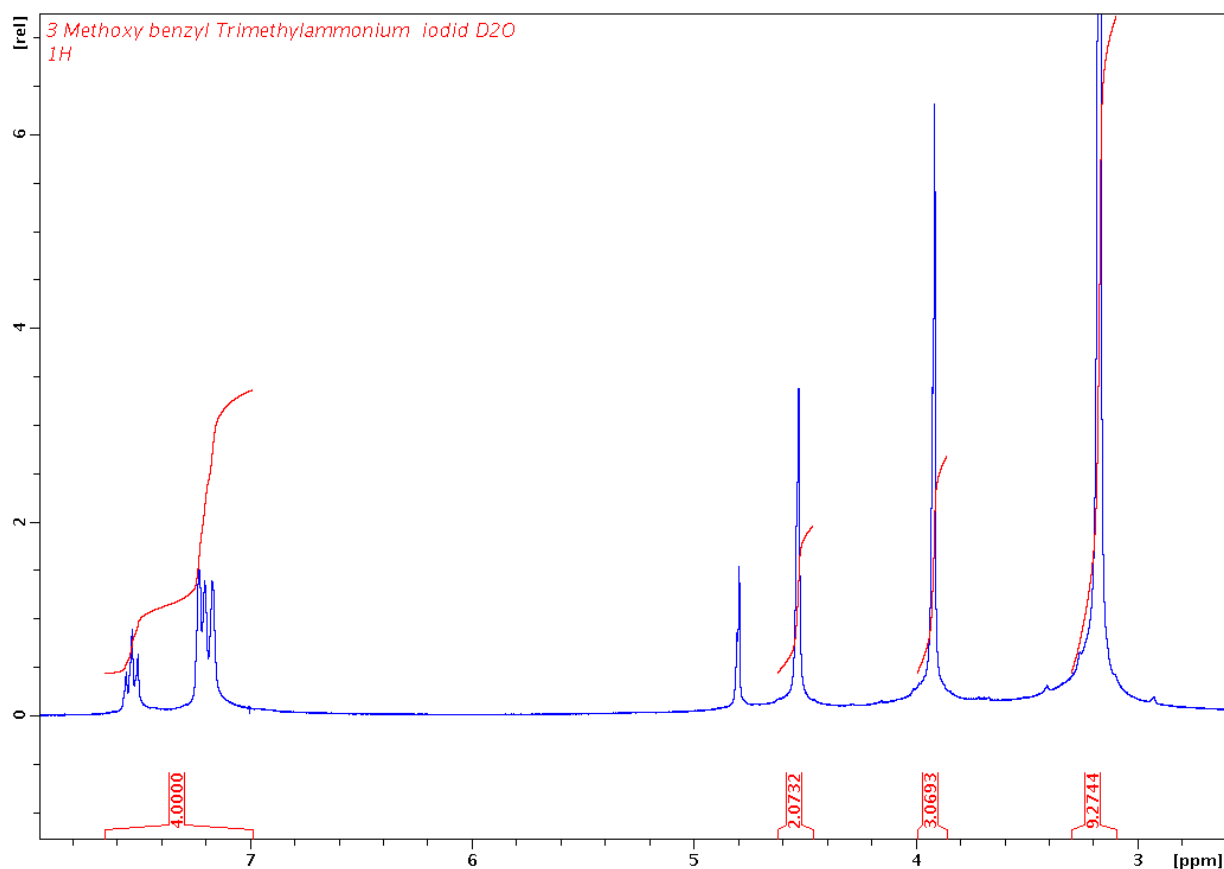
DTG; 1,1-dibenzyl-2,2,3,3-tetramethylguanidinium iodide
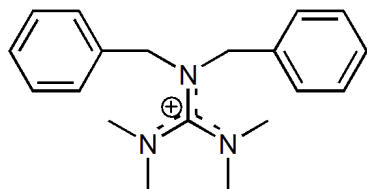
Synthesis and purification of this product was challenging compared to the other compounds. Literature approaches were studied but found to be lacking, the most useful being the one by Santoro.[89,133] Exact amounts will not be given, as several approaches were tried and products unified to give a sufficient yield after excessive purification. A solution of 1,1,2,2 Tetramethylguanidinium and benzyl chloride (1:1 molar ratio) in about 10 times the volume of toluene was heated to 70 °C and stirred until phase separation. A white solid precipitated before phase separation, probably the mono-benzylated guanidinium salt, but dissolved thereafter again in the lower product phase. After rotational evaporation of the solvent, the residual highly viscous clear yellow substance (melting point ≈ 60 ° C) contains the mono and di-benzylated guanidinium salts in a ration of about 1:1 and some benzyl chloride impurity. Increasing the benzyl chloride amount at the start of the reaction did not change this ratio dramatically and addition of K_2CO_3 had no perceptible influence as well. At this point, the solution was combined with similar product compositions from previous approaches. The yellow substance was dissolved in as little i-PrOH as possible, then Et_2O was added until precipitate started to form, and the solution was then cooled to 8 °C. The resulting crystals consisted mainly of the mono-benzylated chloride salt and were washed with Et_2O 3 times. The liquid phases were unified and the solvent evaporated. The solution was again dissolved with as little i-PrOH as possible and crystallization initiated by adding Et_2O and a few mono-benzyl chloride salt seed crystals. After a weekend at 8 °C the white crystals were removed, and the procedure repeated 2 more times. After the fourth cycle, the crystals were basically pure product. After drying *in vacuo* at 80 °C over night this resulted in < 0.2 g of the white product. ^{1}H NMR (300 MHz, D_2O, 25 °C) δ ppm 7.6-7.2 (m, 10H), 4.45-3.95 (m, 4H), 3.05-2.90 (m, 12H).

DTG in D2O, synthese nach drittem Umkristallisieren und auskristallisieren der uebriger Loesung.
1H
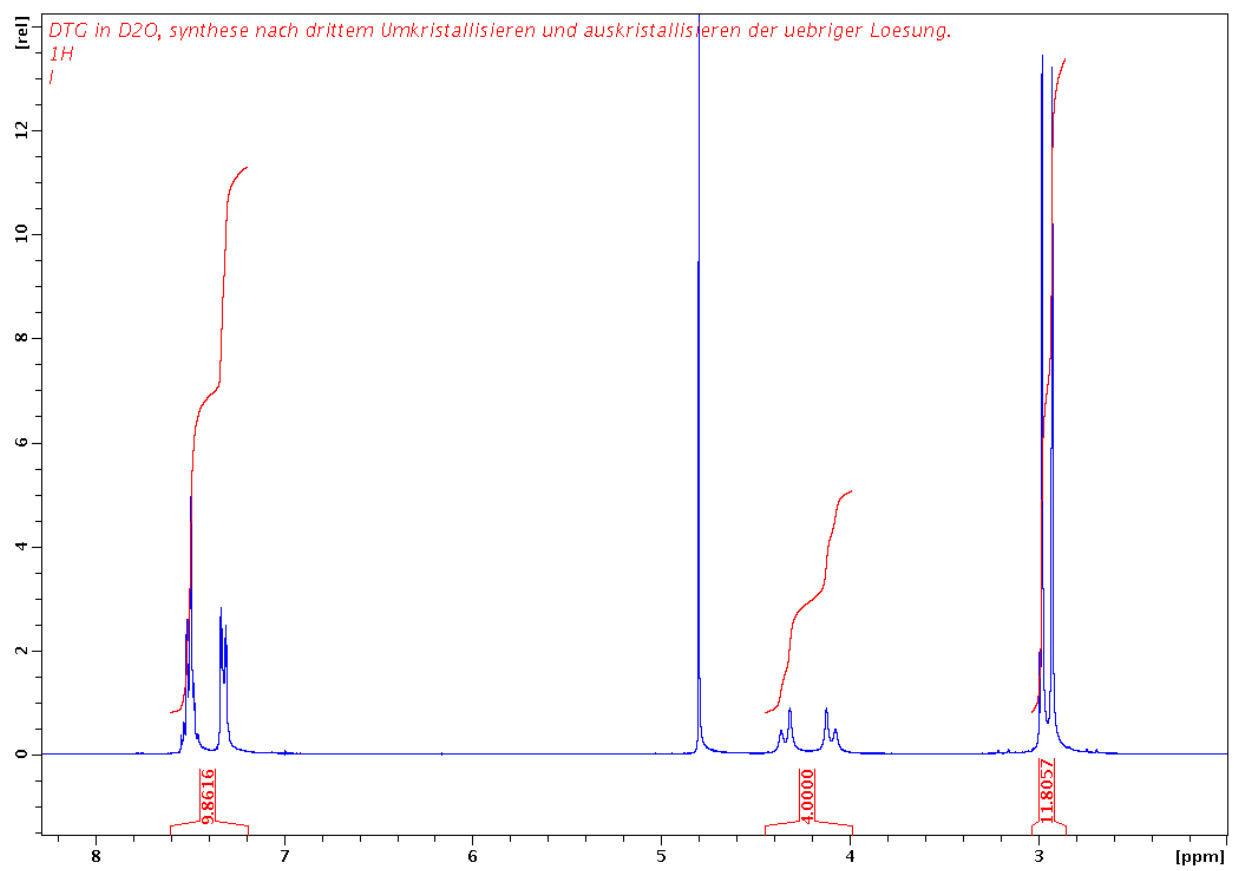
ETM; ethyltrimethylammonium bromide
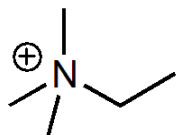
A solution of aqueous 45 wt% NMe_3 (3 ml, 20 mmol), Ethylbromide (0.72 ml, 10 mmol) and EtOH (1.8 ml) was stirred for 24 h at 40 °C. The solution was then dried on a hotplate for 4 h, followed by over night drying *in vacuo* at 80 °C. This resulted in 1.48 g of the white product (91 % yield). ^{1}H NMR (300 MHz, D_2O, 25 °C) δ ppm 3.4 (q, 2H), 3.18 (s, 9H), 1.41 (t, 3H).
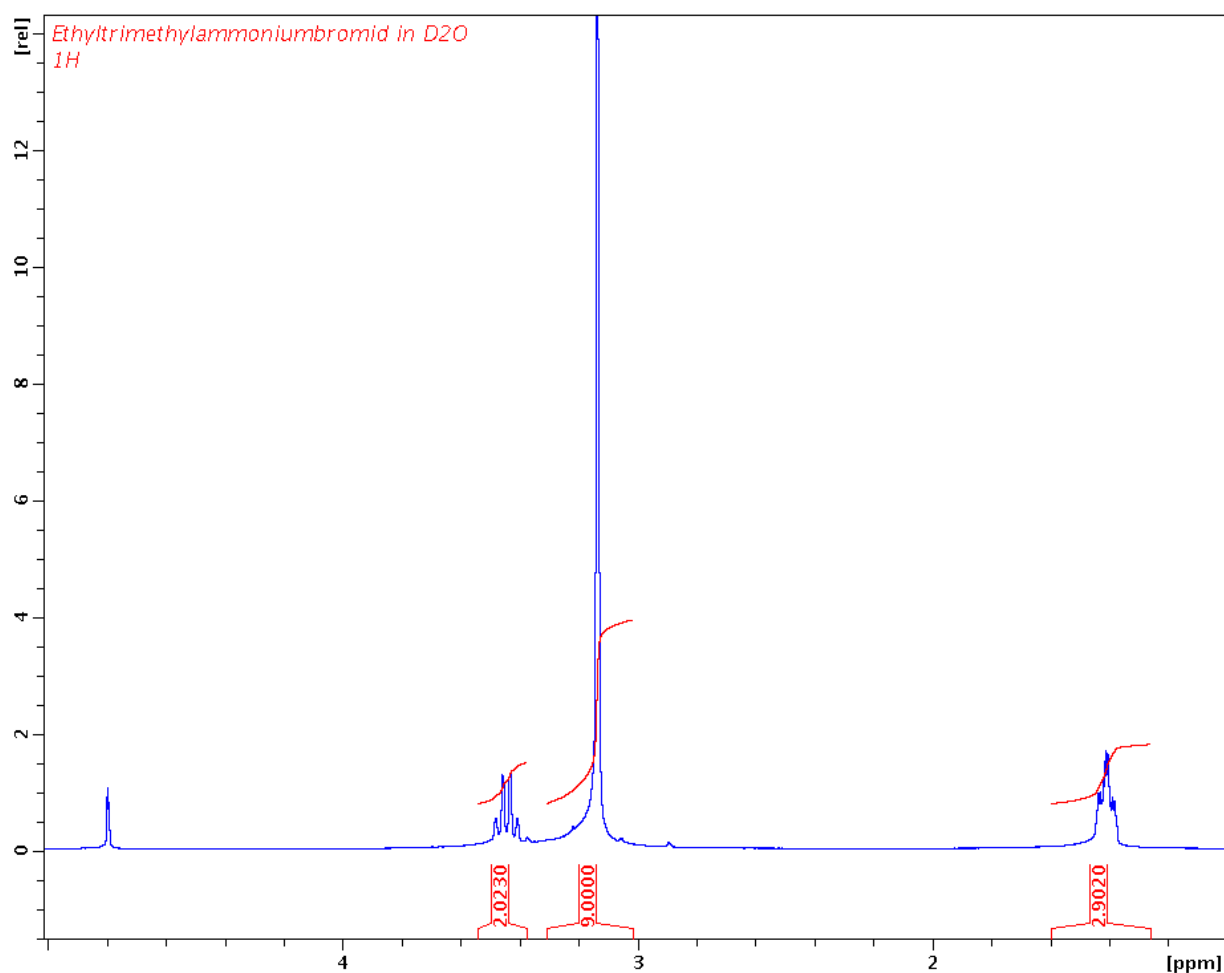
TMI; 1,2,3-trimethylimidazolium iodide
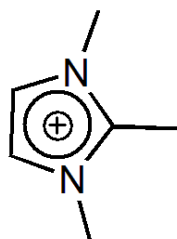
A solution of 1,2-dimehtylimidazole (1.11 g, 11.6 mmol) and methyl iodide (0.72 ml, 11.5 mmol) in 45 ml EtOH was stirred for 12 h at RT during which a yellow precipitate formed. The solvent was evaporated using a rotary evaporator and the precipitate washed several times with Et$_2$O and n-heptan. After drying *in vacuo* at 80 °C this resulted in 0.92 g of the white product (33 % yield). ^{1}H NMR (300 MHz, D$_2$O, 25 °C) δ ppm 7.28 (s, 2H), 3.80 (s, 6H), 2.60 (s, 3H).
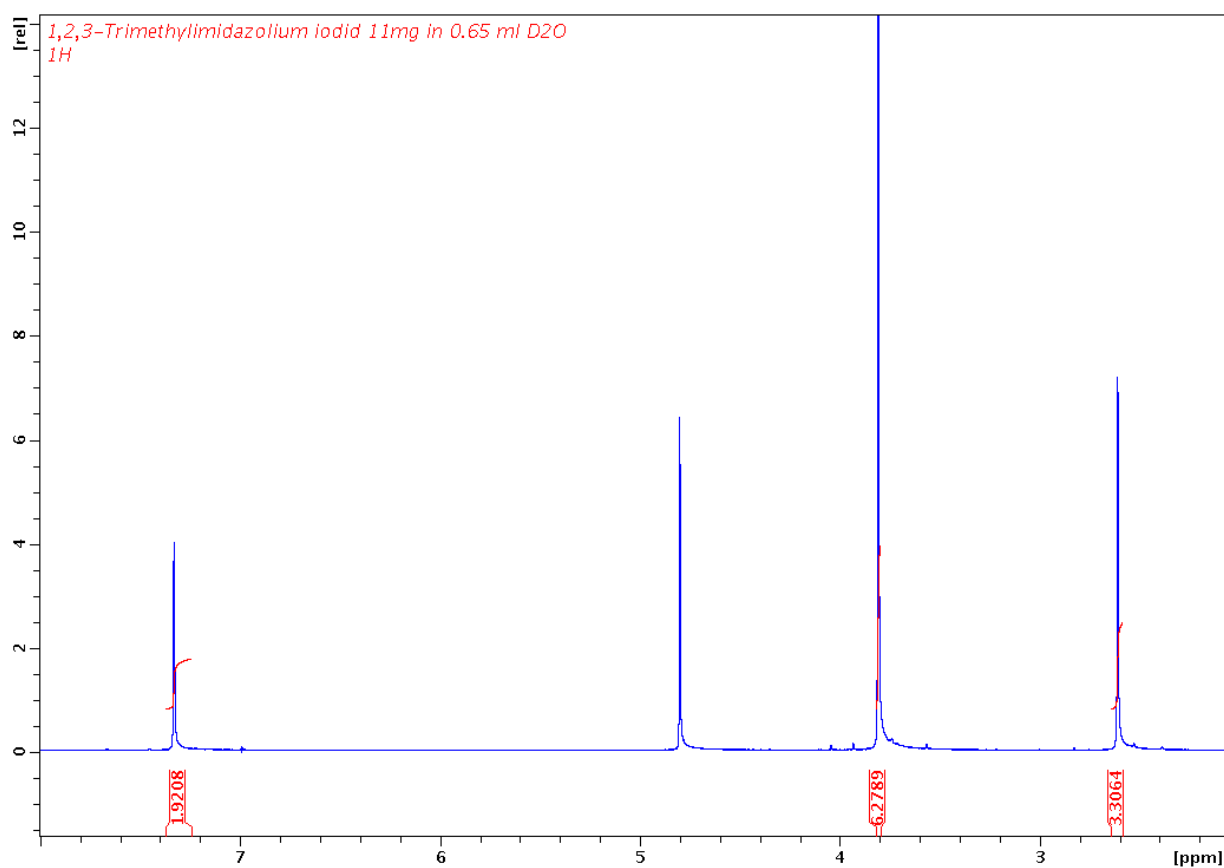
ASU; 6-azonia-spiro-[5.5]undecane bromide
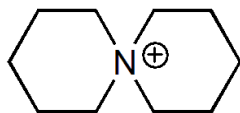
In a three-neck flask a mixture of 1,5-dibromopentane (5.75 g, 25 mmol) and K_2CO_3 (4.2 g, 30 mmol) in 50 ml acetonitrile was heated to reflux. Piperidine (2.14 g, 25 mmol) in 10 ml acetonitrile was added drop-wise via dropping funnel under reflux and the total mixture refluxed over night. Afterwards the solvent was evaporated using a rotary evaporator. EtOH was added to the residual solid and the mixture filtered to remove the K_2CO_3. The solvent was partially evaporated to create an almost saturated solution to which Et_2O was added to precipitate a snow-white solid. This solid was filtered and washed with Et_2O, n-heptane and Et_2O again (the product appears to be slightly soluble in n-heptane). The solid was dried *in vacuo* at 80 °C over night to give 4.49 g of the product (77 % yield). ^{1}H NMR (300 MHz, D_2O, 25 °C) δ ppm 3.48 (t, 8H), 1.91 (m, 8H), 1.75 (m, 4H).
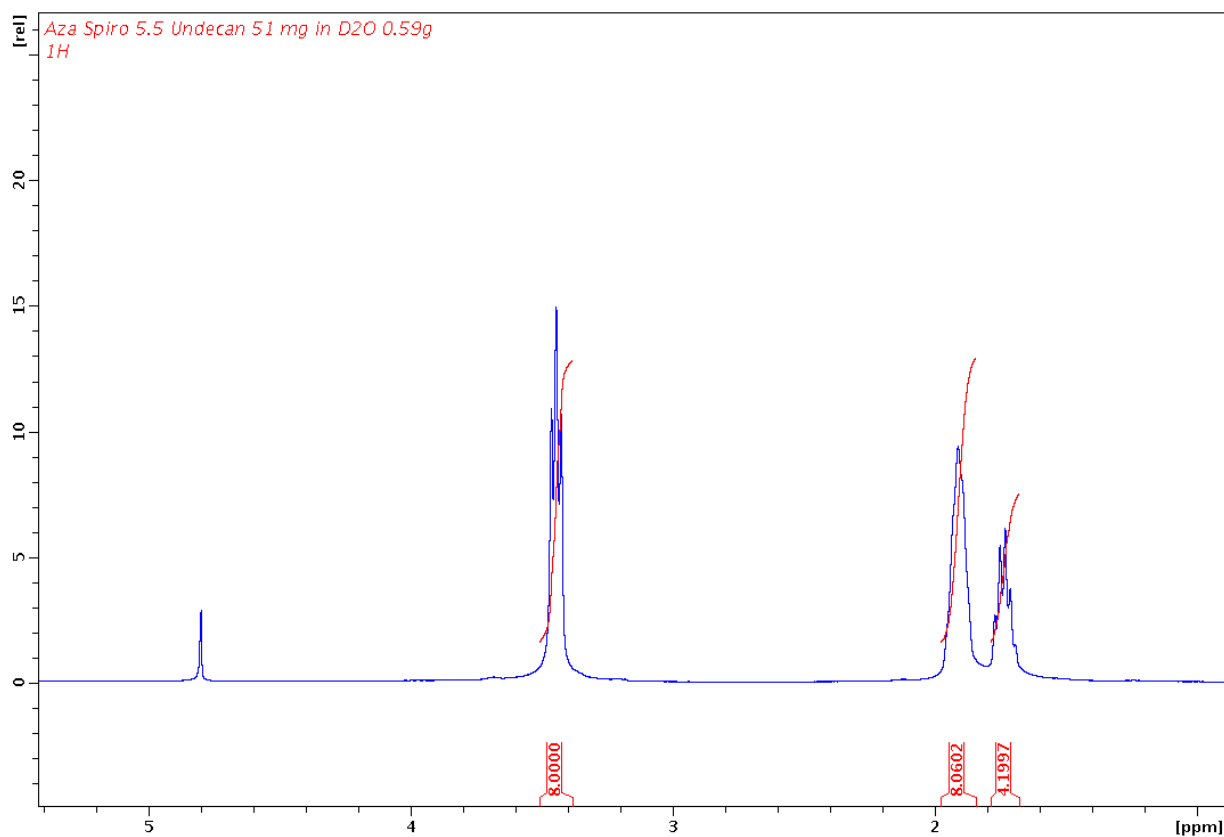
ASN; 5-azonia-spiro-[4.4]nonane bromide
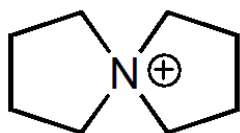
A mixture of 1,4-dibromobutane (2.19 ml, 4g, 19 mmol) in 30 ml acetonitrile with K_2CO_3 (2.7 g, 20 mmol) was prepared. Pyrrolidine (1.82 ml, 1.58 g, 19 mmol) in 10 ml acetonitrile was added drop-wise at room temperature and the solution refluxed for 24 h. The solvent was removed using a rotary evaporator, then EtOH was added to dissolve the product. The K_2CO_3 was filtered of and washed with EtOH several times. The solvent of the filtrate was evaporated, then dissolved in a minimum amount of EtOH. An excess of Et_2O was added until no further precipitate formed. The precipitate was filtered of and washed with Et_2O several times. After drying the precipitate *in vacuo* at 80 °C for 4 h, 3.56 g of the white product (93 % yield) was obtained. ^{1}H NMR (300 MHz, D_2O, 25 °C) δ ppm 3.59 (t, 8H), 2.27 (m, 8H).
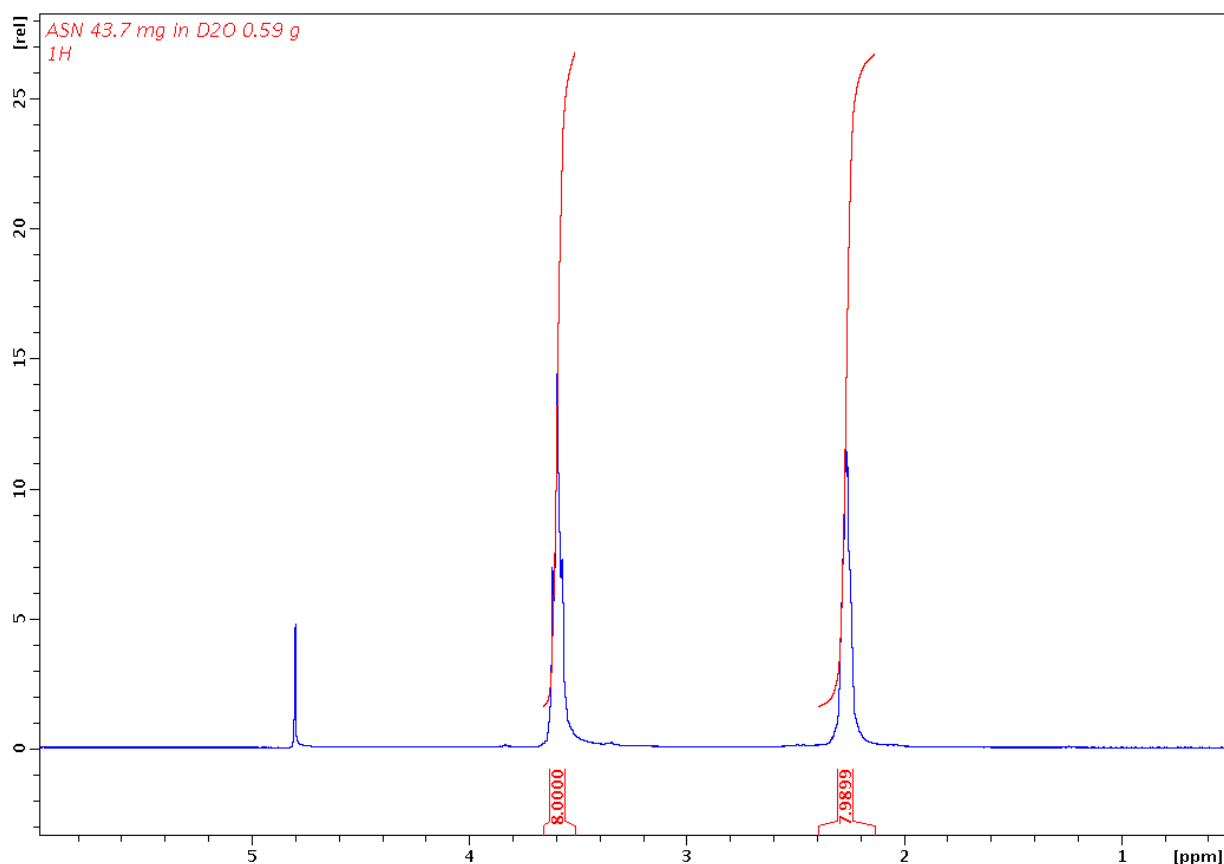
5.3   Transport experiments

5.3.1   Membrane preparation

The membranes were received in the bromide form and washed with deionized water until conductivity of the washing water remained constant, which was measured with a Hanna Instruments HI 98308 Pure Water Tester (PWT). To convert the membrane into anionic forms other than bromide, the washed membranes were submerged in 1 M salt solutions containing the required anion (e.g. NaCl, NH_4I, NaF, NaF, NaOH). The salt solution was exchanged at least three times over the course of 48 hours to ensure complete ion exchange. Subsequently, membranes were washed again as outlined above and stored in liquid water in closed glass bottles at RT until use. Conversion to the hydroxide form was always done in a CO_2-free atmosphere (see below). If it was necessary to maximize water uptake of the membranes, they were submerged in water at elevated temperature. Temperatures approaching 100 °C were achieved in an autoclave to avoid constant water refilling. For extremely high water volume fractions, membrane solutions were created by homogenization using an IKA T10 Basic Ultra-Turrax after swelling in an autoclave.

5.3.2   Membrane conductivity

A membrane was punched out on a Teflon board to create a column from round layers with a 4 mm diameter and a length of 4-10 mm that was placed in a glass cylinder. Both ends were capped with flat gold plates and pressed tightly together with a vise to create a cohesive stack without cracks or irregularities (Figure 5.5). The sample was then placed in a closed double walled glass cylinder with a temperature controlling liquid flow-through, contacted on both sides with stainless steel electrodes. A constant pressure was applied via three bolt nuts to ensure good contact. Membrane solutions were measured inside a U-cell with platinum electrodes, the temperature being controlled via a liquid bath.

Impedance spectra were recorded with an HP 4284A Precision impedance spectrometer in the frequency range of 20 Hz - 1 MHz (25 - 65 °C). Temperature measurements were calibrated using a Pt100 resistance thermometer. Where necessary, the spectrum was fitted using simple equivalent circuits to determine the resistance of the membrane. Weight,

Figure 5.5: A formed membrane stack with gold electrodes on both ends. The vise compresses the stack to ensure cohesion.

diameter and height of the stack were determined before and after each conductivity measurement run (consisting of a temperature ramp up and ramp down) to ensure water evaporation was not excessive. To determine dry weight, membranes were dried *in vacuo* at 50 °C for 24 h. Hydroxide form membranes were converted to chloride before drying to avoid decomposition.

5.3.3   Pulsed field gradient nuclear magnetic resonance (PFG-NMR)

Similar to the procedure in Section 5.3.2 a membrane stack was prepared, this time inside a 4 cm long cut NMR glass tube (5 mm) open on both ends. To create an air-tight seal around the sample, Teflon stoppers (hydrocarbon for ^{19}F nuclei) were tightly inserted from both sides (Figure 5.6).

To reduce the water content of the membrane after a measurement, the stack was removed from the glass and dried in air for a certain amount of time. Hydroxide form membrane samples were prepared and dried in a CO_2-free atmosphere. The ends of the glass tube were slightly enlarged to facilitate the insertion of the Teflon stoppers. Careful movements and slow rotation was required to insert the stoppers to avoid cracks in the glass. Furthermore, the same stoppers could not be used more than a couple of times, as the Teflon would soften and deform with time, eventually resulting inadequate sealing of the sample. The thicker part of the Teflon stoppers was the same diameter as a 5 mm NMR-tube to enable the use of a normal NMR-spinner. The sample setup was inserted into a Bruker Avance III 400 MHz NMR spectrometer with a Diff60 probe head. Stimulated Echo (STE) and Spin Echo
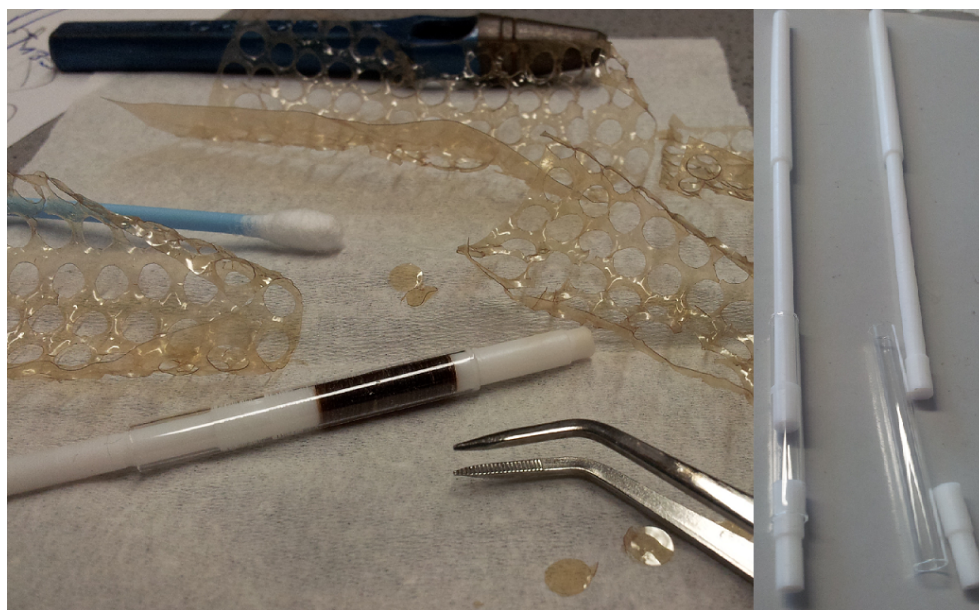
Figure 5.6: A prepared NMR-sample with Teflon stoppers and cut NMR-glass tubes.

(SE) experiments were both used to determine diffusion coefficients. Diffusion time was 10 ms with gradient strengths varying from 30 to 1600 G/cm depending on measurement requirements with 16 gradient steps per experiment. Effective gradient pulse duration was 1 ms with a 10 μs duration of the 90° pulses. Temperature was calibrated using a Pt100 resistance thermometer. To determine dry weight, membranes were dried *in vacuo* at 50 °C for 24 h. Hydroxide form membranes were converted to chloride before drying to avoid decomposition.

5.3.4   Small angle X-ray scattering (SAXS)

8-12 membrane layers were stacked inside a brass vessel, which was made gas tight by rubber seals and Mylar window sheets (Figure 5.7). At BM 26B of the European Synchrotron Radiation Facility (ESRF) in Grenoble (France) the experiments were conducted with a 2D multiwire gas-filled detector (512x512 pixel array). The q-scale was calibrated with the diffracted peak positions of a standard silver behenate powder. Each sample was exposed for about 60 s at a wavelength of 1.54 Å. Background scattering was corrected and the data transformed by azimuthal angle integration into one-dimensional plots. To determine dry weight, membranes were dried *in vacuo* at 50 °C for 24 h. Hydroxide form membranes were converted to chloride before drying to avoid decomposition.
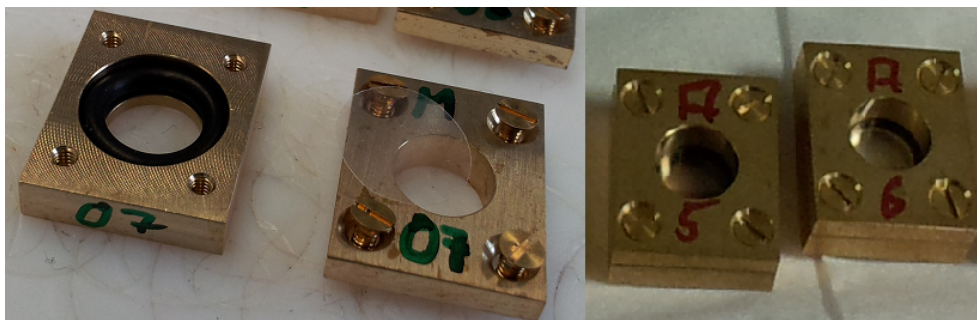
Figure 5.7: Brass SAXS cells open (left) and closed with membrane sample (right).

The following is a description of the used fitting formula for the determination of the ionomer peak of the SAXS patterns with two Gaussian functions as shown in Section 3.2.4.

$$I_1 = y_1 + G_1 \cdot \frac{1}{\sigma_1 \cdot \sqrt{2 \cdot \pi}} \cdot e^{-\frac{q-\mu_1}{\sigma_1^2}}$$

$$I_2 = y_2 + G_2 \cdot \frac{1}{\sigma_2 \cdot \sqrt{2 \cdot \pi}} \cdot e^{-\frac{q-\mu_2}{\sigma_2^2}}$$

where I_n is the signal intensity, σ_n the standard deviation of the curve, q the correlation length, μ_n the position of the ionomer maximum on the x axis (i.e. median), y_n a fitting parameter that adds y-axis intensity and G_n a fitting parameter to multiply the intensity. Addition of both functions gives the total fitting function.

$$I_{total} = I_1 + I_2$$

5.3.5   Hydration behavior

Membrane water content was determined by weighting in the hydrated state before and after each measurement and again after drying *in vaccuo* at 50 °C for 24 h to determine the dry weight. The hydroxide form was converted to the chloride form, using the procedures outlined above, before drying to avoid decomposition.

Water uptake in water at varying temperatures was determined by submerging the membranes at the specified temperature in water for 2 h, then rapidly cooling them with cold water. Before weighing, the samples were quickly dried with a paper towel to remove excess water.

Water uptake at varying temperatures and relative humidities was measured with thermo-gravimetric analysis (TGA) setup containing a magnetic scale, physically decoupled from the experimental conditions and separate temperature controlled regions for the water containing reservoir (T_W) and the crucible containing the sample (T_S). As shown in Figure 5.8 this allows the gas flow from below to set a desired relative humidity.

The number of water molecules per functional group i.e. the hydration number λ was calculated with the formula

$$\lambda = \frac{m_{wet} - m_{dry}}{\text{IEC} \cdot m_{dry} \cdot \text{M}_{\text{H}_2\text{O}}}$$

were m_{wet} and m_{dry} are the weight of the membrane in the wet and dry state respectively, IEC is the ion exchange capacity in mol/g and $\text{M}_{\text{H}_2\text{O}}$ the molar mass of water.

5.3.6   Ion exchange capacity

Chloride form membranes were submerged in a 1 M Na_2SO_4 solution which was exchanged two times. Afterwards the membranes were washed with deionized water and all solutions combined. Then 5 ml of a 0.2 wt% poly(vinylalcohol) solution and 5 drops of 2 M H_2SO_4 were added. Potentiometric titration with a silver and a calomel electrode and a 0.02 M $AgNO_3$ solution then made it possible to determine the amount of chloride in the sample. Before drying and weighing the membranes were converted to the chloride form again, which gave an IEC of 2.1 mmol/g. The IECs of the other ionic forms was calculated base on this value. Since the amount of chloride n_{Cl^-} in a given membrane sample is equal to the amount of any other anion n_{X^-} in the same sample after complete ion exchange

$$n_{\text{Cl}^-} = n_{\text{X}^-}$$

the total mass of all chloride atoms is

$$m_{\text{Cl}^-} = n_{\text{Cl}^-} \cdot M_{\text{Cl}^-}$$

and the total mass of any other anion is consequently

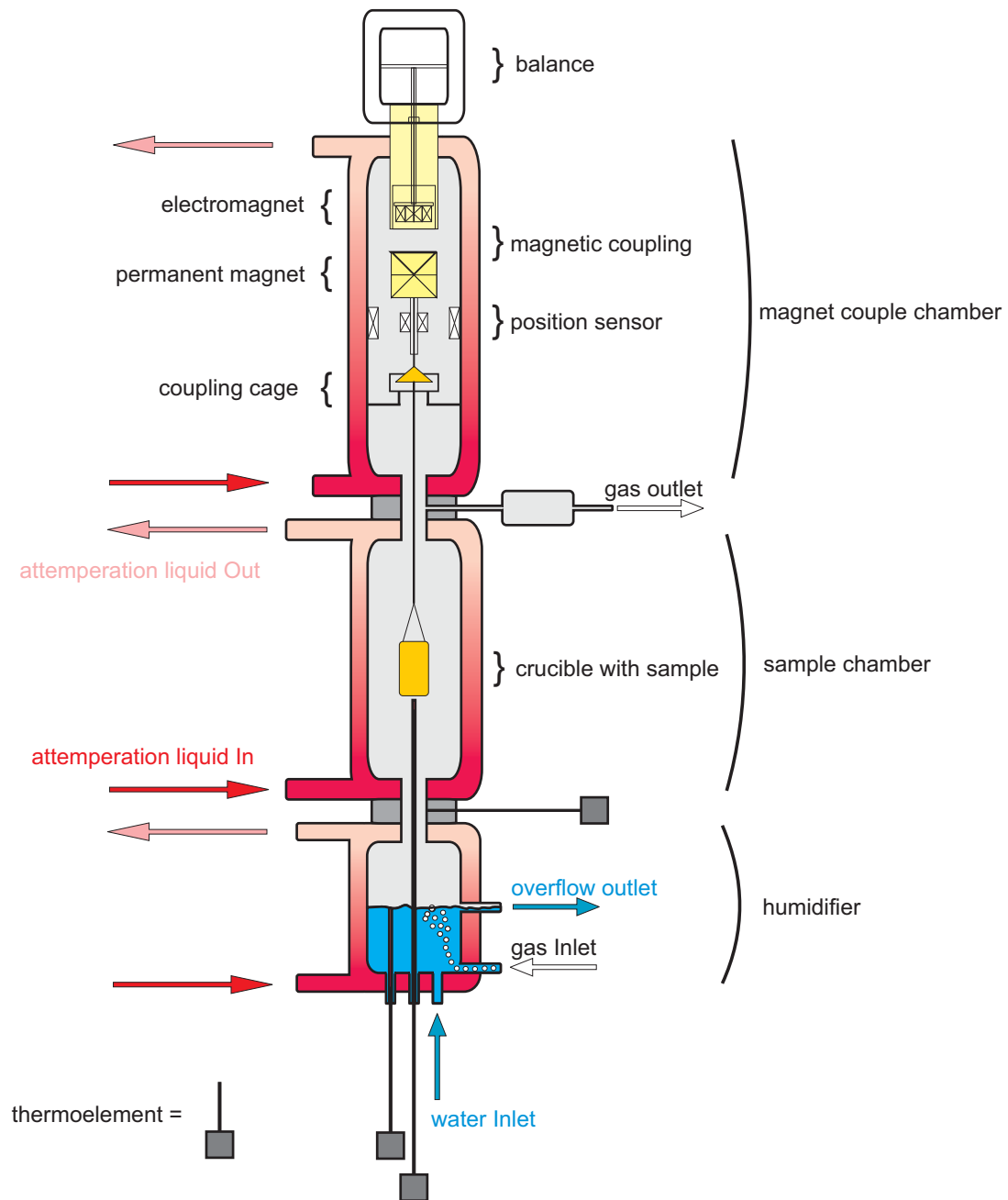$$m_{\text{X}^-} = n_{\text{Cl}^-} \cdot M_{\text{X}^-}$$

Figure 5.8: This TGA-sketch shows the magnetically coupled balance to which the sample crucible is attached and the various temperature controlled regions through which relative humidity and temperature at the sample can be controlled.

with which the dry membrane weight of any ion form membrane $m_{dry\mathrm{X}^-}$

$$m_{dry\mathrm{X}^-} = m_{dry\mathrm{Cl}^-} - m_{\mathrm{Cl}^-} + m_{\mathrm{X}^-}$$

can be calculated. Conversion of hydroxide ions to carbonate in a membrane over time was determined by Warder titration using a Metrohm Titrino plus 877.

5.3.7   Membrane density

A Micromeritics ACCUPyc1330 pycnometer with Helium gas was used to determine the density of the dried membranes by first drying the membranes in various anionic forms for 24 h at 50 °C *in vacuo* inside the pycnometer crucible and instantly closing it after pressurization before inserting it into the pycnometer.

5.3.8   Custom glove box

To avoid conversion of the hydroxide in a HEM to carbonate by ambient CO_2, a custom glove box filled with a humidified Argon atmosphere was constructed, in which HEMs could be prepared and handled (Figure 5.9). This allowed measurements of pure hydroxide form membranes at varying water contents for the first time without the necessity to keep the samples submerged in water.

The main components are Plexiglas sheets, the top sheet containing a removable partition for insertion of larger equipment and an air lock for smaller parts in addition to a spring driven overpressure valve. The weight of the top Plexiglas sheet would cause the top to sag and cause leakage, which required it to be screwed on at the rim, while the other sheets could simply be glued together. To the right side a metal plate was installed with customizable air-tight flanges for various connections (electrodes, heat transfer fluid, thermoelements, power and atmosphere purification system) to the outside of the box. Two gas-tight gloves were attached two the front side for sample manipulation. The Argon atmosphere was constantly circulated via a KNF Neuberger miniport diaphragm pump through a soda lime column for CO_2 removal. An optical infrared sensor was employed to ensure CO_2 concentration remained below 1 ppm. Converting the membrane into the

hydroxide form and subsequent washing, sample preparation and impedance spectroscopy measurement of hydroxide form membranes was conducted exclusively inside the glove box. HEM NMR samples could be prepared inside the glove box as well, but had to be transferred to the outside NMR spectrometer after the sample vessels were sealed. HEM-NMR samples were returned to the glove box for gradual dehydration.
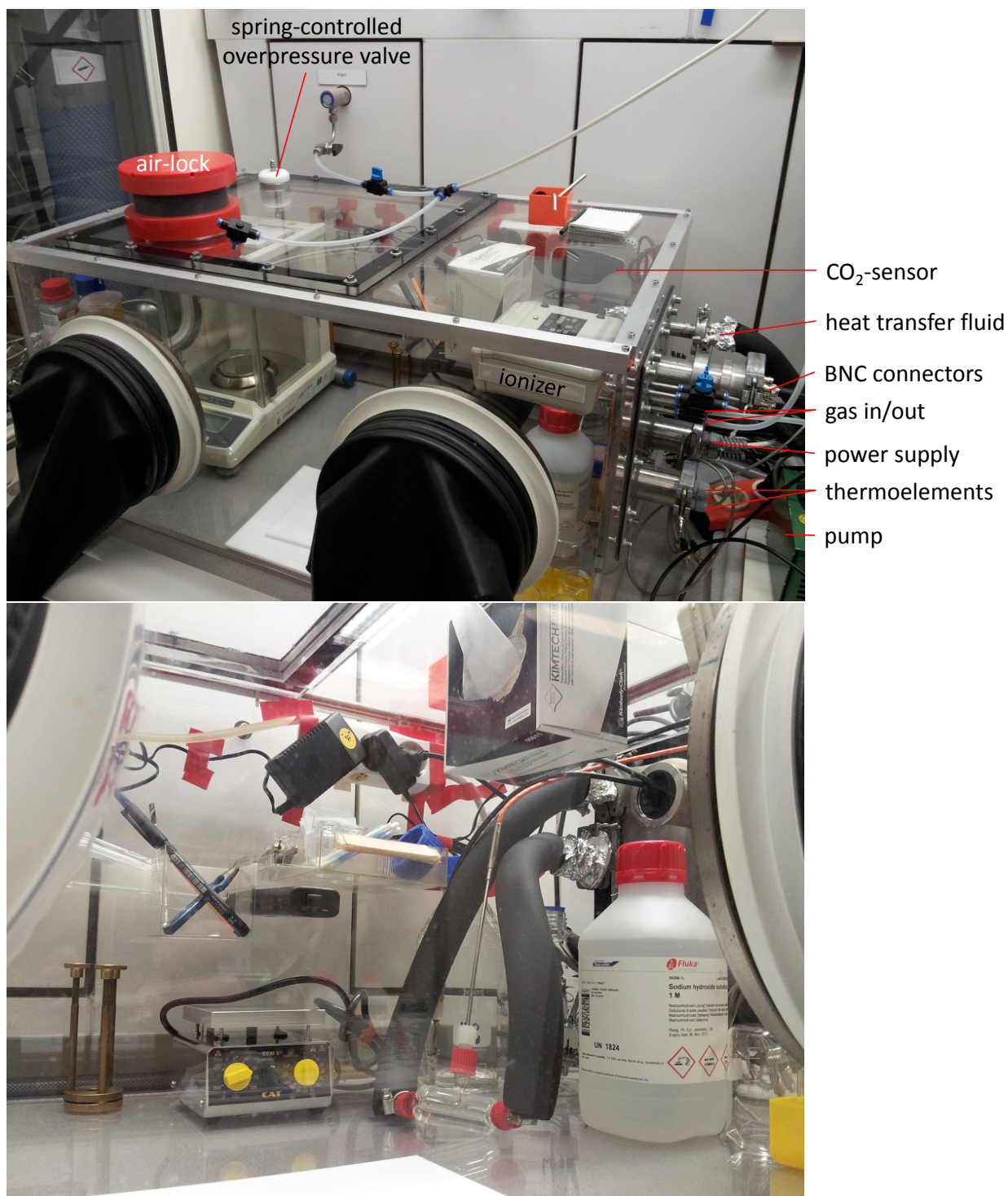
Figure 5.9: Outside and inside of the custom made glove box. The conductivity measurement cell is visible on the lower image.

List of abbreviations and symbols

List of abbreviations

AC . . . . alternating current
AFC . . . . alkaline fuel cell
AEM . . . . anion exchange membrane
CMC . . . . critical micelle formation concentration
DC . . . . direct current
EG . . . . ethylene glycol
FAA-3 . . . . . . commercial FuMaTech anion exchange membrane
FC . . . . fuel cell
HEM . . . . hydroxide exchange membrane
HSAB . . . . hard and soft acids and bases
IC . . . . impedance spectroscopy
IEC . . . . ion exchange capacity
IUPAC . . . . . . International Union of Pure and Applied Chemistry
NMR . . . . nuclear magnetic resonance
PEM . . . . proton exchange membrane
PFG . . . . pulsed field gradient
QA . . . . quaternary ammonium
RF . . . . radio frequency
RS . . . . Reinecke's salt
RT . . . . room temperature
RFB . . . . redox flow battery
SAXS . . . . small angle X-ray scattering
SE . . . . spin echo
S-PEEKK . . . sulfonated poly(ether ether ketone ketone)
STE . . . . stimulated echo
TGA . . . . thermogravimetric analysis

Molecule name abbreviations

ASU . . . . 6-azonia-spiro[5.5]undecane
ASN . . . . 5-azonia-spiro[4.4]nonane
BAABCO . . . 1-benzyl-4-aza-1-azoniumbicyclo[2.2.2]octane
BMI 1-benzyl-3-methylimidazolium
BMP . . . . N-benzyl-N-methylpiperidinium
BP . . . . benzylpyridinium
BTE . . . . benzyltriethylammonium
BTM . . . . benzyltrimethylammonium
DABCO . . . . 1,4-diazabicyclo[2.2.2]octane

DMP . . . . N,N-dimethylpiperidinium
DMPy . . . . . . N,N-dimethylpyrrolidinium
DTG 1,1-dibenzyl-2,2,3,3-tetramethylguanidinium
DTM . . . . decyltrimethylammonium
ETM . . . . ethyltrimethylammonium
HexDTM . . . hexadecyltrimethylammonium
HTM . . . . hexyltrimethylammonium
MAABCO . . 1-methyl-4-aza-1-azoniumbicyclo[2.2.2]octane
MBTM 3-methoxybenyzltrimethylammonium
MOI 1-methyl-3-octylimidazolium
NBTM . . . . . . (3-nitrobenzyl)-trimethylammonium
NTM . . . . neopentyltrimethylammonium
OTM . . . . octyltrimethylammonium
PTM . . . . propyltrimethylammonium
PhTM . . . . . . phenyltrimethylammonium
R . . . . arbitrary substitutent
TMA . . . . tetramethylammonium
TMAX . . . . . . TMA with counter anion X⁻
TMI 1,2,3-trimethylimidazolium
TPA . . . . tetrapropylammonium

List of symbols

A . . . . electrode area
α . . . . degree of dissociation
B_0 . . . . homogeneous magnetic main field
B_1 . . . . inhomogeneous magnetic gradient field
c . . . . concentration
D . . . . diffusion coefficient
D^∞ . . . . diffusion coefficient in infinite dilution
D_σ . . . . conductivity diffusion coefficient
Δ . . . . diffusion time
d . . . . spacing between boundaries in SAXS experiments
δ . . . . gradient pulse duration
E_A . . . . activation energy
e . . . . elementary charge
F . . . . Faraday constant
G . . . . strength of magnetic gradient
G_{form} . . . . form factor of a membrane
G_n . . . . fitting parameter for Gaussian fit
$\Delta G\#$ . . . . free energy reaction barrier
ΔH_i . . . . enthalpy of process or bond i

$T2$ . . . . spin-spin relaxation time

$t_{1/2}$ . . . . half life time

t . . . . time

θ . . . . phase angle in impedance spectroscopy

θ . . . . scattering angle in SAXS experiments

U . . . . electric potential

μ . . . . particle mobility

μ_n . . . . position of ionomer maximum for Gaussian fit

V . . . . volume

wt% . . . . weight percentage

ω . . . . frequency

ω_L . . . . Larmor frequency

x . . . . distance

y_n . . . . fitting parameter for Gaussian fit

z . . . . charge number of ions

Z . . . . total resistance of complex system

Z' . . . . real resistance

Z'' . . . . imaginary resistance

Z_f . . . . form factor of membrane

Acknowledgment

Bibliography

[1] J. K. Nørskov, J. Rossmeisl, A. Logadottir, L. Lindqvist, J. R. Kitchin, T. Bligaard, and H. Jónsson. Origin of the overpotential for oxygen reduction at a fuel-cell cathode. *The Journal of Physical Chemistry B*, 108(46):17886–17892, 2004.

[2] B.B. Blizanac, P.N. Ross, and N.M. Markovic. Oxygen electroreduction on ag(1 1 1): The ph effect. *Electrochimica Acta*, 52(6):2264 – 2271, 2007. Selection of papers from the Third Gerischer Symposium Berlin, Germany, 6-8 July 2005.

[3] P. Atkins and J. de Paula. *Elements of Physical Chemistry*. W. H. Freeman, 2009.

[4] Nagappan Ramaswamy and Sanjeev Mukerjee. Fundamental mechanistic understanding of electrocatalysis of oxygen reduction on pt and non-pt surfaces: Acid versus alkaline media. *Advances in Physical Chemistry*, 2012:17, 2012.

[5] P. Quaino, N. B. Luque, R. Nazmutdinov, E. Santos, and Wolfgang Schmickler. Why is gold such a good catalyst for oxygen reduction in alkaline media? *Angewandte Chemie International Edition*, 51(52):12997–13000, 2012.

[6] N. de Zoubov M.J.N. Pourbaix, J. Van Muylder. Electrochemical properties of the platinum metals. *Platinum Metals Review*, 3(2):47–53, 1959.

[7] A.K Chatterjee, Maheshwar Sharon, and Rangan Banerjee. Alkaline fuel cell: carbon nanobeads coated with metal catalyst over porous ceramic for hydrogen electrode. *Journal of Power Sources*, 117(1–2):39 – 44, 2003.

[8] V. Hacker, E. Wallnöfer, W. Baumgartner, T. Schaffer, J.O. Besenhard, H. Schröttner, and M. Schmied. Carbon nanofiber-based active layers for fuel cell cathodes – preparation and characterization. *Electrochemistry Communications*, 7(4):377 – 382, 2005.

[9] A.J. Appleby. Fuel cells – overview — introduction. In Jürgen Garche, editor, *Encyclopedia of Electrochemical Power Sources*, pages 277 – 296. Elsevier, Amsterdam, 2009.

[10] G. Mulder. Fuel cells – alkaline fuel cells — overview. In Jürgen Garche, editor, *Encyclopedia of Electrochemical Power Sources*, pages 321 – 328. Elsevier, Amsterdam, 2009.

[11] Qingping Hu, Guangwei Li, Jing Pan, Lisheng Tan, Juntao Lu, and Lin Zhuang. Alkaline polymer electrolyte fuel cell with ni-based anode and co-based cathode. *International Journal of Hydrogen Energy*, 38:16264–16268, 2013.

[12] G.J. Ross, J.F. Watts, M.P. Hill, and P. Morrissey. Surface modification of poly(vinylidene fluoride) by alkaline treatment1. the degradation mechanism. *Polymer*, 41(5):1685 – 1696, 2000.

[13] G.J Ross, J.F Watts, M.P Hill, and P Morrissey. Surface modification of poly(vinylidene fluoride) by alkaline treatment part 2. process modification by the use of phase transfer catalysts. *Polymer*, 42(2):403 – 413, 2001.

[14] Timothy N. Danks, Robert C. T. Slade, and John R Varcoe. Alkaline anion-exchange radiation-grafted membranes for possible electrochemical application in fuel cells. *J. Mater. Chem.*, 13:712–721, 2003.

[15] Christopher G. Arges, Min-Suk Jung, Graham Johnson, Javier Parrondo, and Vijay Ramani. Anion exchange membranes (aems) with perfluorinated and polysulfone backbones with different cation chemistries. *ECS Transactions*, 41(1):1795–1816, 2011.

[16] Min-suk J. Jung, Christopher G. Arges, and Vijay Ramani. A perfluorinated anion exchange membrane with a 1,4-dimethylpiperazinium cation. *Journal of Materials Chemistry*, 21(17):6158–6160, 2011.

[17] Holly L. S. Salerno and Yossef A. Elabd. Anion exchange membranes derived from nafion precursor for the alkaline fuel cell: Effect of cation type on properties. *Journal of Applied Polymer Science*, 127(1):298–307, JAN 5 2013.

[18] M. Cifrain and K. Kordesch. *Hydrogen/oxygen (air) fuel cells with alkaline electrolytes.* John Wiley & Sons, Ltd, 2010.

[19] J. Larminie and A. Dicks. *Fuel Cell Systems Explained.* J. Wiley, 2003.

[20] M. Warshay and P.R. Prokopius. The Fuel-Cell in Space - Yesterday, Today and Tomorrow. *Journal of Power Sources*, 29(1-2):193–200, JAN 1990.

[21] C. Ponce de León, A. Frías-Ferrer, J. González-García, D.A. Szánto, and F.C. Walsh. Redox flow cells for energy conversion. *Journal of Power Sources*, 160(1):716 – 732, 2006.

[22] M. Skyllas-Kazacos, M. H. Chakrabarti, S. A. Hajimolana, F. S. Mjalli, and M. Saleem. Progress in Flow Battery Research and Development. *Journal of the Electrochemical Society*, 158(8):R55–R79, 2011.

[23] Sukhwan Yun, Javier Parrondo, and Vijay Ramani. Derivatized cardo-polyetherketone anion exchange membranes for all-vanadium redox flow batteries. *J. Mater. Chem. A*, 2:6605–6615, 2014.

[24] M. Hess, R. G. Jones, J. Kahovec, T. Kitayama, P. Kratochvil, P. Kubisa, W. Mormann, R. F. T. Stepto, D. Tabak, J. Vohlidal, and E. S. Wilks. Terminology of polymers containing ionizable or ionic groups and of polymers containing ions - (IUPAC recommendations 2006). *Pure and Applied Chemistry*, 78(11):2067–2074, NOV 2006.

[25] Kyeong-Ho Yeon, Jung-Hoon Song, and Seung-Hyeon Moon. A study on stack configuration of continuous electrodeionization for removal of heavy metal ions from the primary coolant of a nuclear power plant. *Water Research*, 38(7):1911 – 1921, 2004.

[26] Guillaume Couture, Ali Alaaeddine, Frederic Boschet, and Bruno Ameduri. Polymeric materials as anion-exchange membranes for alkaline fuel cells. *Progress in Polymer Science*, 36(11):1521–1557, NOV 2011.

[27] Jean-Jacques Wolff. Ion exchange resins for use in nuclear power plants. *Purolite - Ion Exchange Resins*, pages 1–33, 2012.

[28] John R. Varcoe, Plamen Atanassov, Dario R. Dekel, Andrew M. Herring, Michael A. Hickner, Paul. A. Kohl, Anthony R. Kucernak, William E. Mustain, Kitty Nijmeijer, Keith Scott, Tongwen Xu, and Lin Zhuang. Anion-exchange membranes in electrochemical energy systems. *Energy Environ. Sci.*, 7:3135–3191, 2014.

[29] Melvin J. Hatch and Winston D. Lloyd. Preparation and properties of a neophyl type anion exchange resin. *Journal of Applied Polymer Science*, 8(4):1659–1666, 1964.

[30] Bernd Bauer, Heiner Strathmann, and Franz Effenberger. Anion-exchange membranes with improved alkaline stability. *Desalination*, 79(2-3):125–144, 1990. Proceeding of the 6th Symposium on Synthetic Membranes in Science and Industry.

[31] Toshikatsu Sata, Makie Tsujimoto, Takanori Yamaguchi, and Koji Matsusaki. Change of anion exchange membranes in an aqueous sodium hydroxide solution at high temperature. *Journal of Membrane Science*, 112(2):161 – 170, 1996.

[32] Geraldine Merle, Matthias Wessling, and Kitty Nijmeijer. Anion exchange membranes for alkaline fuel cells: A review. *Journal of Membrane Science*, 377(1-2):1–35, JUL 15 2011.

[33] Christopher G. Arges, Javier Parrondo, Graham Johnson, Athrey Nadhan, and Vijay Ramani. Assessing the influence of different cation chemistries on ionic conductivity and alkaline stability of anion exchange membranes. *J. Mater. Chem.*, 22:3733–3744, 2012.

[34] Dongyang Chen and Michael A. Hickner. Degradation of imidazolium- and quaternary ammonium-functionalized poly(fluorenyl ether ketone sulfone) anion exchange membranes. *ACS Applied Materials & Interfaces*, 4(11):5775–5781, 2012.

[35] Christopher G. Arges and Vijay Ramani. Two-dimensional NMR spectroscopy reveals cation-triggered backbone degradation in polysulfone-based anion exchange membranes. *Proceedings of the National Academy of Sciences of the United States of America*, 110(7):2490–2495, FEB 12 2013.

[36] Yuesheng Ye and Yossef A. Elabd. *Chemical Stability of Anion Exchange Membranes for Alkaline Fuel Cells*, chapter 15, pages 233–251. John Wiley & Sons, Ltd, 2010.

[37] Kevin J. T. Noonan, Kristina M. Hugar, Henry A. Kostalik, Emil B. Lobkovsky, Hector D. Abruna, and Geoffrey W. Coates. Phosphonium-functionalized polyethylene: A new class of base-stable alkaline anion exchange membranes. *Journal of the American Chemical Society*, 134(44):18161–18164, 2012.

[38] E. B. Trostyanakaya and S. B. Makarova. Anion exchangers of the onium class of compounds. *Journal of applied chemistry of the USSR*, 39:1754–1760, 1966.

[39] R Schwesinger, R Link, P Wenzl, S Kossek, and M Keller. Extremely base-resistant organic phosphazenium cations. *Chemistry - A European Journal*, 12(2):429–437, 2006.

[40] Yongping Zha, Melanie L. Disabb-Miller, Zachary D. Johnson, Michael A. Hickner, and Gregory N. Tew. Metal-cation-based anion exchange membranes. *Journal of the American Chemical Society*, 134(10):4493–4496, 2012.

[41] Bingzi Zhang, Shuang Gu, Junhua Wang, Ye Liu, Andrew M. Herring, and Yushan Yan. Tertiary sulfonium as a cationic functional group for hydroxide exchange membranes. *RSC Adv.*, 2:12683–12685, 2012.

[42] Frank N. Jones and Charles R. Hauser. Ortho-substitution rearrangement vs. elimination reaction of certain benzyl-type quaternary ammonium ions with sodium amide1. *The Journal of Organic Chemistry*, 27(5):1542–1547, 1962.

[43] Stanley H. Pine. *The Base-Promoted Rearrangements of Quaternary Ammonium Salts.* John Wiley & Sons, Inc., 2004.

[44] Thomas Stevens Stevens, Elton Marshall Creighton, Alexander Brown Gordon, and Malcolm MacNicol. Ccccxxiii.-degradation of quaternary ammonium salts. part i. *J. Chem. Soc.*, pages 3193–3197, 1928.

[45] M.B. Smith and J. March. *March's Advanced Organic Chemistry: Reactions, Mechanisms, and Structure.* Wiley, 2007.

[46] K.P.C. Vollhardt and N.E. Schore. *Organic Chemistry.* W. H. Freeman, 2009.

[47] P.Y. Bruice. *Organic Chemistry.* Pearson Education, 2013.

[48] Bo Qiu, Bencai Lin, Lihua Qiu, and Feng Yan. Alkaline imidazolium- and quaternary ammonium-functionalized anion exchange membranes for alkaline fuel cell applications. *J. Mater. Chem.*, 22:1040–1045, 2012.

[49] Michael R. Hibbs. Alkaline stability of poly(phenylene)-based anion exchange membranes with various cations. *Journal of Polymer Science Part B: Polymer Physics*, pages 1736–1742, 2012.

[50] Qiang Zhang, Shenghai Li, and Suobo Zhang. A novel guanidinium grafted poly(aryl ether sulfone) for high-performance hydroxide exchange membranes. *Chem. Commun.*, 46:7495–7497, 2010.

[51] Junhua Wang, Shenghai Li, and Suobo Zhang. Novel hydroxide-conducting polyelectrolyte composed of an poly(arylene ether sulfone) containing pendant quaternary guanidinium groups for alkaline fuel cell applications. *Macromolecules*, 43(8):3890–3896, 2010.

[52] Oliver I. Deavin, Sam Murphy, Ai Lien Ong, Simon D. Poynton, Rong Zeng, Henryk Herman, and John R. Varcoe. Anion-exchange membranes for alkaline polymer electrolyte fuel cells: comparison of pendent benzyltrimethylammonium- and benzylmethylimidazolium-head-groups. *Energy Environ. Sci.*, 5:8584–8597, 2012.

[53] Oliver M. M. Page, Simon D. Poynton, Sam Murphy, Ai Lien Ong, Donna M. Hillman, Cathryn A. Hancock, Michael G. Hale, David C. Apperley, and John R. Varcoe. The alkali stability of radiation-grafted anion-exchange membranes containing pendent 1-benzyl-2,3-dimethylimidazolium head-groups. *RSC Adv.*, 3:579–587, 2013.

[54] Sean A. Nuñez and Michael A. Hickner. Quantitative 1h nmr analysis of chemical stabilities in anion-exchange membranes. *ACS Macro Letters*, 2(1):49–52, 2013.

[55] Tim Peppel, Christin Schmidt, and Martin Köckerling. Synthesis, properties, and structures of salts with the reineckate anion, [criii(ncs)4(nh3)2]–, and large organic cations. *Zeitschrift für anorganische und allgemeine Chemie*, 637(10):1314–1321, 2011.

[56] G. Jander, J. Strähle, E. Schweda, and E. Blasius. *Lehrbuch der analytischen und präparativen anorganischen Chemie: mit 67 Tabellen und 36 Kristallaufnahmen.* Hirzel, 2006.

[57] W.S. Selig. Quaternary Ammonium Halides - Versatile Reagents for Precipitation Titrations. *Journal of Chemical Education*, 64(2):141–143, FEB 1987.

[58] ELEANOR J. ZAIMIS. The synthesis of methonium compounds, their isolation from urine, and their photometric determination. *British Journal of Pharmacology and Chemotherapy*, 5(3):424–430, 1950.

[59] Hai Long, Kwiseon Kim, and Bryan S. Pivovar. Hydroxide degradation pathways for substituted trimethylammonium cations: A dft study. *The Journal of Physical Chemistry C*, 116(17):9419–9426, 2012.

[60] Samuel C. Price, Kristen S. Williams, and Frederick L. Beyer. Relationships between structure and alkaline stability of imidazolium cations for fuel cell membrane applications. *ACS Macro Letters*, 3(2):160–165, 2014.

[61] Bernd Bauer. Untersuchung und verbesserung der alkalistabilität von anionenaustauschermembranen. Master's thesis, Universität Stuttgart, 1988.

[62] Anika Katzfuß, Viktor Gogel, Ludwig Jörissen, and Jochen Kerres. The application of covalently cross-linked brppo as aem in alkaline dmfc. *Journal of Membrane Science*, 425-426(0):131 – 140, 2013.

[63] Dirk Henkensmeier, Hyeong-Rae Cho, Hyoung-Juhn Kim, Carolina Nunes Kirchner, Janine Leppin, Alexander Dyck, Jong Hyun Jang, EunAe Cho, Suk-Woo Nam, and Tae-Hoon Lim. Polybenzimidazolium hydroxides: Structure, stability and degradation. *Polymer Degradation and Stability*, 97(3):264 – 272, 2012.

[64] M Tomoi, K Yamaguchi, R Ando, Y Kantake, Y Aosaki, and H Kubota. Synthesis and thermal stability of novel anion exchange resins with spacer chains. *Journal of Applied Polymer Science*, 64(6):1161–1167, MAY 9 1997.

[65] Nanwen Li, Tingzi Yan, Zheng Li, Thomas Thurn-Albrecht, and Wolfgang H. Binder. Comb-shaped polymers to enhance hydroxide transport in anion exchange membranes. *Energy Environ. Sci.*, 5:7888–7892, 2012.

[66] Alina Amel, Liang Zhu, Michael Hickner, and Yair Ein-Eli. Influence of sulfone linkage on the stability of aromatic quaternary ammonium polymers for alkaline fuel cells. *Journal of The Electrochemical Society*, 161(5):F615–F621, 2014.

[67] P. Mörters, Y. Peres, O. Schramm, and W. Werner. *Brownian Motion*. Cambridge Series in Statistical and Probabilistic Mathematics. Cambridge University Press, 2010.

[68] Adolf Fick. Ueber diffusion. *Annalen der Physik*, 170(1):59–86, 1855.

[69] Jean Philibert. One and a half century of diffusion: Fick, einstein, before and beyond. *Diffusion Fundamentals*, 6:1–19, 2006.

[70] H. Mehrer. *Diffusion in Solids: Fundamentals, Methods, Materials, Diffusion-Controlled Processes*. Springer Series in Solid-State Sciences. Springer, 2007.

[71] E. Barsoukov and J.R. Macdonald. *Impedance Spectroscopy: Theory, Experiment, and Applications*. Wiley-Interscience. Wiley, 2005.

[72] William S. Price. Pulsed-field gradient nuclear magnetic resonance as a tool for studying translational diffusion: Part 1. basic theory. *Concepts in Magnetic Resonance*, 9(5):299–336, 1997.

[73] J. Keeler. *Understanding NMR Spectroscopy*. Wiley, 2011.

[74] E. O. Stejskal and J. E. Tanner. Spin diffusion measurements: Spin echoes in the presence of a time dependent field gradient. *The Journal of Chemical Physics*, 42(1):288–292, 1965.

[75] O. Glatter and O. Kratky. *Small Angle X-ray Scattering*. Academic Press, 1982.

[76] Benjamin Chu and Benjamin S. Hsiao. Small-angle x-ray scattering of polymers. *Chemical Reviews*, 101(6):1727–1762, 2001. PMID: 11709997.

[77] Klaus-Dieter Kreuer and Giuseppe Portale. A critical revision of the nano-morphology of proton conducting ionomers and polyelectrolytes for fuel cell applications. *Advanced Functional Materials*, 23:5390–5397, 2013.

[78] Toomas Rodima, Ivari Kaljurand, Aino Pihl, Vahur Mäemets, V.emets, Ivo Leito, and Ilmar A. Koppel. Acid-base equilibria in nonpolar media 2.1 self-consistent basicity scale in thf solution ranging from 2-methoxypyridine to etp1(pyrr) phosphazene. *The Journal of Organic Chemistry*, 67(6):1873–1881, 2002. PMID: 11895405.

[79] James Walker and John Johnston. C.-tetramethylammonium hydroxide. *J. Chem. Soc., Trans.*, 87:955–961, 1905.

[80] Daniela Stoica, Fannie Alloin, Stephane Marais, Dominique Langevin, Corinne Chappey, and Patrick Judeinstein. Polyepichlorhydrin membranes for alkaline fuel cells: Sorption and conduction properties. *Journal of Physical Chemistry B*, 112(39):12338–12346, OCT 2 2008.

[81] Junhua Wang, Zhuo Zhao, Feixiang Gong, Shenghai Li, and Suobo Zhang. Synthesis of Soluble Poly(arylene ether sulfone) Ionomers with Pendant Quaternary Ammonium Groups for Anion Exchange Membranes. *Macromolecules*, 42(22):8711–8717, NOV 24 2009.

[82] Jing Pan, Shanfu Lu, Yan Li, Aibin Huang, Lin Zhuang, and Juntao Lu. High-Performance Alkaline Polymer Electrolyte for Fuel Cell Applications. *Advanced Functional Materials*, 20(2):312–319, JAN 22 2010.

[83] Qiang Zhang, Qifeng Zhang, Junhua Wang, Suobo Zhang, and Shenghai Li. Synthesis and alkaline stability of novel cardo poly(aryl ether sulfone)s with pendent quaternary ammonium aliphatic side chains for anion exchange membranes. *Polymer*, 51(23):5407–5416, OCT 29 2010.

[84] Liang Wu, Guangfeng Zhou, Xing Liu, ZhengHui Zhang, Chuanrun Li, and Tongwen Xu. Environmentally friendly synthesis of alkaline anion exchange membrane for fuel cells via a solvent-free strategy. *Journal of Membrane Science*, 371(1-2):155–162, APR 1 2011.

[85] Bo Qiu, Bencai Lin, Zhihong Si, Lihua Qiu, Fuqiang Chu, Jie Zhao, and Feng Yan. Bis-imidazolium-based anion-exchange membranes for alkaline fuel cells. *Journal of Power Sources*, 217(0):329 – 335, 2012.

[86] Shahana Chowdhury, Ram S. Mohan, and Janet L. Scott. Reactivity of ionic liquids. *Tetrahedron*, 63(11):2363 – 2389, 2007.

[87] Giorgio Cerichelli, Gabriello Illuminati, and Claudio Lillocci. Structural and mechanistic effects on the rates of ring-opening reactions in the 5-16-membered-ring region. *The Journal of Organic Chemistry*, 45(20):3952–3957, 1980.

[88] Giorgio Cerichelli and Luciana Luchetti. Ring-opening reactions. the reactivity of pyrrolidinium and piperidinium ions in solution. *Tetrahedron*, 49(46):10733 – 10738, 1993.

[89] Lei Liu, Qing Li, Jingwen Dai, Hu Wang, Bangkun Jin, and Ruke Bai. A facile strategy for the synthesis of guanidinium-functionalized polymer as alkaline anion exchange membrane with improved alkaline stability. *Journal of Membrane Science*, 453(0):52 – 60, 2014.

[90] Charles J.M. Stirling. Evaluation of the effect of strain upon reactivity. *Tetrahedron*, 41(9):1613 – 1666, 1985.

[91] Christopher Kelk Ingold and Charles Cyril Norrey Vass. Ccccxi.-influence of poles and polar linkings on the course pursued by elimination reactions. part ii. mechanism of exhaustive methylation (continued). *J. Chem. Soc.*, pages 3125–3127, 1928.

[92] Julius v. Braun, Wilhelm Teuffert, and Karl Weißbach. Über den zerfall quartärer ammonium- und sulfoniumhydroxyde. iv. *Justus Liebigs Annalen der Chemie*, 472(1):121–142, 1929.

[93] D. A. Archer and H. Booth. 50. the thermal decomposition of quaternary ammonium hydroxides. part i. methohydroxides derived from nn-dialkylanilines and related compounds. *J. Chem. Soc.*, pages 322–330, 1963.

[94] Brian R. Einsla, Shaji Chempath, Lawrence Pratt, James Boncella, Jonathan Rau, Clay Macomber, and Bryan Pivovar. Stability of cations for anion exchange membrane fuel cells. *ECS Transactions*, 11(1):1173–1180, 2007.

[95] J.J. Brunet, D. Neibecker, and F. Niedercorn. Functionalization of Alkenes - Catalytic Amination of Monoolefins. *Journal of Molecular Catalysis*, 49(3):235–259, FEB 9 1989.

[96] Thomas E. Mueller, Kai C. Hultzsch, Miguel Yus, Francisco Foubelo, and Mizuki Tada. Hydroamination: Direct addition of amines to alkenes and alkynes. *Chemical Reviews*, 108(9):3795–3892, SEP 2008.

[97] C. A. Bunton and L. Robinson. Micellar effects upon nucleophilic aromatic and aliphatic substitution. *Journal of the American Chemical Society*, 90(22):5972–5979, 1968.

[98] D.F. Evans, M. Allen, B.W. Ninham, and A. Fouda. Critical Micelle Concentrations for Alkyltrimethylammalkyl Bromide in Water From 25 Degrees C to 160 Degrees C. *Journal of Solution Chemistry*, 13(2):87–101, 1984.

[99] Panagiotis Lianos and Raoul Zana. Micellar properties of alkyltrimethylammonium hydroxydes in aqueous solution. *The Journal of Physical Chemistry*, 87(8):1289–1291, 1983.

[100] M. L. Corrin and William D. Harkins. The effect of salts on the critical concentration for the formation of micelles in colloidal electrolytes1. *Journal of the American Chemical Society*, 69(3):683–688, 1947.

[101] Bappaditya Naskar, Arnab Dey, and Satya P. Moulik. Counter-ion Effect on Micellization of Ionic Surfactants: A Comprehensive Understanding with Two Representatives, Sodium Dodecyl Sulfate (SDS) and Dodecyltrimethylammonium Bromide (DTAB). *Journal of Surfactants and Detergents*, 16(5):785–794, SEP 2013.

[102] Henry Eyring. The activated complex in chemical reactions. *The Journal of Chemical Physics*, 3(2):107–115, 1935.

[103] Keith J. Laidler and M. Christine King. Development of transition-state theory. *The Journal of Physical Chemistry*, 87(15):2657–2664, 1983.

[104] EN Komkova, DF Stamatialis, H Strathmann, and M Wessling. Anion-exchange membranes containing diamines: preparation and stability in alkaline solution. *Journal of Membrane Science*, 244(1-2):25–34, NOV 15 2004.

[105] Paul von R. Schleyer, James Earl Williams, and Blanchard K. R. Evaluation of strain in hydrocarbons. the strain in adamantane and its origin. *Journal of the American Chemical Society*, 92(8):2377–2386, 1970.

[106] Kenneth B. Wiberg, Richard F. W. Bader, and Clement D. H. Lau. Theoretical analysis of hydrocarbon properties. 2. additivity of group properties and the origin of strain energy. *Journal of the American Chemical Society*, 109(4):1001–1012, 1987.

[107] G. Courtois, M. Harama, and Ph. Miginiac. Synthese univoque d'amines tertiaires insaturees par voie organometallique a partir de sels d'immonium: Ii. synthese d'amines beta et alpha ethyleniques. *Journal of Organometallic Chemistry*, 218(3):275 – 298, 1981.

[108] T. N. De Castro Dantas, J. P. Laval, and A. Lattes. Preparation de sels d'aminoalkylphosphoniums. *Phosphorous and Sulfur and the Related Elements*, 13(1):97–105, 1982.

[109] Gabriello Illuminati and Claudio Lillocci. Ring-opening reactions. 1. decomposition of some quaternary ammonium ions with sodium methoxide in methanol. *The Journal of Organic Chemistry*, 42(13):2201–2203, 1977.

[110] Gabriella Cospito, Gabriello Illuminati, Claudio Lillocci, and Horia Petride. Ring-opening reactions. 3. mechanistic path vs. ring-strain control in elimination and substitution reactions of 1,1-dimethyl cyclic ammonium ions and their .alpha.,.alpha.'-dimethyl-substituted derivatives. *The Journal of Organic Chemistry*, 46(14):2944–2947, 1981.

[111] David R. Linde, editor. *CRC Handbook of Chemistry & Physics*. CRC Press, 88 edition, 2007.

[112] Yizhak Marcus. Effect of Ions on the Structure of Water: Structure Making and Breaking. *Chemical Reviews*, 109(3):1346–1370, MAR 2009.

[113] Dominik Marx, Amalendu Chandra, and Mark E. Tuckerman. Aqueous Basic Solutions: Hydroxide Solvation, Structural Diffusion, and Comparison to the Hydrated Proton. *Chemical Reviews*, 110(4):2174–2216, APR 2010.

[114] Mark E. Tuckerman, Dominik Marx, and Michele Parrinello. The nature and transport mechanism of hydrated hydroxide ions in aqueous solution. *Nature*, 417(6892):925–929, June 2002.

[115] Lin Zeng and Tianshou Zhao. High-performance alkaline ionomer for alkaline exchange membrane fuel cells. *Electrochemistry Communications*, 34:278–281, 2013.

[116] Guigui Wang, Yiming Weng, Deryn Chu, Rongrong Chen, and Dong Xie. Developing a polysulfone-based alkaline anion exchange membrane for improved ionic conductivity. *Journal of Membrane Science*, 332(1-2):63–68, APR 15 2009.

[117] Wenpin Wang, Shubo Wang, Weiwei Li, Xiaofeng Xie, and Yafei lv. Synthesis and characterization of a fluorinated cross-linked anion exchange membrane. *International Journal of Hydrogen Energy*, 38(25):11045–11052, 2013.

[118] John R. Varcoe, Robert C. T. Slade, Eric Lam How Yee, Simon D. Poynton, Daniel J. Driscoll, and David C. Apperley. Poly(ethylene-co-tetrafluoroethylene)-derived radiation-grafted anion-exchange membrane with properties specifically tailored for application in metal-cation-free alkaline polymer electrolyte fuel cells. *Chemistry of Materials*, 19(10):2686–2693, MAY 15 2007.

[119] Xiaoming Yan, Gaohong He, Shuang Gu, Xuemei Wu, Liguang Du, and Haiyan Zhang. Quaternized poly(ether ether ketone) hydroxide exchange membranes for fuel cells. *Journal of Membrane Science*, 375(1-2):204–211, JUN 15 2011.

[120] Hiroyuki Yanagi and Kenji Fukuta. Anion exchange membrane and ionomer for alkaline membrane fuel cells (amfcs). *ECS Transactions*, 16(2):257–262, 2008. 8th Symposium on Proton Exchange Membrane Fuel Cells, Honolulu, HI, OCT, 2008.

[121] M.G. Marino, J.P. Melchior, A. Wohlfarth, and K.D. Kreuer. Hydroxide, halide and water transport in a model anion exchange membrane. *Journal of Membrane Science*, 464(0):61 – 71, 2014.

[122] V.V. Kisel'nik, N.G. Malyuk, A.N. Toryanik, and V.M. Toryanik. Effect of pressure and temperature of the self-diffusion of water. *Journal of Structural Chemistry*, 14(6):911–914, 1974.

[123] Subhash V. Talekar. Temperature dependence of activation energies for self-diffusion of water and of alkali ions in aqueous electrolyte solutions. a model for ion selective behavior of biological cells. *International Journal of Quantum Chemistry*, 12(S4):459–469, 1977.

[124] Truman S. Light, Stuart Licht, Anthony C. Bevilacqua, and Kenneth R. Morash. The fundamental conductivity and resistivity of water. *Electrochemical and Solid-State Letters*, 8(1):E16–E19, 2005.

[125] Song Hi Lee and Jayendran C. Rasaiah. Proton transfer and the mobilities of the h+ and oh- ions from studies of a dissociating model for water. *The Journal of Chemical Physics*, 135(12):–, 2011.

[126] R. K. McMullan, T. C. W. Mak, and G. A. Jeffrey. Polyhedral clathrate hydrates. xi. structure of tetramethylammonium hydroxide pentahydrate. *The Journal of Chemical Physics*, 44(6):2338–2345, 1966.

[127] Ralph G. Pearson. Hard and soft acids and bases. *Journal of the American Chemical Society*, 85(22):3533–3539, 1963.

[128] Yizhak Marcus. Tetraalkylammonium ions in aqueous and non-aqueous solutions. *Journal of Solution Chemistry*, 37(8):1071–1098, AUG 2008.

[129] Laurent Rubatat, Anne Laure Rollet, Gerard Gebel, and Olivier Diat. Evidence of elongated polymeric aggregates in nafion. *Macromolecules*, 35(10):4050–4055, 2002.

[130] M. G. Marino and K. D. Kreuer. Alkaline stability of quaternary ammonium cations for alkaline fuel cell membranes and ionic liquids. *ChemSusChem*, 8(3):513–523, 2015.

[131] Joseph B. Edson, Clay S. Macomber, Bryan S. Pivovar, and James M. Boncella. Hydroxide based decomposition pathways of alkyltrimethylammonium cations. *Journal of Membrane Science*, 399-400(0):49 – 59, 2012.

[132] Jianbing Zhang, Bingwen Jing, Vaclav Janout, and Steven L. Regen. Detecting cross talk between two halves of a phospholipid bilayer. *Langmuir*, 23(17):8709–8712, 2007.

[133] Angelo V. Santoro and Grace Mickevicius. Hindered rotation in hexasubstituted guanidine salts. *The Journal of Organic Chemistry*, 44(1):117–120, 1979.

Used programs and copyright information

The cover molecule art was created using *Chem3D* and edited using *PowerPoint.* The cover molecule backgrounds are ©*Artjazz Dreamtime.com – Red and Blue Powder Explosion Isolated On White*, partially recolored and edited using *GIMP.* White line in blue powder explosion is from ©*Amos Struck Dreamtime.com – Hand and Static Electricity Arc.*

Fuel cell, redox flow battery, TGA, and membrane stack schemes were created using *CorelDRAW.* Figures were created with *Origin, PowerPoint* or *Mathematica.* NMR spectra are images created with *Bruker TopSpin.* Chemical structures were drawn using *ChemDraw.*

This thesis was typeset using LaTeX with TeXnicCenter.

Michael G. Marino

* 13.10.1984 in Backnang

Südstraße 142 | 71522 Backnang | 0176 70717622
michael.marino@hotmail.de

06/2011 – 04/2015 **Dr. rer. nat. in Chemistry *(scl)***
Max Planck Institute for Solid State Research, Stuttgart (Germany)
„Anion exchange membranes for fuel cells and flow batteries"
Supervisors: Dr. Kreuer and Prof. Dr. Maier

10/2005 – 11/2010 **Diplom in Chemistry**
University of Stuttgart, Diplom (grade „sehr gut"), Supervisor:
Diploma thesis: „Cobalt-mediierte radikalische Polymerisation von
Acrylnitril"(grade 1.0), Supervisor: Prof. Dr. Buchmeiser

07/2004 – 04/2005 **Community service in lieu of military service**
Arbeiter Samariter Bund and Katholische Sozialstation, Backnang

09/2001 – 06/2004 **Higher education entrance qualification**
Technisches Gymnasium Backnang, Abitur (grade 1.7)

09/1995 – 07/2001 **Upper secondary school**
Max-Born-Gymnasium Backnang

04/2009 – 09/2009 **Honorary research fellow**
University of Auckland (New Zealand), topic: „Synthesis and
hydrogenation of β-alkoxymethyl enecarbamates"
Supervisors: Dr. O'Connor and Prof. Dr. Brimble.

Backnang, 28. May 2015

List of publications, talks and poster

M.G. Marino, K.D. Kreuer, Alkaline stability of quaternary ammonium cations for alkaline fuel cells and ionic liquids, *Chem.Sus.Chem.* **2015**, *8*, 513-523.

M.G. Marino, J.P. Melchior, A. Wohlfarth, K.D. Kreuer, Hydroxide, halide and water transport in a model anion exchange membrane, *J. Mem. Sci.* **2014**, *464*, 61-71.

M.R. Buchmeiser, M.G. Marino, Co(acac)$_2$-mediated radical polymerization of acrylonitrile: Control over molecular weights and copolymerization with methyl methacrylate, *Macromol. Mater. Eng.* **2012**, *297*, 894-901.

P.D. O'Connor, M.G. Marino, S.M. Gueret, M.A. Brimble, Synthesis and reactivity of β-methoxymethyl enecarbamates, *J. Org. Chem.* **2009**, *74*, 8893.

A. Wohlfarth, S. Takamuku, G. Titvinidze, M.G. Marino, M. Melchior, K.D. Kreuer, Acid-base blending of highly sulfonated polysulfones, in preparation.

J.P. Melchior, M.G. Marino, K.D. Kreuer, Hydration and thermodynamics of phosphoric acid-polybenzimidazole mixtures: A model system for PBI/PA fuel cells, in preparation.

M.G. Marino, talk with title: Ion transport in membranes for fuel cells and batteries, European Congress and Exhibition on Advanced Materials and Processes (EUROMAT), Sevilla, Spain, September 2013.

M.G. Marino, J.P. Melchior, K.D. Kreuer, talk with title: Hydroxide conductivity of anion exchange membranes for alkaline polymer electrolyte fuel cells, Electrochemistry (GDCh), München, Germany, September 2012.
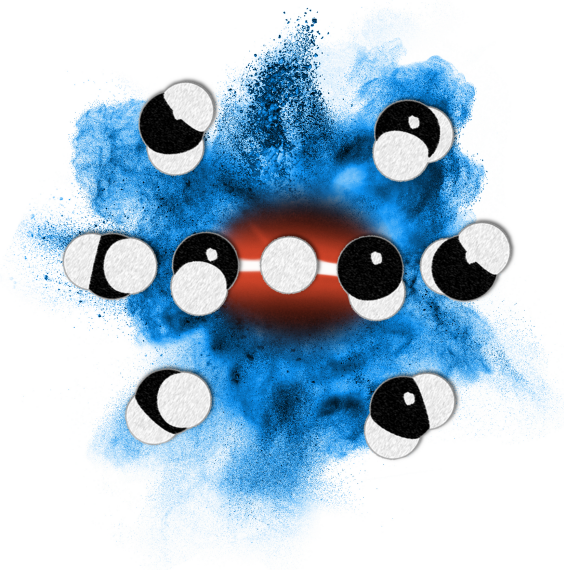
M.G. Marino, J.P. Melchior, K.D. Kreuer, poster with title: Anion exchange membranes: Hydration, hydroxide conductivity and water diffusion under CO_2-free conditions, Solid State Proton Conductors (SSPC 16), Grenoble, France, September 2012.

M.G. Marino, J.P. Melchior, K.D. Kreuer, talk with title: Hydroxide conductivity of anion exchange membranes for alkaline polymer electrolyte fuel cells, European Materials Research Society (EMRS), Straßburg, France, May 2012.

The 6-azonia-spiro[5.5]undecane ion, shown on the left, synthesized during this thesis may well be the most stable ammonium ion under alkaline conditions in existence. Its cyclic structure inhibits both elimination and substitution reactions. As HEM functional group it may increase the operating temperature of HEM fuel cells considerably.

The structural diffusion process of hydroxide, shown on the right, requires a sufficient number of water molecules to occur. Together with a lower degree of dissociation of the ammonium hydroxide groups, this explains the lower conductivity of HEMs compared to PEMs at low hydration. At adequate hydration HEMs can in fact reach comparable conductivities to PEMs.